Polymerization Control in Surface-Mounted Metal-Organic Frameworks

Zur Erlangung des akademischen Grades einer

DOKTORIN DER NATURWISSENSCHAFTEN

(Dr. rer. nat.)

von der KIT-Fakultät für Chemie und Biowissenschaften

des Karlsruher Instituts für Technologie (KIT)

genehmigte

DISSERTATION

von

M. Sc. Beren Sen

aus

Istanbul, Türkei

1. Referent: Prof. Dr. Christof Wöll
2. Referent: Prof. Dr. Stefan Bräse
Tag der mündlichen Prüfung: 07.12.2020

The present thesis was carried out from March, 2017 to June, 2020 under the supervision of Prof. Dr. Christof Wöll at the Institute of Functional Interfaces (IFG) in Karlsruhe Institute of Technology (KIT).

I hereby declare that this Ph.D. thesis is based on my work and it was written solely by myself. I did not use any other sources, references and aids other than those mentioned in the thesis. All the text and figures that are not my own cited properly by me.

Beren Sen

Karlsruhe, 16.12.2020

TABLE OF CONTENTS

ABSTRACT

The work performed within this thesis aims towards templated polymerization reactions in the confined pore space of surface-mounted metal-organic frameworks (SURMOFs) and find applicable use cases. SURMOFs are synthesized in a highly oriented crystalline manner on flat, functionalized substrates using layer-by-layer deposition (LBL) and are used as a template for the controlled polymerization reactions of conductive oligomers/polymers with use cases in different potential areas, such as optoelectronics or sensors.

The first part of the thesis is the oligomerization of terthiophene (Tth) and 3,4-ethylenedioxythiophene (EDOT) in different structures with SURMOF-2 topology, which consists of 1D channels formed by lamellar ordered 2D MOF sheets. Zn(bdc) and Cu(bdc) were used as a host structure for Tth polymerization, whereas Cu(bpdc) were used for EDOT polymerization. Tth and EDOT were incorporated into the SURMOF pores followed by the initiation of oligomerization reaction in the presence of oxidizing agents (I_2 for Tth, $FeCl_3$ for EDOT). It was observed that the crystallinity of the SURMOF-2 structures was not affected by oligomerization reaction. The short chain lengths and the size distribution of the formed poly(terthiophene) (PTh) and poly(3,4-ethylenedioxythiophene) (PEDOT) were characterized by using matrix-assisted laser desorption ionization time-of-flight mass spectrometry (MALDI-ToF/MS). Moreover, spectroscopic techniques, such as UV-Vis, Fourier-transform infrared spectroscopy (FTIR) and Raman spectroscopy, proved that the oligomers are forming inside the pores of the SURMOFs. Electrochemical impedance spectroscopy (EIS) was carried out in order to measure the electrical conductivity of Cu(bpdc) SURMOF thin films after the oligomerization of EDOT. The electrical alternating current conductivity measurements for PEDOT loaded SURMOF thin films revealed an increase in the electroconductivity, which plays a crucial role for applications such as in optoelectronics.

As a second part of the thesis is investigating the Pd-catalyzed polymerization reaction of methyl propiolate (MP). The reaction was carried out in the confined pores of three different SURMOFs: Cu(bpdc) and $Cu_2(bdc)_2(dabco)$ and HKUST-1. These three SURMOF systems were selected as a

template for the polymerization reaction because of their different types of pore windows, pore channels and pore volumes. MP was loaded into the pores of the SURMOFs in presence of $PdCl_2$ in trace amounts as a catalyst and the polymerization reaction was took place at elevated temperatures. The polymer formation and its effect on the SURMOF structure were investigated by using the X-ray diffraction (XRD), scanning electron microscopy (SEM), energy dispersive x-ray spectroscopy / mapping (EDXS, EDXM), atomic force microscopy (AFM), time-of-flight secondary ion mass spectrometry (ToF-SIMS), MALDI-ToF/MS, quartz crystal microbalance (QCM) and 2-probe current-voltage measurements. The XRD patterns showed that MP loading into SURMOFs and polymerization in SURMOFs affects the intensities of the reflexes and the form factors. However, the crystallinity of the SURMOF structures remained unchanged. Further experimental investigations, carried out using by SEM and EDXM, revealed a polymer top layer formation for the Cu(bpdc) and $Cu_2(bdc)_2(dabco)$, whereas no top layer formation was observed for HKUST-1. The reason for the formation of the polymer top layer was investigated by QCM analysis, which indicated a depot-like slow release of MP from Cu(bpdc), whereas a quick release from HKUST-1 is found. A depot-like slow out-diffusion of MP is assumed to trigger the formation of a polymer top layer. ToF-SIMS analyses showed that the polymerization occurred inside all the three SURMOFs despite of the fact of a polymer top layer formation in Cu(bpdc) and $Cu_2(bdc)_2(dabco)$. A variation of the maximum chain lengths and molecular weight distribution of the polymer chains was also observed and was attributed to the different pore systems of SURMOFs. HKUST-1 was found to be the best model for the polymerization reaction inside the pores of SURMOFs, since no polymer top layer formation was found for HKUST-1. Therefore, only for this SURMOF electrical direct current conductivity was measured after MP polymerization. A strong increase in electrical conductivity compared to the pristine HKUST-1 was found, amounting to 6 orders of magnitude. Introducing electrical conductivity to SURMOFs by using them as a template for the polymerization reactions leads to different promising applications of SURMOF thin films, e.g. for the fabrication of sensors and in microelectronics.

ZUSAMMENFASSUNG

Diese Arbeit behandelt templatgeleitete Polymerisationsreaktionen im Porenraum oberflächen-verankerter Metall-Organischen Gerüstverbindungen (engl. surface-mounted metal-organic frameworks; SURMOFs). SURMOFs, die in hochorientierter, hochkristalliner Form auf funktionalisierten Substraten durch Lage-für-Lage Verfahren (engl, layer-by-layer, LBL) synthetisiert werden, wurden als Template für kontrollierte Polymerisationsreaktionen von verschiedener leitfähigen Oligomere/Polymeren verwendet und für potenzielle Anwendungen in Bereichen wie Optoelektronik oder Sensoren getestet.

Die erste Studie behandelt Oligomerisierung von Terthiophen (Tth) und 3,4-Ethylendioxythiophen (EDOT) in verschiedenen SURMOF-2-Strukturen, die sich aus lamellar geordneten 2D-MOF-Schichten mit 1-D Kanälen zusammensetzen. Zn(bdc) und Cu(bdc) wurden als Template für die Tth-Polymerisation verwendet, während Cu(bpdc) für die EDOT-Polymerisation verwendet wurde. Nach der Synthese der SURMOFs wurden Tth und EDOT die Poren von SURMOF-2 eingebracht und danach durch Oxidationsmitteln (I_2 für Tth, $FeCl_3$ für EDOT) oligomerisiert. Die Kristallinität der SURMOF-2-Strukturen wurde durch die Oligomerisierungsreaktion nicht beeinflusst. Die kurzen Kettenlängen und die Größenverteilung des gebildeten Poly (terthiophens) (PTh) und Poly (3,4-ethylendioxythiophens) (PEDOT) wurden unter Verwendung der matrix-assistierte Laser-Desorption-Ionisierung Flugzeitanalyse Massenspektrometrie (MALDI-ToF/MS) überprüft. Darüber hinaus haben spektroskopische Techniken, UV-Vis-, FTIR- und Raman-Spektroskopie, gezeigt, dass sich die Oligomere tatsächlich in den Poren der SURMOFs geformt haben. Elektrochemische Impedanzspektroskopie (EIS) wurde durchgeführt, um die elektrische Wechselstromleitfähigkeit von Cu(bpdc)-Dünnfilmen nach der Oligomerisierung von EDOT zu messen. Die Messungen der elektrischen Leitfähigkeit für PEDOT-beladene SURMOF-Dünnfilme ergaben eine Erhöhung der elektronischen Leitfähigkeit, die eine entscheidende Rolle für die Verwendung der polymerbeladenen SURMOF-Dünnfilme in elektronischen Anwendungen spielt.

Die zweite Studie behandelt die Pd-katalysierte Polymerisierungsreaktion von Methyl Propiolat (MP). Poly-Methyl Propiolat wurde in den Porensystemen von drei verschiedenen SURMOFs

synthetisiert: Cu(bpdc), $Cu_2(bdc)_2(dabco)$ und HKUST-1. Diese drei SURMOF-Systeme wurden aufgrund ihrer unterschiedlichen Arten von Porenfenster, Porenkanälen und Porenvolumina als Template für die Polymerisationsreaktion ausgewählt. In die SURMOF-Strukturen wurde MP in Gegenwart von Spuren von $PdCl_2$ als Katalysator in die Poren der SURMOFs geladen und dann bei erhöhter Temperatur polymerisiert. Polymer-SURMOF-Komposite wurden dann unter Verwendung der Röntgendiffraktometrie (XRD), Rasterelektronenmikroskopie (SEM), energiedispersive Röntgenspektroskopie und Mapping (EDXS, EDXM), Rasterkraftmikroskopie (AFM), Flugzeit-Sekundärionen-Massenspektrometrie (ToF- SIMS), MALDI- ToF/MS, Quarzkristall Mikrowaage (QCM) und Strom-Spannungs-Messungen untersucht. Die XRD-Analysen zeigen, dass die MP-Beladung in SURMOFs und die Polymerisation in SURMOFs die Intensität der Reflexe und die Formfaktoren leicht beeinflussten. Die Kristallinität der SURMOF-Strukturen blieb jedoch unverändert. Weitere experimentelle Untersuchungen, die mit SEM und EDXM durchgeführt wurden, zeigten eine Polymer-Deckschichtbildung für Cu(bpdc) und $Cu_2(bdc)_2(dabco)$, während bei HKUST-1 keine Deckschichtbildung beobachtet wurde. Der Grund für die Bildung der Polymerdeckschicht wurde durch QCM-Analyse untersucht, die eine depotartige langsame Auswärts-Diffusion von MP aus Cu(bpdc) zeigen, während eine schnelle Desorption aus HKUST-1 stattfindet. Eine depotartige langsame Desorption von MP aus Cu(bpdc) begünstigt also die Bildung der Polymerdeckschicht während der Synthese. Darüber hinaus zeigten ToF- SIMS-Analysen, dass die Polymerisation innerhalb aller drei SURMOFs trotz der Bildung der Polymerdeckschicht in Cu(bpdc) und $Cu_2(bdc)_2(dabco)$ auftrat. Eine Kontrolle der maximalen Kettenlängen und Größenverteilung für die Polymere konnte auch erreicht werden. Da HKUST-1 das bestes SURMOF Modellsystem für die Polymerisationsreaktion von MP in den Poren ist, wurde die Gleichstromleitfähigkeit für HKUST-1 nach MP-Polymerisation gemessen. Eine Erhöhung der elektrischen Leitfähigkeit um 6 Größenordnungen im Vergleich zu leerem HKUST-1 wurde beobachtet. Elektrische Leitfähigkeit in SURMOF Dünnfilmen ist potentiell für unterschiedlichen Anwendungen nutzbar, z.B. in Sensoren und in der Mikroelektronik.

1. INTRODUCTION

1.1 Metal-Organic Frameworks

Metal-organic frameworks (MOFs), also called porous coordination polymers (PCPs), are highly porous and crystalline hybrid materials, which consist of inorganic metal nodes (metal ions or metal-oxo clusters) and organic ligands, as shown in Figure 1.1.[1, 2] Since the term "MOF" was first presented by Omar Yaghi in 1995[3], it has received increasing attention in late 1990s.[4] In the past decades, over 70.000 crystalline MOF structures have been discovered.[5]
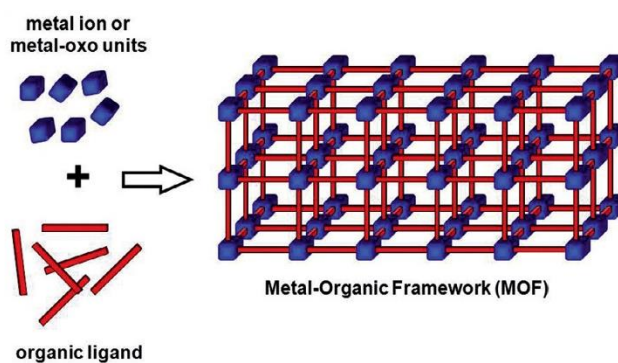
Figure 1.1 : The formation of metal-organic framework (MOF) by connecting the metal nodes with the organic ligand (Figure taken and partially modified from ref.[2]).

The inorganic metal nodes in the MOF frameworks can be metal ions (e.g. Zn(II), Cu(I), Cu(II), Co(II), Mn(II), Al(III), Cr(III), Fe(III)) or clusters (e.g. $Zn_4O(COO)_6$, $Cu_2(COO)_4$, $Cr_3O(H_2O)_3(COO)_6$ and $Zr_6O_4(OH)_{10}(H_2O)_6(COO)_6$), whereas the organic ligands (linkers) contain mostly carboxylate, phosphanate-, pyridyl-, and imidazolate functional groups. Combination of different linkers with different inorganic metal nodes yields diverse framework topologies.[6] Secondary building units (SBUs) are an important concept to describe the topology of MOFs and describe the coordination of the metal center/cluster.[7] Transition-metal carboxylate clusters are important as SBUs for the design of directionality in constructing MOFs and obtain robust frameworks.[8]

Paddle-wheel SBUs are mostly known and well-studied until today.[9] This complex is based on metal (II) carboxylates $[M_2(COO)_4]$. Copper- and zinc-paddlewheel based MOFs are the examples in this class and they have two advantages. Firstly, paddle-wheel SBUs can be formed in

energetically favorable conditions of solvothermal reactions. Secondly, the solvents can be removed by an activation process, which results in generating open metal sites.[10, 11]

In general, MOFs can show ultrahigh porosity and large inner surface area and thus, ultralow densities, by tuning the pore size and functionality.[12-14] Some examples of MOF structures are shown in Figure 1.2. HKUST-1 (Hong Kong University of Science and Technology-1) was first published by Williams et al. in 1999[15] following the publication of MOF-5 by Yaghi et al.[16] HKUST-1 consists of copper clusters and benzene tricarboxylate linkers, whereas MOF-5 consists of zinc-based clusters and benzene dicarboxylate linkers.[4] In most cases, MOFs are named as by the university at which they were found, followed by a number. Examples for that are the series of the MOFs; HKUST-1 (Hong Kong University of Science and Technology-1), MIL-53 (Matériaux de l′Institut Lavoisier-53)[17], UiO-66 (Universitetet i Oslo-66).[18]
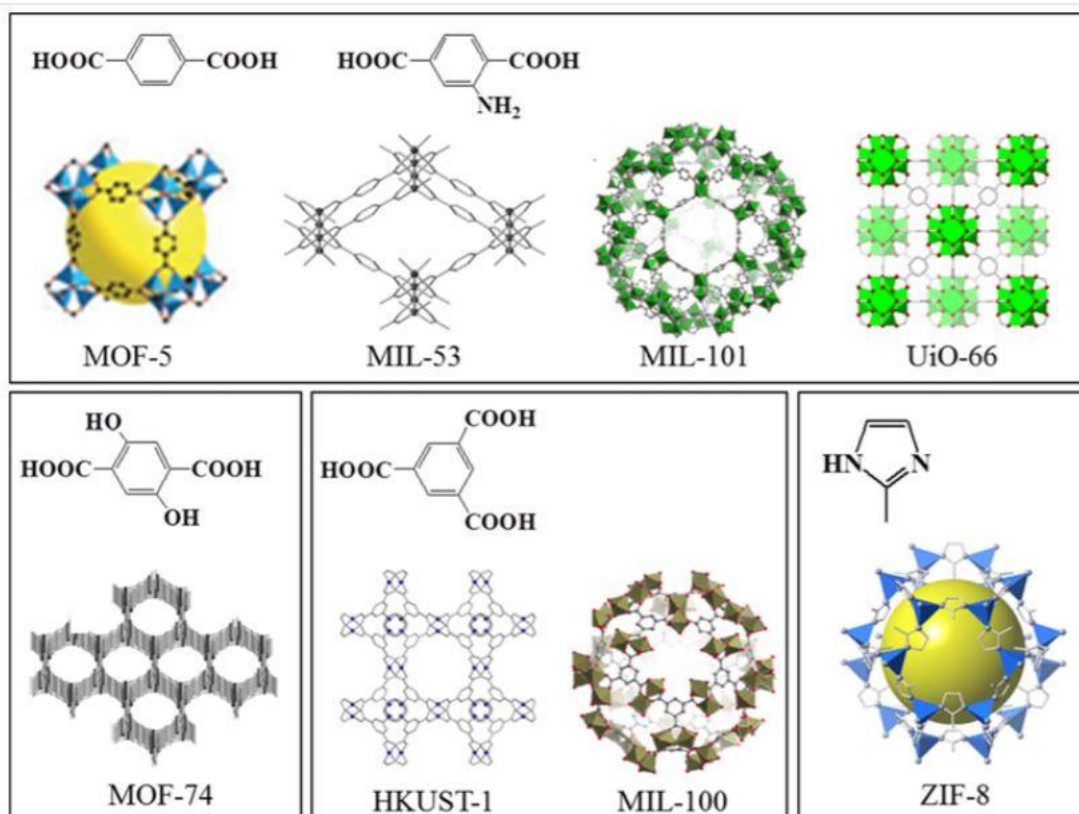

Figure 1.2 : Some examples of MOF structures (Figure taken from ref.[19]).

Different synthesis methods for MOFs has been reported in the past decades. These methods are mainly conventional solvothermal synthesis, microwave-assisted heating, mechanochemistry, electrochemistry, sonochemistry or formation at room temperature, as shown in Figure 1.3. In

addition to the conventional step-by-step methods, there are also high-throughput methods. The method for the synthesis of MOFs should be chosen regarding to the applications.[20] The solvothermal method is one of the easiest techniques for the preparation of MOFs, because the all reactants (metal salts, linkers and solvent) are mixed in an autoclave at the same time followed by heating them to an elevated temperature to obtain crystalline MOF product at the end.[21]
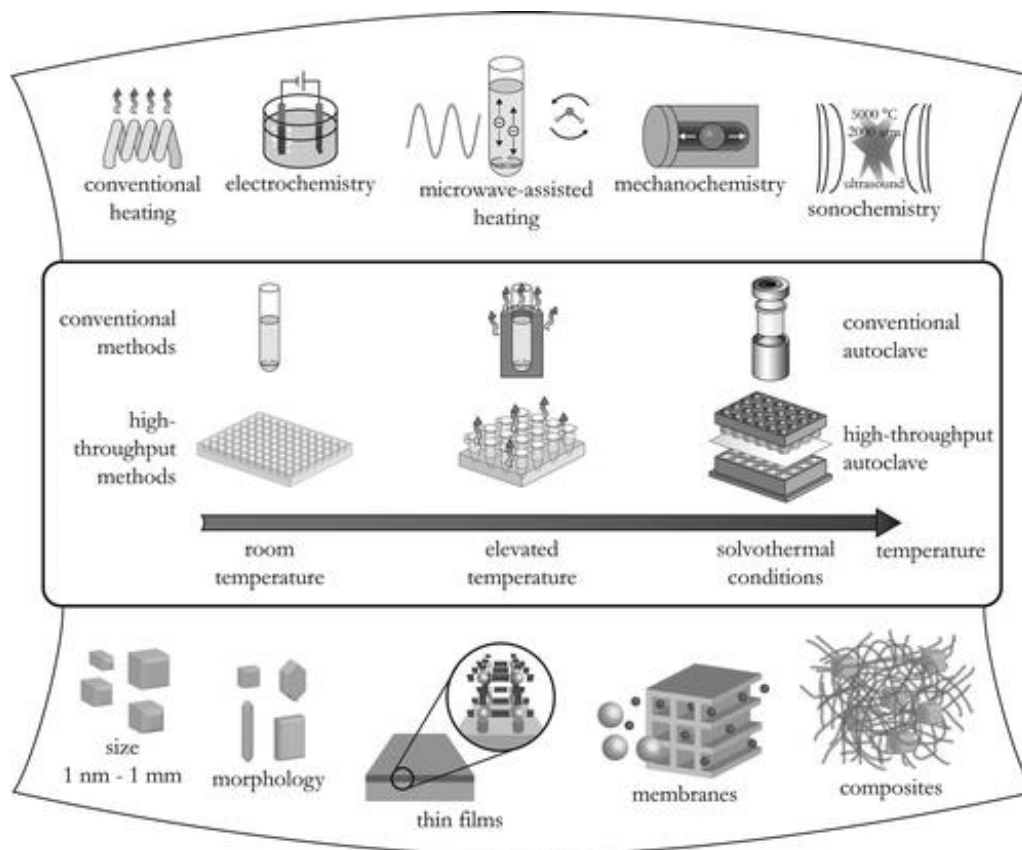
Figure 1.3 : Overview of MOF synthesis methods with feasible reaction temperatures and reaction products (Figure taken from ref.[20]).

Since MOFs can show high porosity, high surface area, chemical and thermal stability[22] and they can have electrical, magnetic, optical and catalytic properties by choosing the proper metal source and designed ligands[23], they can be used in different kind of fields such as separation[24, 25], gas storage[26, 27], catalysis[28, 29], drug delivery[30, 31], sensing[32, 33] and controlled polymerizations.[34, 35]

1.2 Surface-Mounted Metal-Organic Frameworks

In the last decades, the fabrication of MOF thin films on different kind of substrates has become important for the researchers in order to use them in MOF-based devices.[36, 37] Many techniques

have been developed to synthesize MOF thin films such as liquid phase epitaxy (LPE)[38], colloidal[39], Langmuir-Blodgett (LB) depositions[40], reactive seeding[41], electrophoretic deposition[42], microwave assisted film formation[43], and gel-layer deposition.[44] The homogeneity and thickness of the films are their key factors for the properties of SURMOFs, alongside with film roughness, crystal alignment, size of the crystals, domain size of the crystals, substrate adhesion and several mechanical features.[45]

Liquid phase epitaxial growth (LPE) has been developed in order to deposit highly crystalline and homogenous MOF thin films on the substrate surfaces in a controllable layer-by-layer mode (LBL).[46] C. Wöll and R. A. Fischer reported firstly these thin MOF films prepared by LPE in 2007, which referred to as surface-mounted metal-organic frameworks (SURMOFs).[47, 48]

1.2.1 Substrates and surface functionalization of SURMOFs

The selection of proper substrates and appropriate surface modifications are important factors to synthesize SURMOFs. Planar solids like gold, silicon, silicon oxide, glass, quartz, alumina, FTO, ITO; flexible materials like plastic, non-planar substrates like metal oxide and metal foams are some examples of substrates used for the growth of SURMOFs.[49]

Before the epitaxial growth of SURMOFs on e.g. Au surfaces, firstly the surface should be functionalized. Self-assembled monolayers (SAMs) are mostly used for the functionalization of Au substrates. The principle relies on covalent bonding of surfactant thiols on surfaces of Au substrates for the formation of an ordered monomolecular layer. The structure of SAM is shown in Figure 1.4. The structure involves a head group, tail group and functional end group. In general, the head group can consist thiols, silanes or phosphonates, the tail group can consist alkyl chains, whereas functional end groups can be -OH[50], -COOH[51], -NH$_2$[52], -CH$_3$[53] or pyridyl.[54, 55] Initial reactants is linked with these functional end groups.[56] In this study, Au surfaces are functionalized with 16-mercaptohexadecanoic acid (MHDA), which has the end group is -COOH, and 11-mercapto-1-undecanol (MUD), which has the end group of -OH.[57]
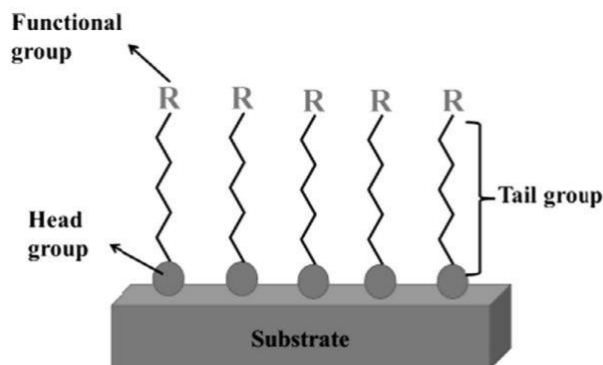
Figure 1.4 : Structure of self-assembled monolayer (SAM) (Figure taken from ref.[54]).

1.2.2 Liquid phase epitaxy

As mentioned above, LPE is one of the methods, which has importance to grow highly oriented SURMOFs on functionalized substrates with defined thickness.[57] The key steps of this process are the adsorption of constituents from the liquid phase to the surface in stepwise, layer-by-layer (LBL) fashion.[58] As shown in Figure.1.5, the procedure involves the steps as follows[59]:

- First of all, after the functionalization of SURMOFs by SAMs, the sample is immersed in metal ions solution, where the functional end groups of SAMs bind the metal units by coordination bonds.

- The second step is to rinse the substrate with pure solvent in order to remove physically adsorbed metal units.

- Following the rinsing step, an immersion into the organic linker solution is applied, which results in binding of linker molecules with the metal units, which were fixed before.

- Then, the surface is rinsed again. Since there are free functional groups after rinsing to deposit the metal units, this process can be applied as a cycle afterwards.

5
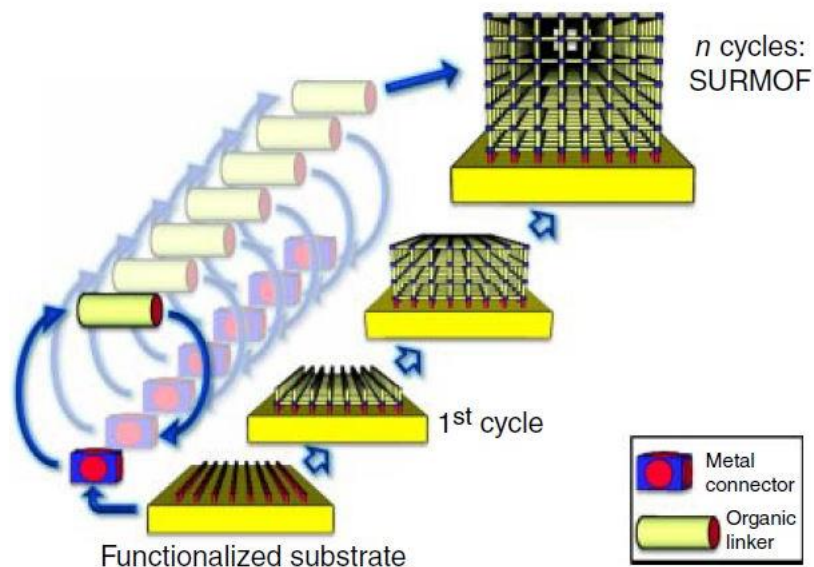
Figure 1.5 : Schematic of SURMOF synthesis by layer-by-layer method on a functionalized substrate (Figure taken from ref.[60]).

One unit cell is formed ideally by one cycle of the deposition and the number of deposition cycles determines the thickness of SURMOFs. The orientation of the SURMOF growth can be controlled by appropriate chosen of the functional groups in SAMs.[59]

The first SURMOF synthesized by LBL LPE method was HKUST-1, which was grown in [100] orientation on MHDA SAMs.[53] HKUST-1 is comprised of copper(II) acetate and 1,3,5-benzenetricarboxylic acid (btc), where copper(II) acetate binds to the SAM following btc linked to the copper(II) acetate.

If LPE is compared with other methods for MOF thin film preparation, it has many advantages over the other methods.[46] The thickness can be controlled by changing the number of deposition cycles.[61] Crystal orientation can be controlled to obtain perfectly oriented films by proper selection of the functionalized surface.[47] Moreover, homogenous morphology in MOF thin films can be obtained with small roughness.[62] Compared to the conventional methods for bulk MOF synthesis (powder MOF), defect density is lower in MOF thin films.[63]

1.2.3 Preparation methods of SURMOFs

Different techniques such as spray-[2], pump-[64], dipping-[65], and quartz crystal microbalance (QCM)-method[66] have been developed in order to synthesize SURMOFs. The techniques used for the synthesis of SURMOFs in this study will be explained in the following section.

1.2.3.1 Spray method

The spray method is one of the high throughput approaches to synthesize thick SURMOF films. Since the preparation of SURMOF films with the thickness above 100 nm takes long time by using conventional methods, spray method has several advantages to obtain thick SURMOF films in a shorter time.[2] Figure 1.6 shows the schematic of the production of SURMOF films by using spray method. This method depends on layer-by-layer synthesis procedure. This system depends on the production of aerosol from reactants' solution with a small nozzle. Deposition of material occurs by contacting the droplets of the aerosol with the substrate.

The procedure of one deposition cycle in the spray method to synthesize SURMOFs as the following:

- Firstly, solution of metal-containing reactant is subsequently sprayed on the functionalized substrate for 15 seconds.

- Then, 35 seconds are waited and the substate is rinsed by ethanol for 5 seconds.

- After the rinsing step, solution of linker-containing reactant is subsequently sprayed on the substrate for 25 seconds and waited again for 35 seconds.

- Finally, the substrate is rinsed with ethanol for 5 seconds.

As seen in the procedure, each deposition cycle takes 2 minutes. The number of deposition cycles depends on required thickness of SURMOF. By using this technique, SURMOF films with a thickness of 1 µm can be prepared in a few hours.
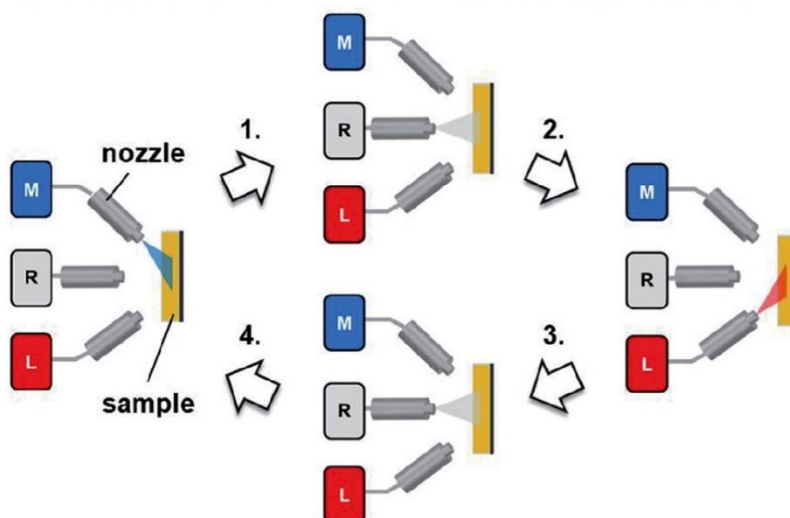
Figure 1.6 : Schematic of the synthesis of SURMOFs by spray method (M:Metal, R:Rinsing, L:Linker; figure taken from ref.[2]).

1.2.3.2 Pump method

The pump method is another method for the synthesis SURMOF films in order to control the temperature ranging from -20 to 100 ˚C during the synthesis.[64] The schematic diagram for the LBL growth of SURMOF using pump method is shown in Figure 1.7. This system consists of four pumps. Three pumps are used to pump the metal solution, linker solution and ethanol to the sample cell, whereas the fourth pump is used in order to pump out the solution from the sample cell. Like spray method, ethanol is used to remove the excess reactants. In this thesis, 65 ˚C was used as synthesis temperature. The procedure of SURMOF synthesis using pump method as the following:

- Firstly, metal solution is pumped into the sample cell, where the functionalized substrates are placed.

- Then, the metal solution is pumped out from the sample cell and ethanol is pumped into the cell in order remove excess reactants. The sample was rinsed with ethanol.

- After the rinsing step, the linker solution is pumped into the sample cell.

- In order to complete first deposition cycle, linker solution is pumped out completely again from the sample cell and ethanol is pumped into the cell to remove the excess linker molecules. As a final step, ethanol is also pumped out.

Immersion times for the synthesis of SURMOFs in this thesis were 10 min for metal solution, 2×2 min for ethanol rinsing, 15 min for linker solution and again 2×2 min for ethanol rinsing at the end of deposition cycle. Depending on the type of SURMOF the settings parameter can be changed.
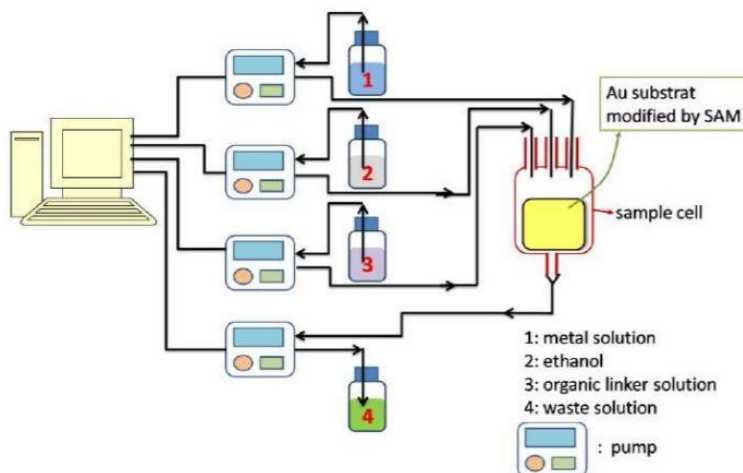
Figure 1.7 : Schematic diagram of the pump method for the synthesis of SURMOFs (Figure taken from ref.[64]).

1.3 Polymerization in MOFs

As stated above in Chapter 1.1, MOFs have different application areas including polymer science, where the nanochannels' structure of MOFs are playing an important role. Since the channel properties of MOF such as pore size and dimensions, regularity and shape of the channels, and functionality can be changed by proper selection of metal ions and organic linkers, polymer features (e.g. orientation of polymer chain, polymer arrangement, amount of polymer chains, environment of the polymers) can be controlled.[35, 67] Figure 1.8 indicates the number of published polymer/MOFs papers starting from 2005, which is a sign of the importance of this topic over the years compared to the conventional bulk polymerization reactions.[67]

Figure 1.8 : The number of publications about the polymer/MOF combination (Figure taken from ref.[67]).

The research group of S. Kitagawa and Uemura at Kyoto University in Japan first published a paper about the styrene polymerization by heating in the presence of initiator in $Zn_2(bdc)_2(dabco)$ MOFs[68] following further publications about the polymerization inside MOFs.[69] However, confining polymerization reactions inside the pores of MOF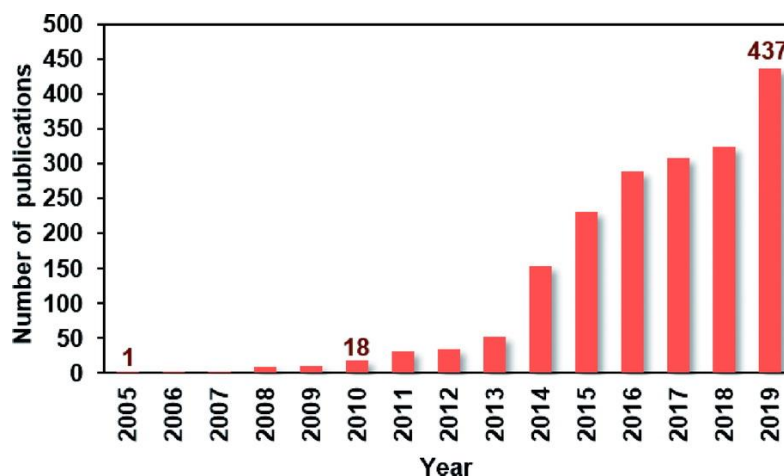s have been performed by using different types of polymerization methods such as radical polymerization[68, 70-74], oxidative polymerization[75-79], ionic polymerization[80, 81] and cycloaddition polymerization.[82]

Radical polymerization is one of the well-studied method to control the polymerization of vinyl monomer inside the MOFs.[68, 70-74] Reviewing the literature, radical polymerization inside the MOFs results in controlling the polymer within the scope of molecular weight (narrow molecular weight distribution)[68, 71], stereostructure[71], reaction sites[72] and sequence of copolymer.[70, 83]

Oxidative polymerization in MOFs is another useful method in order to prepare MOF-polymer composites for electronic devices, because it was shown that the optical and electronic properties of the resulted polymer can be controlled.[75-77, 84]

However, literature review shows that SURMOFs have not widely been used as templates for the polymerization reactions. Self-polymerization of 3,4-dihydroxy-L-phenylalanine (L-DOPA) by UV light irradiation was carried out in the pores of HKUST-1 for enantioselective adsorption of the drug naproxen, which was an innovative study in order to fabricate the homochiral polymer thin films by using of SURMOF.[85] Furthermore, a HKUST-1 thin film was used to synthesize electrochemically 3D porous conductive polymer, polyaniline.[86] Besides these studies, thiophene monomers were oxidatively polymerized in HKUST-1 thin film, where HKUST-1 initiated the

10

polymerization reaction by heating. In this mechanism, there was no need of oxidative agent or catalyst for the initiation of polymerization reaction.[84] Another publication shows the electropolymerization of 1-hexyne, monosubstituted acetylene, in the 1D channels of SURMOF-2 (Cu(bdc)) resulting in an increase of electroconductivity after polymerization compared to the pristine SURMOF-2.[87]

2. THEORETICAL BACKGROUND OF THE CHARACTERIZATION TECHNIQUES

2.1 X-Ray Diffraction

X-ray diffraction (XRD) is well-known and widely used technique in order to determine the atomic and molecular structure of a crystalline material.[88] First XRD experiments on a single crystal were performed in 1912 by Laue[89] and then XRD became an important role to investigate the unknown crystalline materials in different fields such as material science, geology, mineralogy, engineering and biology.[90] The principle of XRD depends on constructive interference of monochromatic X-rays within the crystalline sample. Monochromotic X-ray is elastic scattered by core electrons of atoms in a sample to produce XRD signal. Since the crystalline sample has regularly-spaced atoms in a lattice, it results in diffraction of X-rays, which produce XRD patterns.[88] W. H. Bragg and W. L. Bragg had presented Bragg's law in 1913, which describe the relationship between the wavelength of the incident X-rays, angle of incidence and distance between the crystal lattice planes of atoms (Figure 2.1). The equation of Bragg's law is as follows:

$$n\lambda = 2d \sin\theta$$

In this equation, λ is the wavelength of X-ray, n is the integer number of diffraction order, d is the distance between the planes and θ is the scattering angle between the plane and X-ray.
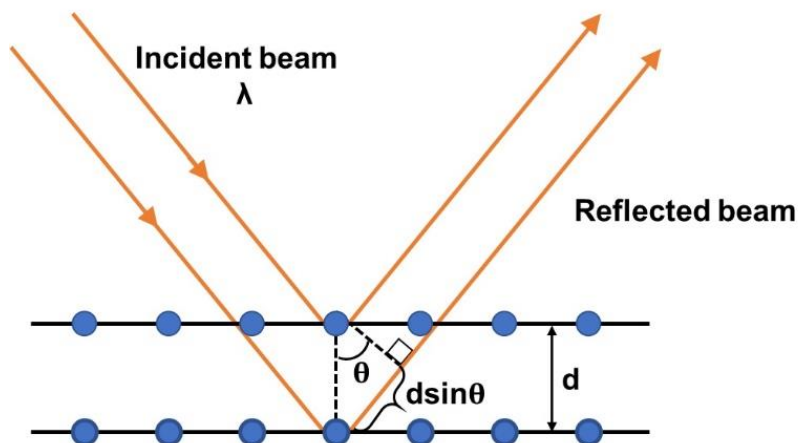

Figure 2.1 : Schematic of XRD showing the parameters of Bragg's law. Black solid lines represent crystalline plane with a distance, blue circles represent atoms.

X-ray diffractometers includes basically three main units: X-ray tube, a sample holder and an X-ray detector (Figure 2.2).[91] Generation of X-rays occurs in a cathode ray tube, in which a filament

is heated up to produce electrons. Voltage is applied in order to accelerate the electrons towards a metal target, e.g., Cu, Mo or Cr. The target material is bombarded with the electrons. In case electrons have enough energy to dislocate the inner shell electrons of the target material, specific X-ray spectra are produced. Crystal monochrometers is used for the production of monochromatic X-rays, which is required for diffraction. These X-rays are collimated and directed to the crystalline sample and then reflected X-rays are recorded by the detector, which converts them into the signal to see on the computer.[90]
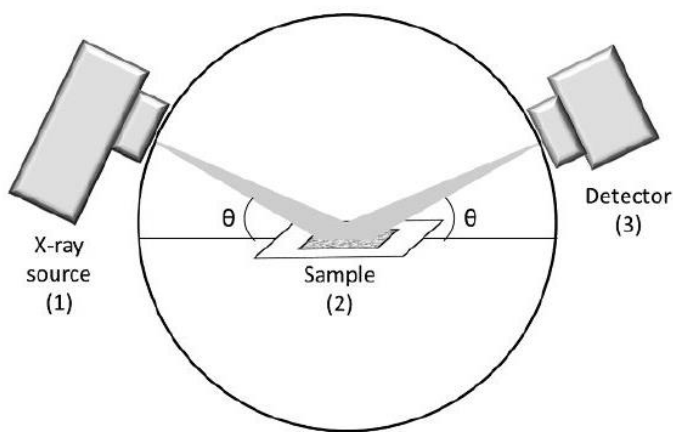
Figure 2.2 : Schematic of X-ray diffraction setup (Figure taken from ref.[91]).

Powder materials have a random orientation distribution of crystallites resulting in measurement of all diffraction peaks, whereas thin films like SURMOFs have an anisotropy. Hence, in-plane and out-of-plane XRD techniques are important to determine the structure and orientation of the thin films. As shown in Figure 2.3, in-plane XRD is a technique in order to determine the distances of the lattice planes, which is normal to the substrate surface. On the other hand, out-of-plane XRD is technique to determine the distances of lattice planes, which is parallel to the substrate surface. By using of out-of-plane XRD, only crystallographic information in one direction can be obtained, whereas more detailed information can be achieved by using of in-plane XRD.[92]

Figure 2.3 : Schematic of (a) out-of-plane and (b) in-plane XRD measurements of a thin film (Figure taken from ref.[93]).

2.2 Infrared Spectroscopy

Infrared (IR) spectroscopy is a technique based on the absorption of infrared light by a substance to be measured, which causes vibrations of the atoms of a molecule. It can be used for the identification of chemical structures. Infrared region in the electromagnetic spectrum is between the visible and microwave region 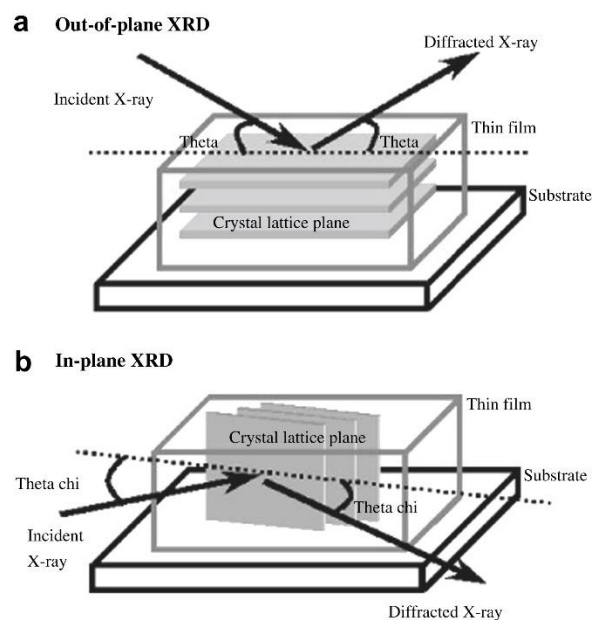and divided into 3 regions, which are near- (wavelength: 0.8-2-5 µm), mid- (wavelength: 2.5- 25 µm), and far-infrared wavelength: (25-1000 µm).[94, 95]

When the frequency of IR match with the frequency of molecular vibrations and rotations, the absorption occurs. A change in dipole moment of the atoms during the vibration is required for the absorption of IR light. When the change in dipole moment is greater, IR absorption band will be also stronger. IR inactive means that the molecule has no dipole moment.[94]

IR absorption can be described by the help of a model of a harmonic oscillator. If atoms are seen as particles with a known mass, a diatomic molecule contains masses m1 and m2 connected by a spring with a force constant k, which based on the bond strength between the atoms. The distance between these two masses is r at equilibrium. A restoring force F is produced with the stretch of the molecules. If the spring is released, vibration occurs around the equilibrium position of the system. The energy E, vibrational frequency v of a diatomic molecule can be calculated, where µ

15

is the reduced mass and Δx is the sum of distance change of the masses during the vibration as follows:

$$\nu = \frac{1}{2\pi}\sqrt{\frac{k}{\mu}}$$

$$\mu = \frac{m1 \cdot m2}{m1 + m2}$$

$$E = \frac{1}{2} \cdot k \cdot \Delta x^2$$

Harmonic oscillator is a simplified model, which is valid for small displacements. Since greater displacements don't show harmonic oscillation, anharmonic oscillator model can be described. In the harmonic oscillator model, the potential energy is symmetric, whereas the potential energy is asymmetric in anharmonic model. The potential energy can be calculated by the Morse equation and the energy levels are not equally spaced, whereas equally spaced in harmonic oscillator model. There are mainly two important effects of this model. Firstly, the repulsion between the atoms increased very fast, when two atoms approach each other. Secondly, the molecule can dissociate with sufficiently large vibrational energy.[94] Figure 2.4 shows the energy levels of harmonic and anharmonic oscillator.[96]
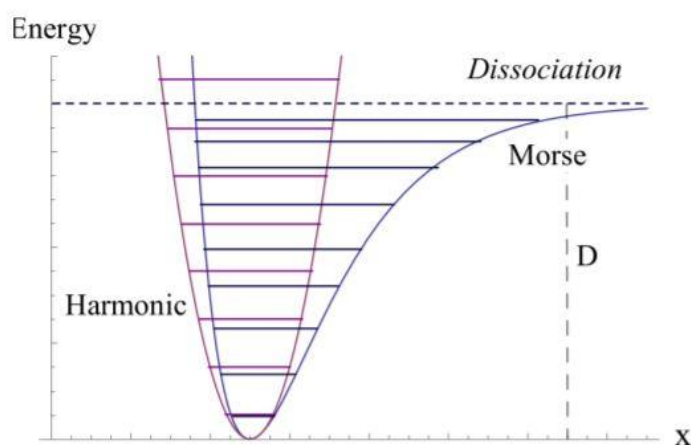

Figure 2.4 : Schematic of the energy levels for harmonic and Morse potential (Figure taken from ref.[96]).

Nowadays, mostly used mid-infrared spectrometers are Fourier transform spectrometer (FTIR). IR light source, interferometer, sample compartment, detector, amplifier and computer are the main parts of typical FTIR spectrometer. IR source produce IR light and the it is directed into an interferometer, which modulates the light. Then, the light passes through the sample compartment and reaches finally the detector. Afterwards, the signal is amplified and converted to the digital signal, which called as interferogram. Michelson interferometer, which is the core of FTIR spectrometer, consists of a beam splitter, fixed mirror and a mirror, which can move back and forth (Figure 2.5). The principle is based on the separation of incident light into two beams by the beam splitter. Beam splitter is responsible for transmitting 50% of the light and reflects the remaining part. One beam is directed to the fixed mirror, whereas the other beam is reflected to the moveable mirror. Then, the fixed and moveable mirrors reflect the light back to the beam splitter. The light reflecting from these two mirrors is recombined at the beam splitter, which have difference in path length. After the overlapping of both beams, they are directed towards the sample compartment and detected by the detector. Interferogram is collected and digitized by FTIR spectrometer, which performs the FT functions and shows the spectrum.[97]
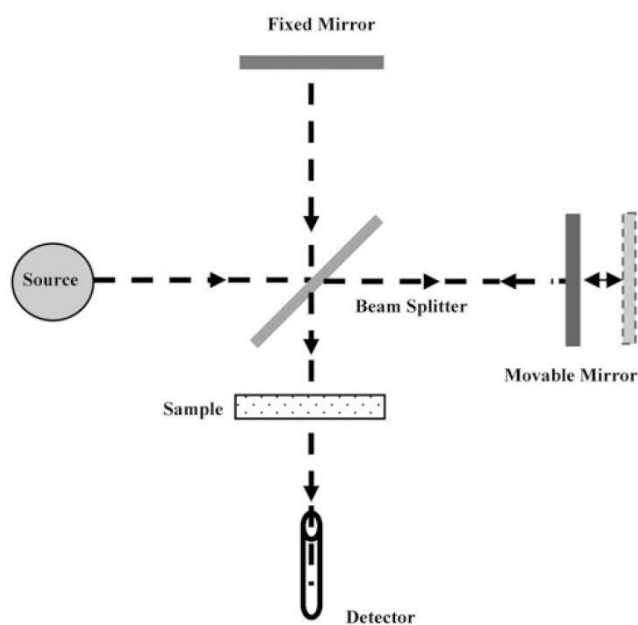

Figure 2.5 : Schematic of Michelson interferometer (Figure taken from ref.[98])

Infrared reflection absorption spectroscopy (IRRAS) is a technique to measure an infrared reflection absorption spectrum for the thin films on metal surfaces.[99] The principle is based on the reflection of incident IR beam, which is focused on the metal surface at a grazing angle and

detection of reflected light. IR light is composed of two parts, s-polarized and p-polarized. The electric vectors of IR light are shown in Figure 2.6. The electric vector of s-polarized light is perpendicular to the incident plane (E_s), whereas the electric vector of p-polarized light is parallel to the incident plane (E_p). For E_s, the electric field, which is formed by the incident light and the reflected light, is cancelled because of the change in phase by 180° as a result of reflection. For this reason, only p-polarized light has influence as probe light. The grazing incidence of p-polarized light is typically 80° in IRRAS experiments.[100]
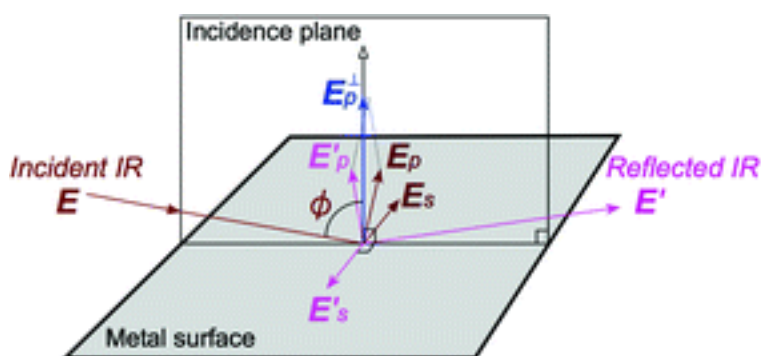
Figure 2.6 : Schematic of reflection of incident light with a grazing angle by the metal surface (Figure taken from ref.[100]).

Surface normal dipole selection rule is important term for IRRAS and shown in Figure. 2.7. This rule indicates that only vibrations, which have dynamic dipole moment perpendicular to the surface plane, can interact with p-polarized light. The reason of this rule is, when a molecule adsorbed on a metal surface, the dynamic dipole moment perpendicular to the surface is almost double together with its mirror image, whereas the dynamic dipole moment parallel to the surface is cancelled out each other.[100]

Figure 2.7 : Surface dipole selection rule, dynamic dipole moment perpendicular to the surface (left), parallel to the surface (right) (Figure taken from ref.[100]).

IRRAS is a powerful and reliable technique for chemical characterization of SURMOFs. It is shown that thin layer of molecules on metal surfaces like SAMs can be detected by using IRRAS without any destruction of the thin layer.[51] Furthermore, IRRAS can be used by checking specific bands of SURMOFs to determine whether SURMOF is successfully grown on the substrate.[101] Post-synthetic modification of SURMOFs can be also investigated by using this technique in order to observe the characteristic chemical bands after the modifications.[102] Moreover, IRRAS is also an useful technique to prove the oligomerization/polymerization inside the SURMOFs as it will be shown in this thesis.

2.3 Raman Spectroscopy

Raman spectroscopy is another vibrational spectroscopic technique in order to provide information about the chemical structure like in IR spectroscopy. The main difference between Raman and IR spectroscopy is that no dipole moment is required for Raman active molecules, so it is complementary to IR spectroscopy. The principle is based on the Raman effect, which is found out by Sir C. V. Raman in 1928. There is a correlation between polarizability of the electrons and Raman effect. A change in polarizability during the vibration is required for the Raman active molecules to be observed in Raman spectra. When the light is scattered from a molecule, the main percentage of the scattered light is Rayleigh scattering (elastic scattering), whereas the other small percentage ($\sim 10^{-5}$ of the incident light) of this light is Raman scattered (inelastic scattered) light.[98, 103, 104] The energy diagrams are shown in Figure 2.8.

The frequencies of the incident beam (ν_0) and Rayleigh scattering is the same. The frequency of Raman scattered light is $\nu_0 \pm \nu_m$, where ν_m is the vibrational frequency of the molecule. Raman scattered light is scattered with a shift in energy as a result of interaction of the incident light and the vibrational energy levels of the molecules, so this light can have less energy (Stokes) or more energy (anti-Stokes) energy compared to the incident light.[98]
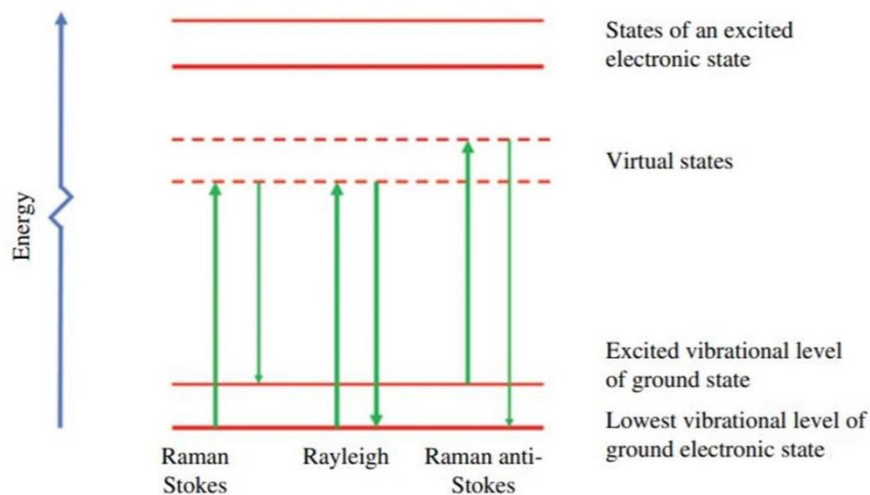
Figure 2.8 : Energy diagrams of Rayleigh, Raman (Stokes, and anti-Stokes) scattering (Figure taken from ref.[104]).

Since Raman spectroscopy is a complementary technique to IR spectroscopy, it is useful for the analysis of SURMOFs together with IRRAS. The literature review shows that Raman can be used to detect Glaser-Hay coupling reaction in SURMOF[105], to determine the presence of guest molecules in SURMOF[87] or to observe the changes in chemical structures of SURMOFs after the catalytic reactions.[106]

2.4 Ultraviolet-Visible Spectroscopy

Ultraviolet-visible (UV-vis) spectroscopy is a commonly used technique to characterize and determine quantitively the substances. The principle is based on the electronic transitions in substances by absorption of ultraviolet light (UV, 200-400 nm) or visible light (Vis, 400-800 nm). When the light is absorbed by the material, the electrons within the materials undergo excitation, which causes absorption spectrum. Since UV and visible light has enough energy to promote electrons to higher energy levels, excitation results in jumping of electrons from ta ground state to an excited state, which has higher energy level. Three types of electrons can exist in the outer shell of electrons, which are σ-, π- and n- (lone pair) electrons. Figure 2.9 shows the energy level diagrams with electronic transitions of σ-, π- and n-electrons. σ* and π* represent anti-bonding orbitals. The σ-bond electrons are found at the lowest energy level and higher energy are needed for the excitation. The π-bond electrons are at higher energy levels compared to σ-bond electrons.

Since they are not really stable, lower energy is required for excitation. Non-bonding electrons (n-electrons) are found at higher energy levels than the π-bond electron. It should be noted that energetically favored promotion of electrons occurs from the highest occupied molecular orbital (HOMO) to the lowest unoccupied molecular orbital (LUMO).[107, 108]
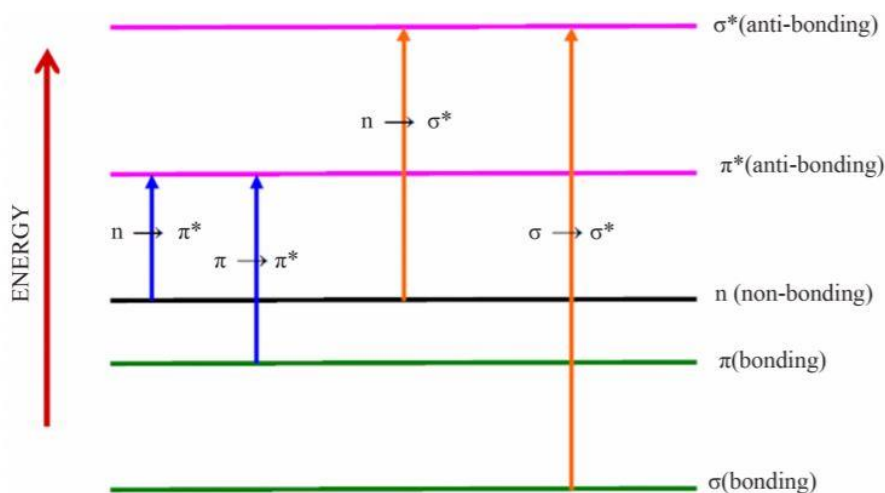
Figure 2.9 : Energy level diagrams with electronic transitions of σ-, π- and n-electrons (Figure taken from ref.[107]).

The principle of UV-Vis spectroscopy follows Beer-Lambert law, which indicates that the absorption of the light is proportional to the number of absorbing molecules and intensity of the source does not affect the absorption of the incident light. The Beer-Lambert law can be shown as:

$$A = log_{10} \frac{I_0}{I} = \varepsilon l c$$

where A describes the absorbance, I_0 is the intensity of the incident light, I is the intensity of the transmitted light, ε is the molar extinction coefficient, l is the path length of the absorbing solution and c is the concentration of the substance.[109]

UV-Vis spectroscopy can be utilized for the characterization of optical properties of SURMOFs. Reviewing the literature shows that UV-Vis spectroscopy is a powerful technique, e.g. to investigate the photoswitchable MOF films[110, 111], to check the absorption of molecules inside the SURMOF[106] or to investigate the smoothness of SURMOFs.[65]

2.5 Mass Spectrometry

Mass spectrometry (MS) is one of the analytical techniques, which is based on measurement of mass-to-charge ratios of the analyzed samples in order to identify of unknown compounds and quantify the composition of the molecules. The structure and chemical properties can be determined by using mass spectrometry. Mass spectrometry mainly consists of ion source, mass analyzer and ion detector. First step of this technique is the ionization of the compounds in the ion source compartment, which is resulted in fragmentation. Then, the fragments are separated according to their mass-to-charge ratio and are detected to produce the mass spectrum. Mass spectrum shows a plot of ion abundance against to mass-to-charge ratio (m/z). Since the ionization of the analyzed sample occurs by bombardment of the analyte with electron beams in old MS techniques and it causes fragmentation of the sample into many units, which is not always desired, soft ionization techniques like electrospray ionization (ESI) and matrix-assisted laser desorption ionization (MALDI) were developed.[112, 113]

In this part, the principle of mass spectrometric techniques used in this study will be explained.

2.5.1 Matrix-assisted laser desorption ionization time of flight mass spectrometry

Matrix-assisted laser desorption ionization (MALDI) was developed in 1985 as soft ionization technique.[112, 114] Matrix-assisted laser desorption ionization time of flight mass spectrometry (MALDI-ToF/MS) is widely used techniques in different areas like polymer chemistry, nanotechnology, biochemistry, organic chemistry and medicine. As mentioned before, the principle of MALDI-ToF/MS is based on production, separation and detection of gas-phase ions to analyze large molecules, such as polymers, lipids. oligosaccharides and proteins.[115] MALDI-ToF process consists of two phases; ionization phase and time of flight phase (ToF) shown in Figure 2.10. Firstly, crystalline structured small organic compound called as "matrix" is required in ionization phase to embed the sample into the matrix. After the inserting matrix into the sample, the sample is irradiated by UV-laser in vacuum, which led to desorption of the molecules and ionization at the same time. Then, they are accelerated in an electrical field into the ToF device, which is the second phase. In this phase, TOF device is responsible for separation of the accelerated ions of different m/z ratios. Principally, ions with smaller m/z value and highly charged ions reach faster to the detector by passing field-free drift tube drift space. After the ions are detected, specific molecular mass can be calculated from the signals.[115-117]
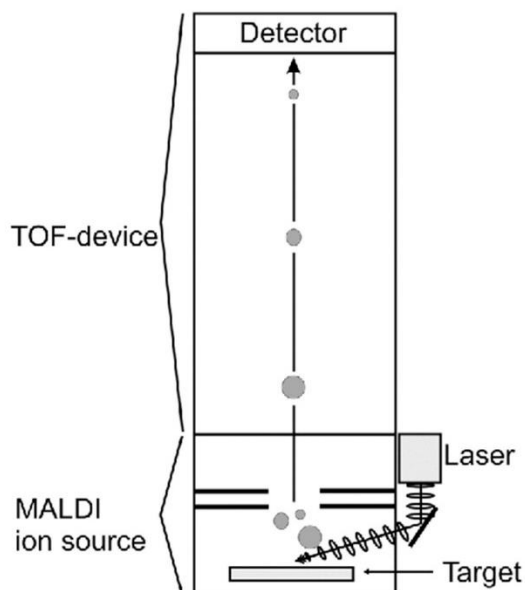
Figure 2.10 : Schematic drawing of MALDI-ToF/MS (Figure taken and partially modified from ref.[115]).

MALDI-ToF/MS is one of the important techniques used in this thesis to get the mass spectrum of the polymers, which were formed inside the SURMOFs. Besides, it can be used to analyze hybrid SURMOF materials, such as SURMOF/LeuH hybrid (layered europium(III) hydroxychloride).[106] In this study, the main drawback was to detect the polymers formed inside the SURMOFs by using ESI/MS or MALDI-ToF/MS because of their low concentration. During this study, it was faced the difficulties for the digestion of SURMOFs in order to characterize the polymers, which will be discussed in detail in Chapter 4.1.4.

2.5.2 Time-of-flight secondary ion mass spectrometry

Time-of-flight secondary ion mass spectrometry (ToF-SIMS) is a surface-sensitive analytical technique, which provide elemental and molecular information of a surface in high resolution. The surface is bombarded by energetic beam of primary ions, which results in production of different kind of sputtered neutral or charged "secondary" ions such as electrons, neutral molecules, atomic and cluster ions (Figure 2.11). Following of mass separation and counting of secondary ions, the secondary ions are detected by mass spectrometry. Depth profiling and 3D imaging are also possible besides having the mass spectrum of a surface, when a sputter ion source is applied to erode the sample with oxygen, cesium or argon cluster ions.[118-120] ToF-SIMS can be used to analyze the polymers, thin films on the surfaces or thiol self-assembled monolayers.
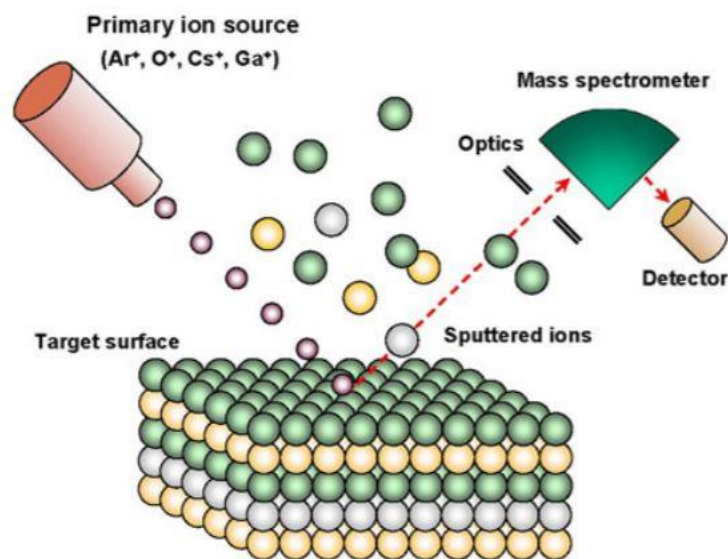
23

Figure 2.11 : The principle of secondary ion mass spectrometry (Figure taken from ref.[121]).

ToF-SIMS is another important technique in this study to investigate whether the polymerization occurred inside the SURMOFs by means of depth profiling. Additionally, depth integrated images can show whether the polymer distributed in SURMOF homogenously. Besides, ToF-SIMS is a useful technique for the characterization of chemical composition in specific areas in SURMOFs[122] or for the investigation of the dye loading in SURMOF.[123]

2.6 Scanning Electron Microscope and Energy Dispersive X-Ray Analysis

Scanning electron microscope (SEM) is a versatile technique for morphological characterization of materials. SEM is composed of electron gun (electron source and accelerating anode), electromagnetic lenses for focusing electrons, electron detector, sample chamber, scan generator, computer and screen to view the images as shown in Figure 2.12. The working principle of SEM is consisting of several steps. Firstly, generation of electrons occurs at the top of the column. Then, electrons are accelerated down by the anode following passing through a combination of lenses and apertures for the production of fine beam of electrons. The entire electron column should be in vacuum in order to prevent the oxidation and contamination of filament and also to decrease the collision between electrons and air molecules. Next, the surface of the sample is hit by the electron beams. The interaction of electrons within the sample allows to produce two types of electrons backscattered (BSE, primary electron beam) and secondary electrons (SE), which are used to image the sample. Scanning of the sample surface takes place, when the electron-beam coils are moved,

24

so it results in getting information about a specific area of the sample. The signals, which are produced by the interaction of electron beam with the sample, are detected by the detectors.[98, 124]
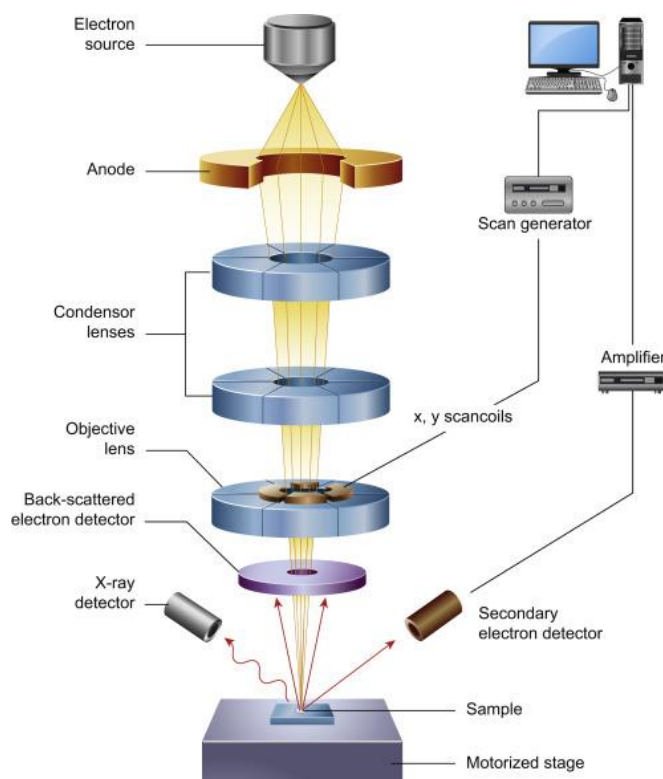
Figure 2.12 : Schematic of the main components of SEM microscope (Figure taken from ref.[125]).

Energy dispersive X-ray analysis (EDX), which is an attachment of SEM, can be used to determine the elemental composition of the samples. Specific X-rays are produced by hitting the electrons in high energy to the sample and they are detected by a semiconductor detector following conversion them into signals, which leads to have a spectrum indicating the peaks corresponding to the elements in the samples. Besides EDX is both qualitative, semi-quantitative and quantitative technique, elemental mapping can be also performed to get information about the spatial distribution of elements.[126, 127]

SEM together with EDX has an important role for the morphological analysis of SURMOFs, e.g. investigation of thickness or roughness of SURMOFs. In this study, the morphological changes before and after polymerization were recorded by SEM, which gave a hint how the thickness of SURMOF changed after polymerization and how polymer covered the SURMOF surfaces.

25

3. EXPERIMENTAL SECTION

3.1 Materials

Zinc acetate dehydrate (≥98%), copper(II) acetate monohydrate (≥98%), palladium chloride (99%), 11-mercapto-1-undecanol (MUD, 97%), 16-mercaptohexadecanoic acid (MHDA, 90%), 1,4-benzenedicarboxylic acid (bdc, 98%), 4,4- biphyenyldicarboxylic acid (bpdc, 97%), 1,3,5-benzenetricarboxylic acid (btc), 1,4-diazabicyclo(2.2.2)octane (dabco, ≥99%), 3,4-ethylenedioxythiophene (EDOT, 97%), trans-2-[3-(4-tert-Butylphenyl)-2-methyl-2-propenylidene]malononitrile (DCTB, ≥99%), hydrochloric acid (37%), glacial acetic acid (100%), tetrahydrofuran (THF, ≥99.9%) and chloroform (≥99.5%) were purchased from Merck, Germany. 2,2′:5′,2″-Terthiophene (Tth, 99%) and iron(III) chloride (98%) and methyl propiolate (99%) were obtained from Alfa-Aesar, Germany. Absolute ethanol (≥99.8%) was purchased from VWR chemicals. All chemicals were used without further purification.

The gold substrates used for SURMOF synthesis consisted of a 100-nm Au/5-nm Ti metal bilayer deposited on Si wafers. They were purchased from Georg-Albert-Physical Vapor Deposition (Silz, Germany).

Silicon wafers were purchased from Silicon Sense (US).

Quartz glass was obtained from GVB Solutions in Glass (Herzogenrath, Germany).

Interdigitated gold electrodes on glass substrates with a gap of 5 µm were purchased from Metroohm.

Gold coated QCM sensors was obtained from LOT-QuantumDesign (Darmstadt, Germany). The sensors have 14 mm of diameter, 0.3 mm of thickness and 4.95 MHz of fundamental frequency.

3.2 Functionalization of Substrates

3.2.1 Gold substrates

The gold substrates and gold coated QCM sensors were functionalized by SAMs of MHDA solution or MUD solution based on the type of SURMOF and its application.[56]

For MHDA functionalization, the gold substrates were immersed into 20 µM ethanolic solution of MHDA containing 10% (v/v) acetic acid for 3 days at room temperature and in dark conditions.

Afterwards, the substrates were rinsed with pure ethanol and dried under nitrogen stream in order to use in synthesis procedure.

For MUD functionalization, the gold substrates were immersed into 1 mM ethanolic MUD solution for 24 h. After the functionalization, they were rinsed with pure ethanol and dried under nitrogen stream in order to use in the synthesis procedure.

3.2.2 Silicon substrates

The silicon substrates were functionalized by using UV-ozone cleaner (Ossila, Sheffield, UK). Before the functionalization, the substrates were cut to the required size for the synthesis and then cleaned with ethanol followed by gentle drying under the nitrogen stream. Afterwards, the precleaned substrates were put into UV-ozone cleaner for 30 minutes in order to have -OH groups on the surface and remove the organic impurities from the surface. After this step, the substrates were put immediately into the metal solution and used for SURMOF synthesis.

3.2.3 Quartz substrates

The quartz substrates were functionalized also by using UV-ozone cleaner as described in functionalization of silicon substrate. First of all, quartz substrates were sonicated for 10 min. in acetone and ethanol, respectively. Then, they were rinsed with ethanol and gentle dried under the nitrogen flow. Afterwards, they were put into the UV-ozone cleaner for 30 min. for the functionalization. The substrates were used immediately after the functionalization.

3.2.4 Interdigitated electrodes

The interdigitated electrodes were rinsed with ethanol and then gentle dried under the nitrogen flow, followed by the functionalization of the surface by UV-ozone cleaner for 30 min. The electrodes were used immediately after the functionalization for SURMOF synthesis.

3.3 Instrumental Information of the Used Techniques

3.3.1 X-ray diffraction

X-ray diffraction was carried out using a D8-Advance Bruker AXS diffractometer with Cu Kα radiation ($\lambda = 1.5418$ Å) in $\theta-\theta$ geometry with position sensitive LYNXEYE-detector and variable

divergence slit. In this thesis, the samples were scanned generally from 5° to 20° with a step size of 0.02°and a scan speed of 1 s. Bruker EVA software was used for background corrections.

3.3.2 Infrared reflection absorption spectroscopy

Infrared reflection absorption spectroscopy (IRRAS) was performed using a Bruker VERTEX 80 purged with dried air in order to prevent the water bands. The IRRAS accessory (A518) has a fixed angle of incidence of 80°. The data were collected on a narrow-band liquid-nitrogen-cooled mercury cadmium telluride detector. Perdeuterated hexadecanethiol-SAMs on Au/Ti/Si were used for reference measurements. The sample measurements were stopped when water bands were not observable anymore. Bruker OPUS software was used for background corrections.

3.3.3 Raman spectroscopy

Raman analysis was carried out using a Senterra Raman microscope (Bruker Optics, Ettlingen, Germany) equipped with a 532 nm laser operated at 2mW output power as excitation source. For focusing the laser to the sample surface as well as collecting the backscattered light and Olympus MPLAN 50×NA 0.75 objective was used. The measurement time for each measurement spot was 90 s with three coadditions (3×30 s).

3.3.4 UV-vis spectroscopy

The ultraviolet–vis spectra were recorded by means of a Cary5000 spectrometer with an UMA unit from Agilent in order to check the SURMOFs in this PhD study.

3.3.5 ToF-SIMS

ToF-SIMS was performed on a TOF.SIMS[5] instrument (ION-TOF GmbH, Münster, Germany).

For the ToF-SIMS analysis shown in chapter 4.1.4.1, the spectrometer is equipped with a Bi cluster primary ion source and a reflectron type time-of-flight analyzer. UHV base pressure was $< 4 \times 10^{-8}$ mbar. For high mass resolution the Bi source was operated in "high current bunched" mode providing short Bi_3^+ primary ion pulses at 25 keV energy, a lateral resolution of approx. 4 µm, a target current of 0.35 pA. The short pulse length of 1.1 ns allowed for high mass resolution. No charge compensation was required. Spectra were calibrated on the omnipresent C^-, C_2^-, C_3^-, or on the C^+, CH^+, CH_2^+, and CH_3^+ peaks. Based on these datasets the chemical assignments for characteristic fragments were determined.

For depth profiling, a dual beam analysis was performed in a fully interlaced mode: The primary ion source was sawtooth scanned on an area of 500×500 µm^2 (128×128 data points) and a argon cluster sputter gun (operated with Ar_{1500}^+ ions, 10 keV, scanned over a concentric field of 750×750 µm^2, target current 3 nA) was applied to erode the samples. The sputter ion dose density was >1000 times higher than the Bi ion dose density. The sputter ion fluence was used as a measure for the erosion depth. To avoid signal differences due to different primary ion target currents in both measurements the sulfur signals were point by point normalized on total secondary ion counts.

For the ToF-SIMS analysis shown in chapter 4.2.6, base pressure was 7×10^{-9} mbar. Bi_3^+, 25 keV, 0.27 pA at 125 µs cycle time, were used as primary ions; Ar_{1200}^+, 0.25 keV, 0.7nA, as sputter ions. In order to remove trace amounts of physisorbed MP and to differentiate from thicker layers of polyMP, dynamic SIMS spectra were recorded in non-interlaced mode. Therefore, a 700×100 µm^2 crater was eroded (3 scans followed by 1s pause), and a concentric field of view of 500×500 µm^2 was analyzed (3 frames) until a total sputter time of 600 s was reached.

3.3.6 MALDI-ToF/MS

MALDI-ToF/MS experiments were performed using a 4800 MALDI-ToF/ToF mass spectrometer (AppliedBiosystems/MDS SCIEX, Foster City, CA) equipped with a Nd:YAG pulsed laser (355nm wavelength with <500ps pulses and 200Hz repetition rate). The 4000 Series Explorer (V3.5.3) and DataExplorer (V 4.9) software were used for the analysis. Data acquisition was performed in the reflector positive ion mode. Each mass spectrum obtained was an average of 1000 laser shots over the entire spot.

Prior to the MALDI-ToF/MS analysis, the SURMOF thin films (dimension of the substrate $\sim 1 \times 1$cm^2) were dissolved by immersing in a solution of 50 µL of acetic acid mixed with 0.2 mL ethanol, retaining the polymer chains. For the preparation of the mixture solution for the MALDI-ToF/MS analysis, 0.5 µL of the resulting liquid was mixed with 0.5 µL of matrix solution containing of 10 mg of DCTB in 1 mL THF. Then, 0.5 µL of the resulting solution was spotted onto the MALDI target and air-dried.

3.3.7 SEM and EDX

The scanning electron microscopy (SEM) analysis, as will be presented in Chapter 4.2.6, was performed using TESCAN Vega 3 with tungsten filament electron source. Images were taken using a working distance of 6-14 mm, with 8-10 kV emission voltage. For the energy dispersive x-ray spectroscopy (EDXS) and mapping (EDXM) a Bruker XFlash Detector 610M was used, always with 10 kV emission voltage. To prevent artifacts caused by electrical charging of the SURMOFs, the samples were sputtered with a Bal-Tec MCS 010 coating system using an Au-Pd target.

3.3.8 AFM

The atomic force microscopy (AFM) micrographs shown in Chapter 4.2.6 were recorded at room temperature using a Bruker Dimension Icon Atomic Force Microscope in alternating current mode (AC mode) in air using MikroMasch NSC15 probes, scan rate of 0.6Hz and 400 scan lines. A minimal number of modifications is performed in the raw data.

3.3.9 Electrical conductivity measurements

The electrical conductivity as will be presented in Chapter 4.1.4.1 was measured by using electrochemical impedance spectroscopy (EIS). The electrical conductivity of the pristine, loaded and oligomerized SURMOFs was measured using an impedance analyzer IM3570 (Hioki) R, L, C measuring device operated at room temperature in the frequency range of 4 Hz–8 MHz, using soft spring contacts with a spring constant of 1 N/m. The measurements were carried out at room temperature in an inert gas atmosphere.

The electrical conductivity of the samples as will be shown in chapter 4.2.6 was carried out by 2-probe current-voltage measurements using a Keithley 2635B Source Meter. The sample was grown on interdigitated gold electrodes on glass substrates from Metrohm. The gap width between the electrodes mounted to 5 µm, with a total gap length of 3.38 m. Electrical characterization was performed in pure nitrogen atmosphere at room temperature (298 K). Prior the experiment, the sample was equilibrated in the nitrogen atmosphere for more than one hour, for the desorption of all volatile guest molecules from the pores of SURMOFs. A pristine HKUST-1 sample was measured as a reference for a comparison with the polymer-filled HKUST-1 sample.

3.3.10 Quartz crystal microbalance

Quartz crystal microbalance (QCM) experiments, which will be presented in Chapter 4.2.6, were performed by using Q-Sense E4 Auto4 device. Firstly, SURMOFs were synthesized on gold coated QCM sensors by hand-spray applying 40 cycles according to the type of SURMOFs (for more details, see Chapter 4.2.2). Afterwards, the samples were put in QCM cell and were activated in pure argon flow at 40℃ over night following cool down to 25℃ in order to initiate the loading experiment. After the baseline was achieved, N_2 was bubbled in monomer (methyl propiolate) solution in order to observe adsorption of methyl propiolate in SURMOF. Reaching to the equilibrium was waited and then pure N_2 was flowed into the QCM cell for desorption of methyl propiolate until again equilibrium was reached. The temperature was adjusted to 40℃ in order to completely desorption of methyl propiolate from the SURMOF. During the QCM absorption-desorption experiments, flow rates of Ar and N_2 was sept up to 100 mL/min by using a mass flow controller.

4. RESULTS

4.1 Tth and EDOT Polymerization in SURMOF-2 Structures

4.1.1 Background

As mentioned in Chapter 1.3, MOF-templated polymerization reactions have drawn considerable attention in last decades, because its various advantages over conventional polymerization reactions such as morphology control, branching control during polymerization and homogenous mixing of immiscible polymers.[71, 72, 128, 129] MOF morphologies and their pore dimensions have a great effect in polymerization process.[130, 131] The literature review shows that a series of previous works have emphasized polymerization reactions inside the bulk MOF powder particles.[69, 132, 133] Since the polymers formed in MOF powder shows broad size distribution, controlling the polymer length within MOF powders is challenging. Therefore, SURMOFs are becoming increasingly important in order to obtain Polymer: MOF composites. Using SURMOFs instead of MOF powders for polymerization reactions has several benefits as follows: (1) easiness of characterization of polymer films formed within SURMOF thin films by microscopic or spectroscopic techniques, (2) the direct use of polymer films in different applications because of the possibility of the SURMOF growth on different kind of substrates (e.g. transparent or conductive surfaces).[36, 49, 58, 59]

In this part of the study, three different SURMOF-2 films prepared by LBL deposition technique, Zn(bdc) (**1**), Cu(bdc) (**1a**) and Cu(bpdc) (**2**), have been selected as a host structure to perform polymerization reactions within SURMOF-2, which were grown on functionalized SiO_2 and Au substrates. This study has focused on oxidative reactions of Tth and EDOT to obtain PTth and PEDOT, respectively. The oligomer formation inside the 1D channels of the SURMOF-2 was observed as a result. Additionally, PEDOT:SURMOF film with electrical conductivity was achieved in order to potentially use of these films in optoelectronics. Figure 4.1 shows the schematic of loading of monomers inside the 1D channels of SURMOF-2, the formation of oligomers inside the nano-pores of SURMOF-2 and digestion of SURMOF-2 with acetic acid to determine the chain length distribution of oligomers.[79]
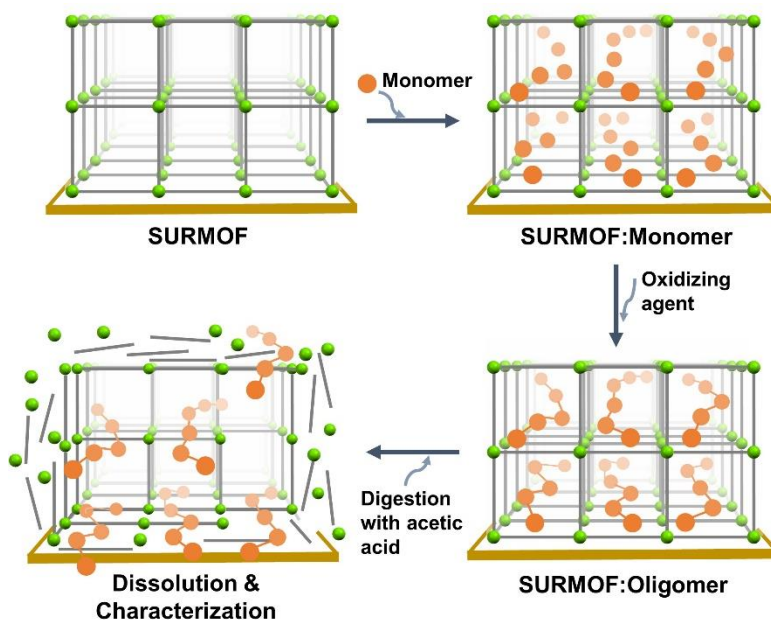
Figure 4.1 : Schematic showing the loading of monomers, the formation of oligomers inside the nano-pores of SURMOF-2 and digestion of SURMOF-2 to determine the chain length distribution of oligomers.

4.1.2 SURMOF-2 preparation

The SURMOF-2 thin films of **1**, **1a** and **2** were grown on functionalized Au, Si and quartz using the spray method as described in detail in chapter 1.2.3.1.

Prior the synthesis of **1**, the gold substrates were functionalized by SAMs deposited from MHDA solution, for detailed information see chapter 3.2.1. In case of Si and quartz substrates, the surfaces were functionalized by UV-treatment for 30 minutes, see chapter 3.2.2 and 3.2.3. The functionalized substrates were mounted on a sample holder and subsequently sprayed with a 1 mM ethanolic solution of $Zn(CH_3COO)_2 \cdot 2H_2O$ and 0.2 mM ethanolic solution of bdc at ambient temperature.

1a was prepared following the same methodology as described for **1**. Instead of $Zn(CH_3COO)_2 \cdot 2H_2O$, a $Cu(CH_3COO)_2 \cdot H_2O$ salt was used as a metal precursor. The precursor metal and linker concentrations were the same as in case of SURMOF-2 thin film of **1**.

In case of **2**, 1 mM ethanolic solution of $Cu(CO_2CH_3)_2 \cdot H_2O$ as the metal solution and 0.2 mM ethanolic solution of bpdc as the linker solution were used for spraying.

20 spray cycles were executed for all SURMOFs unless indicated otherwise.

4.1.3 Monomer loading and polymerization in SURMOF-2

Before the loading of Tth into the nanochannels of **1**, SURMOF was activated under vacuum at 80 ℃ for 6 h in order to completely remove solvent molecules from SURMOF. After the activation, the structure of SURMOF in terms of crystallinity was checked with XRD. Then, 100 μL of an ethanolic solution of Tth (6 mM) was drop casted on the activated SURMOF-2 and left undisturbed for approx. 1 h in a glass vial at room temperature following rinsing the substrate with ethanol. The drop casting and the rinsing step was repeated 4 times. The Tth loaded sample was placed in a chamber of I_2 for 6 h. Next, the sample was heated under the vacuum at 80 ℃ for 5-6 h for the polymerization reaction. Similar methodology was carried out for **1a**.

Prior to loading of EDOT into the nanochannels of **2**, SURMOF was activated under vacuum at 80 ℃ for 6 h. EDOT was drop casted on the activated SURMOF-2 and left undisturbed for 5 h in a glass vial at room temperature. Then, it was washed once with ethanol and left to dry at room temperature. For the polymerization reaction, **2** was immersed in an ethanolic solution of 1 M of $FeCl_3$ for 1 h followed by washing with ethanol.

As a hint in the result section, monomer loaded samples will be indicated as **Monomer:1, 1a** or **2**, whereas the oligomerized samples as **Polymer:1, 1a** or **2** regarding to the used corresponding monomer, polymer and SURMOF-2 structure.

4.1.4 Results and discussion

As mentioned above, SURMOFs were selected from SURMOF-2 isoreticular series as host structures in this part of the study.[134] By proper choice of linker with different lengths, the pore size of SURMOF-2 can be adjusted. These SURMOFs consist of 1D channels, which are parallel to substrate. Figure 4.2 represents the structure of **1** and **2**, in which the channels are in (010) direction, whereas SURMOF-2 grows in (001) direction perpendicular to the substrate. Ditopic carboxylate linker and paddle-wheel type SBUs are connected and form lamellar stacking 2D square grid-like structures, which results in formation of the channels.[134] The only difference between the structure of **1** and **2** is the length of the organic linkers and the type of used metal ions in the synthesis. However, these structures show P4 symmetry.[134]

In the following sub-sections, the results obtained by oligomerization of Tth in **1** and **1a**, and oligomerization of EDOT in **2**, respectively, will be shown.
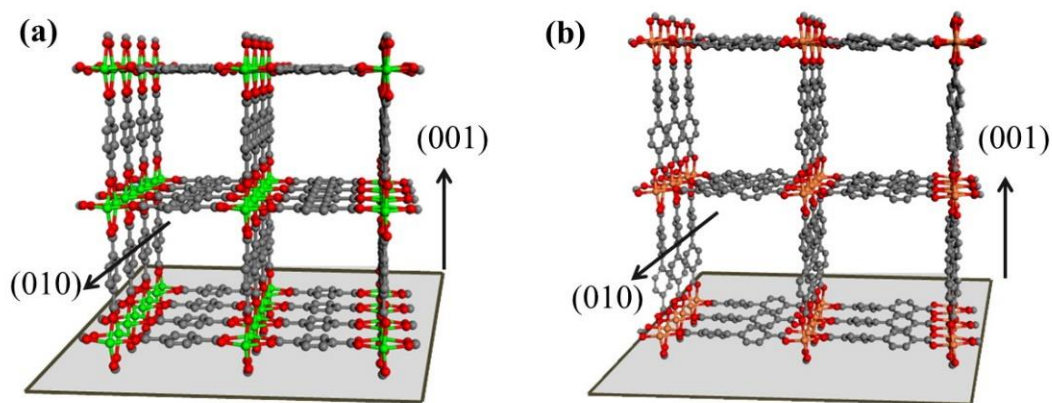
*Figure 4.2 : The structures of (a) **1** and (b) **2**.*

4.1.4.1 Oligomerization of Tth in SURMOF-2

As mentioned before in Chapter 4.1.3, Tth is oxidatively oligomerized in the pores of **1** and **1a** by means of exposure to the oxidizing agent I_2 vapor and subsequently heating to 80 ℃ for 6 h, which results in starting the oxidative reaction. Figure 4.3 shows the polymerization reaction of Tth in the presence of oxidizing agent.
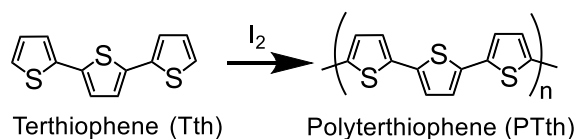

Terthiophene (Tth)   Polyterthiophene (PTth)

Figure 4.3 : Schematic of Tth polymerization reaction in presence of oxidizing agent I_2.

Firstly, out-of-plane XRD has been carried out in order to check crystallinity for pristine (**1**), monomer loaded (**Tth:1**) and polymerized SURMOFs (**PTth:1**). The XRD patterns shown in Figure 4.4 indicates the successful growth of SURMOF with two reflexes, (001) and (002), respectively. Compared to the simulated XRD pattern, observation of only these two reflexes reveals perfect crystalline orientation of **1** perpendicular to the substrate. Although the crystallinity remained unchanged after oligomerization, it is interesting to note that a new diffraction peak at 2θ ~ 8.3° for **Tth:1** existed, which is next to the (001) diffraction peak at 8.1°. The appearance of the new peak in SURMOF-2 structure after loading of large organic molecules has been published before for **1**, which indicates that a slight distortion, in means of small tilting of the planes, happens when guest molecules are loaded into the MOF structure.[64] Furthermore, control experiments were carried out for the empty pristine **1** in presence of I_2 vapor in order to check the stability of SURMOF. According to XRD analysis, it was observed that Zn- (or Cu-) paddlewheel-based frameworks are stable in presence of oxidizing agents.
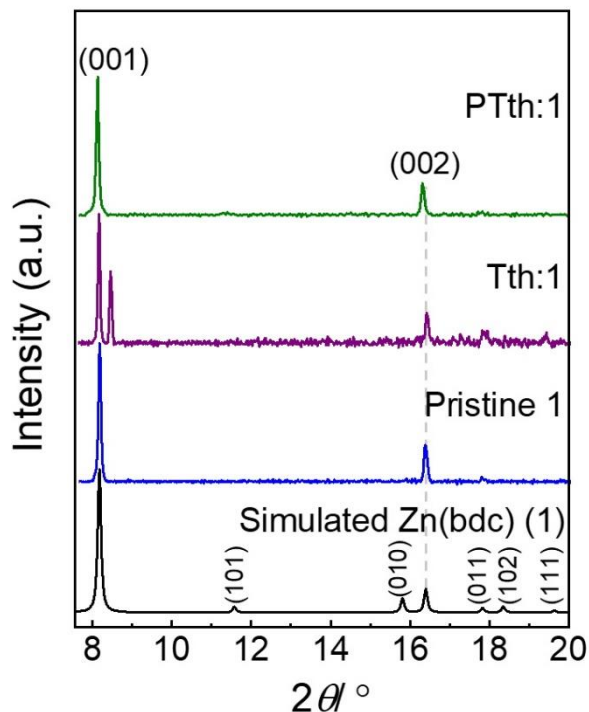
36

*Figure 4.4 : Simulated XRD pattern of **1** (black), out-of-plane XRD patterns of pristine **1** (blue), after Tth loading (**Tth:1**, purple), and after oligomerization (**PTth:1**, green).*

Spectroscopic techniques play an important role to prove whether monomer loaded and oligomerized inside the SURMOFs. Firstly, the characterization of chemical structure of pristine sample **1**, bulk Tth and **Tth:1** was performed by IRRAS. The corresponding IRRAS spectra are shown in Figure 4.5a, which reveals that monomers were successfully impregnated in the pores of SURMOFs. A peak observed at 795 cm^{-1} for both bulk Tth and **Tth:1**, which is absent for pristine **1**, represents C–H out-of-plane vibration of the thiophene rings.[135]

In addition to IRRAS, the sample before and after oligomerization was checked by Raman spectroscopy to observe the changes in the chemical structure. As seen in Raman spectra shown in Figure 4.5b, the peak at 1453 cm^{-1} for **PTth:1**, which is absent in pristine **1**, indicates the stretching vibrations of the –C=C– units in the polythiophene backbone.[136]
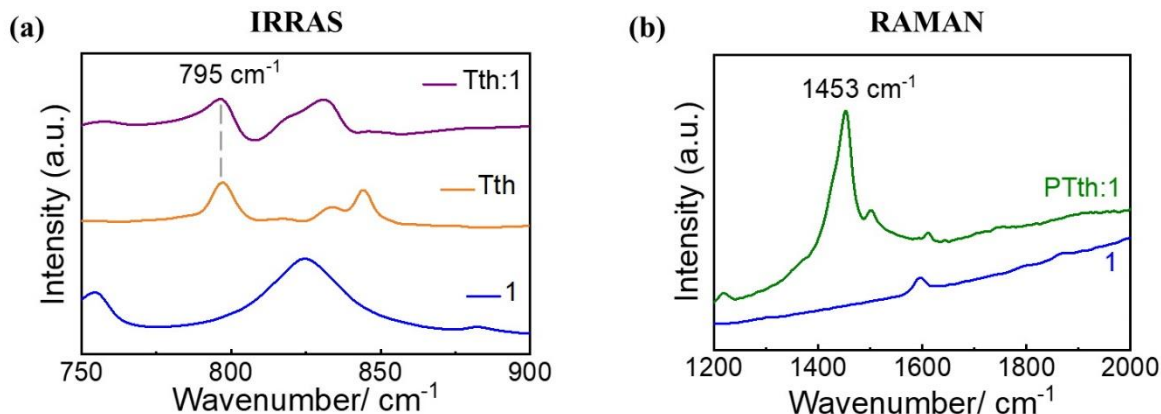
*Figure 4.5 : (a) IRRAS of pristine 1 (blue), bulk Tth (orange) and **Tth:1** (purple) showing C–H out-of-plane vibration of thiophene rings at 795 cm^{-1}, (b) Raman spectra of pristine 1 (blue) and **PTth:1** (green) showing the presence of C=C bond stretching band at 1453 cm^{-1}.*

MALDI-ToF/MS experiments were carried out in order to determine chain length distribution of the oligomers formed in SURMOF. Figure 4.6a shows the MALDI-ToF spectrum of **PTth:1** dissolved in acetic acid/ethanol solution, whereas the mass spectrum of bulk Tth oligomers in solution is shown in Figure 4.6b, where the specific peaks for terthiopene oligomers were marked. The expected m/z value of one Tth monomer unit is equal to 247.98. The experimentally observed difference in mass spectrum between the oligomers, however, is ~ 246.0 correspond to the mass of one monomer unit reduced by the mass of H_2 because of the oligomerization reaction. Short chains of PTth oligomers were observed with a maximum of n=4, where the oligomer chains in solution were observed with a length up to n=12. The mass spectra of the isotope patterns of PTth formed in **PTth:1** is shown in Appendix A (Figure 6.1).
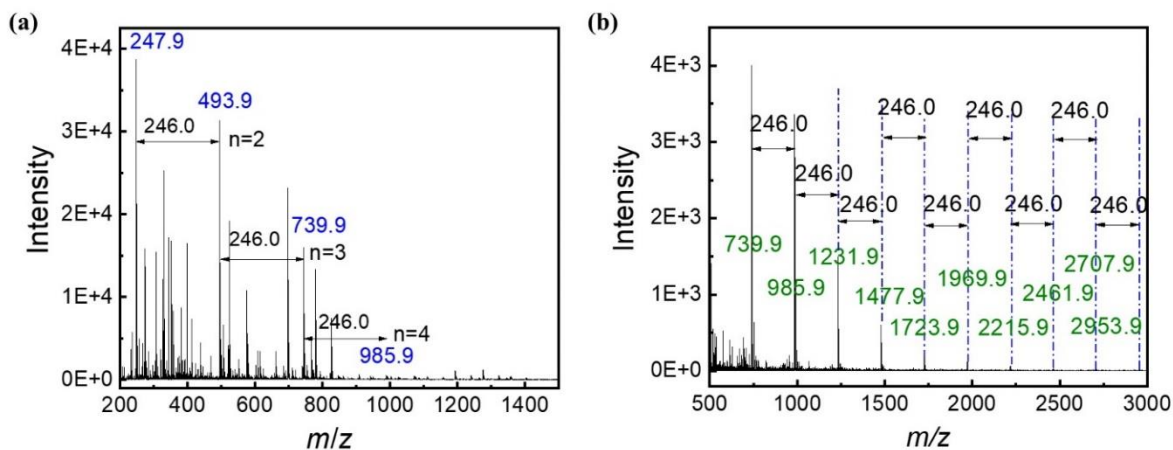

*Figure 4.6 : MALDI-ToF spectrum of (a) PTth formed in **PTth:1** and (b) PTth in solution.*

The main problem for the detection of oligomers/polymers inside the SURMOFs was the low concentration of the oligomers/polymers after the digestion of SURMOFs in acetic acid/ethanol solution. The detection of oligomers/polymers was not successful in the ESI/MS because of getting lower intensity for the oligomers/polymers at the end of the analysis. It can be considered that the ionization of the SURMOF can be easier compared to the oligomers/polymers, which resulted in the detection of SURMOFs, not the oligomers/polymers. However, digestion of SURMOFs by using of acetic acid/ethanol solution made possible to detect oligomers/polymers in MALDI-ToF/MS successfully in this study. After the optimization of this digestion method, the same procedure was always applied to detect the oligomers/polymers, which were formed in SURMOFs.

The reason to obtain short oligomer chains can be explained by restricted diffusion efficiency of Tth inside the SURMOF with 1D channels. In a previous study, it is emphasized that the molecular uptake rate is reduced in case of destroying the surface structure of SURMOF, which causes surface barrier formation.[137]

From MALDI-ToF/MS data, we can conclude that PTth oligomer chain formed in SURMOF has a length of ~ 4 nm, because the longitudinal axis of Tth is ~ 1 nm in length. If the interlayer distance of 0.56 nm for SURMOF-2 is taken into consideration[134], it can be stated that ~ 7 layers of 2D sheets in **1** include one PTth chain.

Table 4.1 shows the comparison of theoretical and experimental m/z values for PTth:1 obtained from MALDI-ToF spectrum, in which there is no significant difference between the theoretical and experimental values.

*Table 4.1 : Experimental and theoretical m/z values for **PTth:1** taken from mass spectrum.*

Label	m/z (exp)	m/z (theo)	Δm/z	Structure
n=1	247.9163	247.9783	0.062	$C_{12}H_8S_3$
n=2	493.9185	493.9414	0.0229	$C_{24}H_{14}S_6$
n=3	739.8802	739.9046	0.0244	$C_{36}H_{20}S_9$
n=4	985.8501	985.8678	0.0177	$C_{48}H_{26}S_{12}$

Besides the mass spectrum analysis, ToF-SIMS was used for depth profiling of the **Tth:1** and **PTth:1** samples in order to check the distribution of the terthiophene oligomers inside the nano-

pores of the SURMOF. As seen in Figure 4.7, **Tth:1** and **PTth:1** have the similar depth profile for sulfur atoms coming from thiophene units. This analysis confirms that the oligomerization occurred inside the pores of SURMOF, because the distributions of sulfur atoms did not change after monomer loading and oligomerization. Sulfur atoms were not only deposited on the surface of the SURMOF, rather they distributed throughout the SURMOF film.
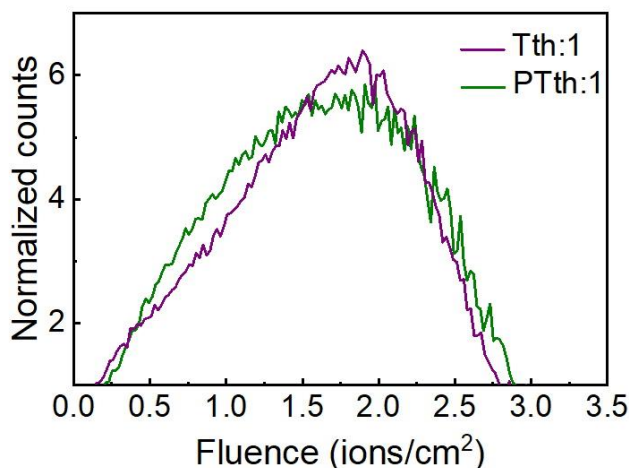

*Figure 4.7 : ToF-SIMS depth profiling of **Tth:1** (purple) and **PTth:1** (green) for sulfur atoms (Intensities point by point normalized on total counts).*

Terthiophene oligomerization was also performed in Cu(bdc) (**1a**) for a comparison with Zn(bdc). The only difference between these two isostructural SURMOF-2 are the metal ions used in the synthesis. Figure 4.8 displays the XRD patterns with two reflexes (001) and (002) of pristine **1**, **Tth:1a** and **PTth:1a**, which reveal the successful growth of SURMOF. In contrast to Tth oligomerization in **1**, a new peak at 9.3° was observed after the oligomerization next to the (001) diffraction peak at $2\theta \sim 8.1°$. The existence of the new peak in **PTth:1a** can be explained again by small distortion of the plane in SURMOF structure as discussed above in case of **1**.[64] Furthermore, a change in the relative intensity of the peak (001) after the oligomerization resulting the change of the form factor was observed, which also confirms that the oligomerization of monomers occurred inside the pores of SURMOF.
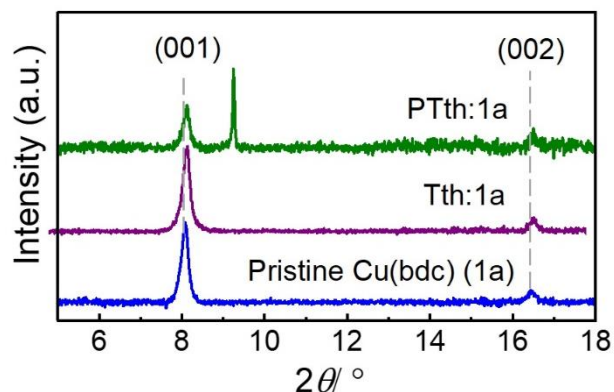
*Figure 4.8 : Out-of-plane XRD patterns of pristine **1a** (blue), after Tth loading (**Tth:1a**, purple), and after oligomerization (**PTth:1a**, green).*

MALDI-ToF/MS experiments carried out similarly as mentioned above to examine the chain length of the oligomers formed in **PTth:1a**. Figure 4.9 shows the MALDI-ToF spectrum of **PTth:1a** dissolved in acetic acid/ethanol solution. The analysis reveals that the maximum chain length observed in **PTth:1a** is n=4 comparable to **PTth:1**. The mass spectra of the isotope patterns of PTth formed in **PTth:1a** is shown in Appendix A (Figure 6.2). Limited diffusion efficiency of Tth inside the 1D channels of **1a** affected formation of longer polymer chains in **1a**.

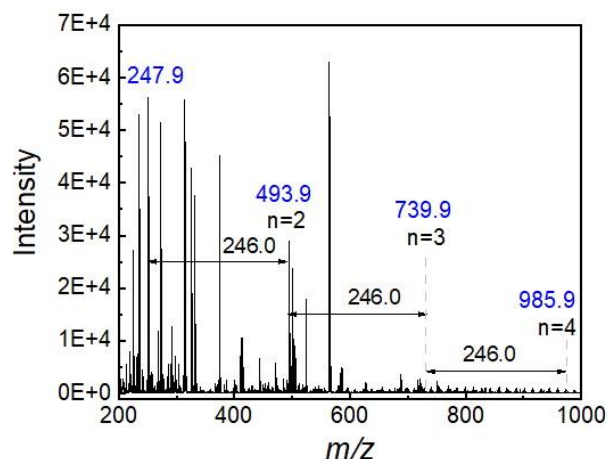*Figure 4.9 : MALDI-ToF spectrum of PTth formed in **PTth:1a**.*

4.1.4.2 Oligomerization of EDOT in SURMOF-2

Apart from Tth oligomerization in the host structure of **1** and **1a**, EDOT oligomerization was also investigated in the pores of Cu(bpdc) (**2**), which is isoreticular to **1** and **1a**. Since the linker molecule (bpdc) is larger than (bdc), **2** has larger channel window dimension.

41

EDOT is also oxidatively polymerized by drop casting in the pores of **2** in this case by using oxidizing agent FeCl$_3$. The polymerization reaction of EDOT in the presence of FeCl$_3$ is shown in Figure 4.10.

3,4-Ethylenedioxy
thiophene (EDOT)

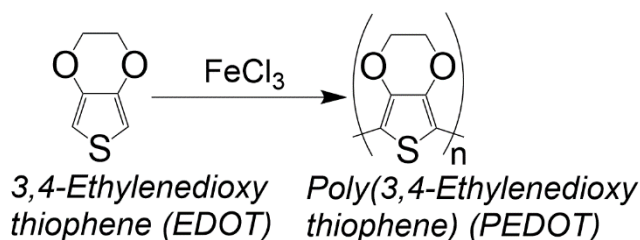Poly(3,4-Ethylenedioxy
thiophene) (PEDOT)

Figure 4.10 : Polymerization of EDOT in presence of oxidizing agent, FeCl$_3$.

First of all; the samples of **2**, **EDOT:2** and **PEDOT:2** were examined by using XRD to determine whether there are changes in the crystallinity of the structures after monomer loading and oligomerization (Figure 4.11). In contrast to the case of **1**, no change was observed in the out-of-plane XRD patterns after EDOT loading. Additionally, oligomerization did not affect the XRD patterns. This finding confirms that the structure and crystallinity stays unchanged after monomer loading and oligomerization. However, a change in relative intensities, especially in the (001) peak, can be observed in XRD patterns of **EDOT:2** and **PEDOT:2**, which points to the successful loading and oligomerization of EDOT inside the pores of **2**.
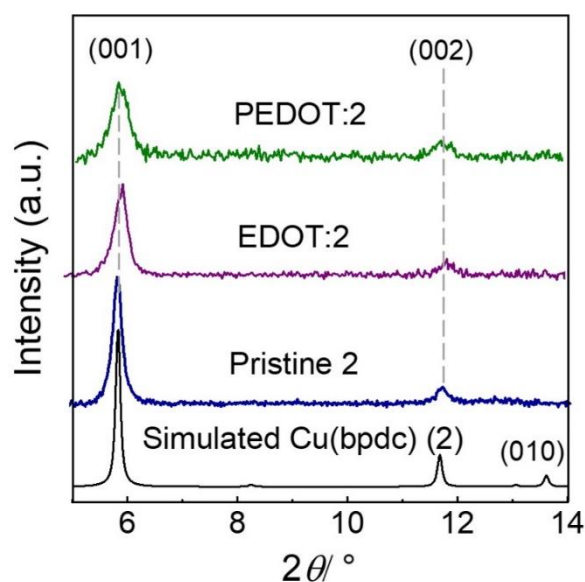

*Figure 4.11 : Simulated XRD pattern of **2** (black), out-of-plane XRD patterns of pristine **2** (blue), after EDOT loading (**EDOT:2**, purple), and after oligomerization (**PEDOT:2**, green).*

Besides XRD analysis, the pristine **2** and **PEDOT:2** were checked by UV-Vis and Raman spectroscopy in order to observe the changes after oligomerization. In order to check the change after oligomerization for **2** by UV-Vis, **2** was grown on quartz substrate. As can be seen from Figure 4.12a, a broad absorption in the visible light region for **PEDOT:2** was observed in the spectrum, which attributes to absorption of PEDOT in oxidized state.[138]
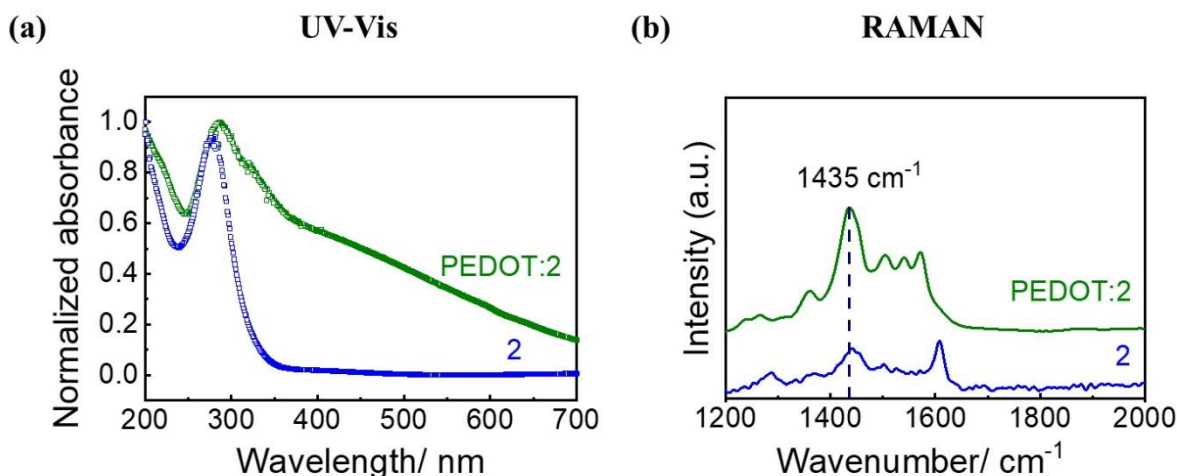

*Figure 4.12 : (a) UV-Vis spectra of **2** (blue) and **PEDOT:2** (green), (b) Raman spectra of **2** (blue) and **PEDOT:2** (green) presenting the C=C stretching band of PEDOT at 1435 cm^{-1}.*

Furthermore, Figure 4.12b represents the Raman spectra in order to characterize the chemical structure changes before and after oligomerization of EDOT. It can be clearly seen from the spectra that there is a band at 1453 cm^{-1} for **PEDOT:2**, which assigns the C=C stretching band. Raman spectra together with UV-Vis spectra indicates that the oligomerization of EDOT is successful in the pores of SURMOF.

For determination of oligomers' chain length, MALDI-ToF/MS was used to get the mass spectrum of PEDOT formed in **PEDOT:2** after dissolving in acetic acid/ethanol mixture. The MALDI-ToF spectrum, shown in Figure 4.13a, indicates that the PEDOT oligomer chains were obtained up to n=9, whereas the length of the bulk oligomer chains formed in solution were n=14 as displayed in Figure 4.13b. The isotopic patterns of mass spectra for **PEDOT:2** are shown in Appendix A (Figure 6.3). Since the m/z value of EDOT is equal to 142.17, the difference between the oligomers in mass spectrum was observed as ~ 140.0, which has 1 H_2 molecule less because of the oligomerization reaction. It can be concluded that the difference of obtained chain length in solution and in **2** is smaller compared to the chain length of PTh in solution and in **1**.
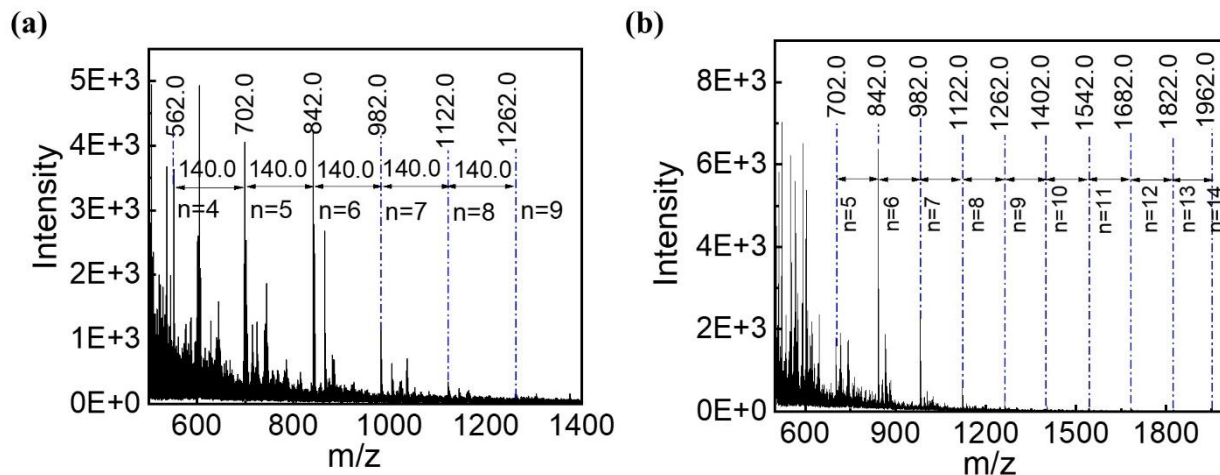
*Figure 4.13 : MALDI-ToF spectrum of (a) PEDOT formed in **PEDOT:2** and (b) PEDOT in solution.*

Table 4.2 presents the slight difference between the theoretical and experimental m/z values obtained from MALDI-ToF spectrum for **PEDOT:2**.

*Table 4.2 : Experimental and theoretical m/z values for **PEDOT:2** taken from mass spectrum.*

Label	m/z (exp)	m/z (theo)	Δm/z	Structure
n=4	561.9539	561.9879	0.034	$C_{24}H_{18}O_8S_4$
n=5	701.9791	701.9811	0.002	$C_{30}H_{22}O_{10}S_5$
n=6	841.9791	841.9743	0.0048	$C_{36}H_{26}O_{12}S_6$
n=7	981.9680	981.9675	0.0005	$C_{42}H_{30}O_{14}S_7$
n=8	1121.9665	1121.9607	0.0058	$C_{48}H_{34}O_{16}S_8$
n=9	1261.9737	1261.9539	0.0198	$C_{54}H_{38}O_{18}S_9$

An important implication of these results mentioned above is the electrical conductivity of PEDOT:SURMOF composites. If the literature is reviewed, it can be clearly seen that the electroconductivity of PEDOT:PSS (polystyrene sulfonate) mixture has been widely investigated, because they have great stability and high electrical conductivity (1-10 S×cm^{-1}).[139] Normally, PEDOT is known as an intractable polymer because of its poor solubility. Hence, PEDOT should be mixed with PSS in order to increase the solubility. PEDOT:PSS is used widely as a conductive

thin polymer film.[139-141] Since the main limitation of PEDOT-coatings on solid substrates is the low solubility of PEDOT, **PEDOT:2** thin films synthesized on SiO_2 showed a clearly advantage over the other PEDOT-coatings, because no dilution is required with another polymer. The electrical conductivity measurements were performed by using electrochemical impedance spectroscopy (EIS) as described in Chapter 3.3.9. The conductivity after oligomerization of EDOT was measured for three different thicknesses of **2** (corresponding to 30, 50 and 80 cycles), which was grown on SiO_2 substrates. Figure 4.14a presents conductivity of silicon wafer, **PEDOT:2** with 30 cycles and **PEDOT:2** with 50 cycles. Boron doped silicon wafer with <100> surface orientation and native grown oxide were selected as reference system to compare the conductivity. These measurements reveal that the conductivity is higher in **PEDOT:2** with 50 growth cycles compared to **PEDOT:2** with 30 growth cycles. The explanation of these findings can be that the surface is not fully covered when SURMOF is grown with 30 cycles, which results in lower conductivity. In order to see the effect of the SURMOF thicknesses on the conductivity, the conductivity was measured also for **PEDOT:2** with 80 growth cycles. As seen in Figure 4.14b, the conductivity is the same for both **PEDOT:2** with 50 and 80 growth cycles, which indicates that the homogenous thin film was obtained after 50 growth cycles. The conductivity of **PEDOT:2** for both cases was measured as 1.6×10^{-7} S×cm^{-1}. The conductivity was also measured for EDOT loaded SURMOF and lower conductivity was observed as expected. If the literature is reviewed, it is seen that PEDOT:MOF powder (MIL-101) composite has the conductivity of 1.1×10^{-3} S×cm^{-1} in the 3D pores of MIL-101, which is higher compared to our findings. The main limitation of having lower conductivity in **PEDOT:2** can be explained by getting shorter oligomer chains in **2** and having lower intermolecular interactions in the 1D channels of **2**. Nevertheless, it has been reported before that the conductivity of PEDOT:MOF powder with 1D channels is equal to 2.3×10^{-8} S×cm^{-1}, which is in good agreement with our findings.[142]
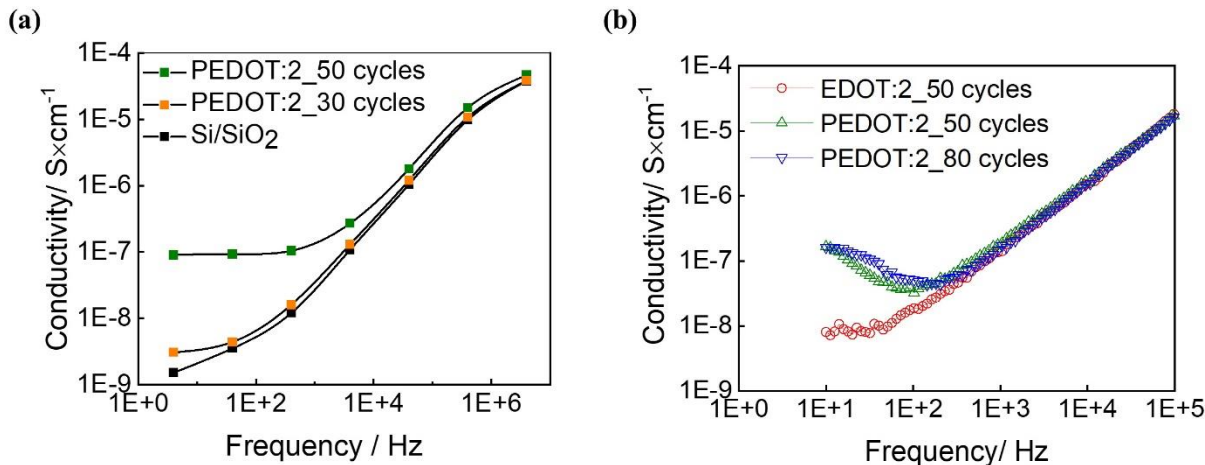
*Figure 4.14 : Conductivity as a function of frequency (a) for silicon wafer (black), **PEDOT:2** with 30 growth cycles (orange), **PEDOT:2** with 50 growth cycles (green); (b) for **EDOT:2** (red), **PEDOT:2** with 50 growth cycles (green) and **PEDOT:2** with 80 growth cycles (blue).*

4.1.5 Summary

In summary, oligomerization of Tth and EDOT monomers was successfully performed in the pores of host structures, which was selected from isoreticular SURMOF-2 series. As a first step, the monomers were loaded through drop casting into the activated SURMOF-2 structures following the oligomerization step, which is done by the help of corresponding oxidizing agents (I_2, $FeCl_3$). The results confirm that the crystallinity of the SURMOF-2 as a host structure did not be altered by oligomerization reaction. Spectroscopic techniques, which were used to check the chemical structure of the surface before and after oligomerization, showed that the oligomers are inside the pores of SURMOFs. By using MALDI-ToF/MS, the maximum chain length was observed as n=4 for Tth, whereas it was n=9 for EDOT. The reason to obtain rather short chain length after oligomerization can be explained by lower diffusion efficiency of monomers inside the SURMOF-2. Nevertheless, the conductivity results of PEDOT:MOF films propose that PTth:MOF or PEDOT:MOF thin films can be used in optoelectronic applications in the future because of their feasible growth on different kind of substrates and easiness of processing.

4.2 Methyl Propiolate Polymerization in Different Type of SURMOFs

4.2.1 Background

MOFs plays an important role in order to use them as a template for polymerization reactions of various monomers, as mentioned before.[35, 143, 144] Since the pores and pore-channels of MOFs provide a confined space for polymerization reactions, polymerization of different kind of monomers in MOFs has been reported up to the present, e.g. aromatic acetylene[132], substituted acetylenes[81], methacrylate[133], vinyl monomers[70, 71], acrylonitrile[145] and perylene.[146] Although the polymerization in MOF thin films has some benefits for characterization over the bulk MOF powders, due to their uniformity in flat solid substrates, not many study has been reported for SURMOF thin films used as a template for polymerization reactions.[79, 85, 86]

In this chapter, polymerization of methyl propiolate (**MP**) catalyzed by Palladium (Pd) was investigated in 3 different type of SURMOFs, Cu(bpdc) (**2**), $Cu_2(bdc)_2(dabco)$ (**3**) and HKUST-1 (**4**). Since **2**, **3** and **4** have different geometries of pore channels, 1D, quasi-1D and 3D, respectively, a comprehensive study was performed in order to recognize advantages and drawbacks of MP polymerization in different types of SURMOF pore systems. As a result, the maximum chain length and molecular weight distribution was controlled successfully in different dimensions of the pore systems. Furthermore, a depot-like release of **MP** was found for **2** by performing QCM loading and unloading experiments, which resulted in polymer formation as a top layer on the SURMOF. On the other hand, faster release of excess **MP** was explored in 3D channels of **4,** where no top layer polymer formation was observed. Therefore, using **4** as a host structure for polymerization of **MP** was optimized and electrical conductivity was measured after **MP** polymerization inside the channels of **4**, which resulted in an increase of conductivity compared to the pristine **4**.

4.2.2 SURMOF preparation

Thin films of **2**, **3** and **4** were used as a template for methyl propiolate polymerization.

The thin films of **2** and **4** were grown using layer-by-layer deposition via the spray coating method, for more details see 1.2.3.1. Gold substrates were functionalized by MHDA, whereas Si substrates were functionalized by UV-treatment prior to synthesis as described in chapter 3.2.1 and 3.2.2. The functionalized substrates were mounted on the sample holder and subsequently sprayed. For the synthesis of **2**, 1 mM ethanolic solution of $Cu(CH_3COO)_2 \cdot H_2O$ as a metal solution and 0.2 mM

ethanolic solution of bpdc as a linker solution were used. The thin films of **4** were also prepared with the same methodology. The metal solution was the same as Cu(bpdc), whereas the linker solution was 0.2 mM of btc in ethanol.

The thin films of **3** were grown on Au and Si substrates using the layer-by-layer deposition via a pump system (for more details, see chapter 1.2.3.2). Prior to SURMOF synthesis, the gold substrates were functionalized by SAM deposited from a MUD solution as described in detail in chapter 3.2.1. For the synthesis, 1 mM of $Cu(CO_2CH_3)_2 \cdot H_2O$ as a metal solution and the mixture of 0.1 mM of bdc and dabco as a linker solution were used in order to grow of **3**. After the functionalization of the substrates, they placed inside the sample holder of a pump system. During the synthesis, the substrates were immersed in the ethanolic copper acetate solution for 10 minutes, whereas the immersion time of the linker solution was 20 minutes. 40 deposition cycles were applied at 60℃.

4.2.3 Monomer loading and polymerization in SURMOF

Prior to loading of **MP**, the SURMOFs were activated under vacuum at 80℃ for 6 hours. For the loading step, 400 μL of **MP** was mixed with a trace amount of palladium chloride ($PdCl_2$) catalyst. This solution was drop casted on the activated SURMOF and left undisturbed for 2 hours in a glass vial at room temperature. To remove the residual monomer the samples were washed with chloroform before the polymerization. Afterwards, the MP loaded SURMOF (**MP:2, MP:3, MP:4**) was placed into the oven at 90℃ for 5 hours to obtain poly(methyl propiolate) (**PolyMP**) in the SURMOF (**PolyMP:2, PolyMP:3, PolyMP:4**). Finally, the samples were washed with chloroform to remove unreacted monomer and excess polymer from the surface for further characterization.

Bulk polymerization of **MP** was carried out in slight difference to literature.[147] Bulk polymerization was done in order to compare the chain length of the **PolyMP** in bulk with the polymer synthesized in the pores of the SURMOFs. Bulk **PolyMP** was prepared by mixing 400 μL of **MP** with a trace amount of $PdCl_2$. The mixture was put into an oven at 90℃ for 5 hours.

4.2.4 Modelling the SURMOF structures by loading MP and Pd

The software package BIOVIA Material studio 2018 was used to create appropriate models of the MP and Pd loaded **2**, **3** and **4** MOF structures. Each unit cell was filled with one of MP and one Pd molecule. The structure models were then used in order to simulate XRD patterns for comparison

with the experimental data. No structure optimization using e. g. force fields was carried out for these model structures.

4.2.5 Simulation of methyl propiolate

Force field simulations of the coiling behavior of polyMP polymers with n=20 were carried out using CgenFF version 4.0 with the CHARMM36 force field applied.[148-151] Coiling simulation initiated with a steepest descent minimization, then followed by a 100 ps Canonical ensemble (NVT) simulation using a V-rescale thermostat, then followed by 10 ns NVT simulation using Nose-Hoover thermostat. All simulations were carried out in GROMACS 2019.2 with periodic boundary conditions applied.

4.2.6 Results and discussion

As mentioned above, three different SURMOFs; **2**, **3** and **4** were selected as a host structure for **MP** polymerization. The polymerization reaction of **MP** catalyzed by $PdCl_2$ to yield **polyMP** is shown in Figure 4.15. MP – which is the methyl ester of propiolic acid in this case – belongs to the class of a substituted acetylene monomers.[152]
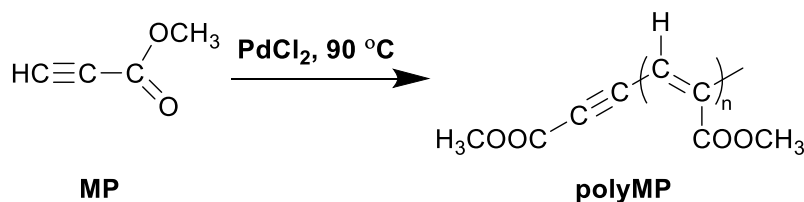

*Figure 4.15 : Polymerization reaction of **MP** catalyzed by $PdCl_2$ to yield **polyMP**.*

Figure 4.16 presents the structure of **2**, **3** and **4**, which are synthesized by LBL procedure in order to obtain uniform SURMOFs with well-defined orientation on the substrate. Firstly, SURMOF system **2**, which was used also as a template for EDOT polymerization, was selected to investigate the **MP** polymerization inside its 1D pore channels that are parallel to the substrate (Figure 4.16a). **2** shows a sheet like structure with an interlayer distance between the planes of 5.6 Å.[134]
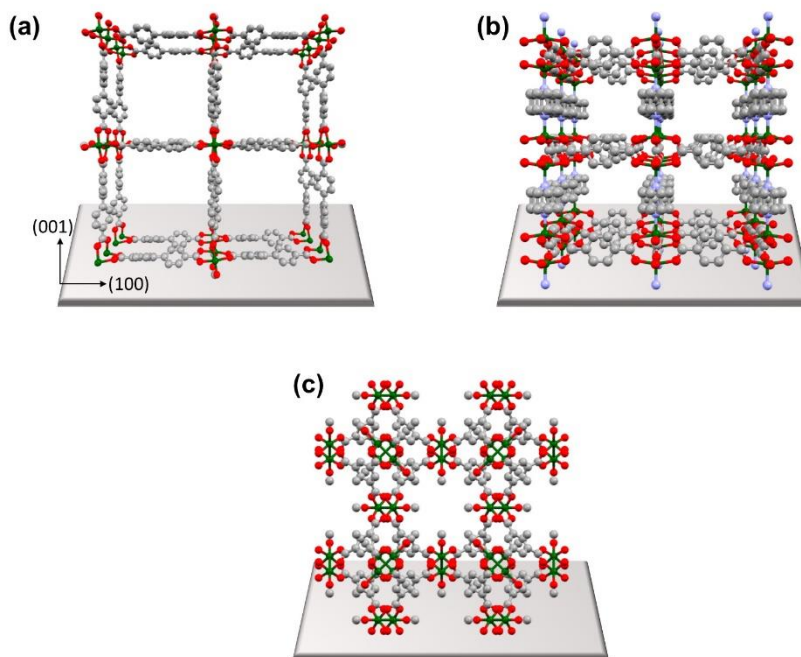
Figure 4.16 : The structure of (a) **2**, *(b)* **3** *and (c)* **4**. *Color scheme: C (gray), O (red), N (purple), Cu (green).*

As shown in Figure 4.16b, **3** has large square shaped channels perpendicular to the substrate with a size of $7.5\text{Å} \times 7.5\text{Å}$[153], whereas the cubic pore windows which are oriented parallel to the support have slightly small openings with the size of 4.8 Å × 3.2 Å.[154] **3** can be thought as quasi-1D framework for the polymerization reaction because of its small openings, which can hinder the diffusion of **MP** with a kinetic diameter of 6.2 Å.

SURMOF system **4** was chosen for this comparative study, because it has been widely studied and is a well-known system. **4** has 3D pore system, which exhibits pore windows with a diameter of 9 Å and 6 Å[155], rather than the other systems **2** and **3** (Figure 4.16c). Also, it consists of 3 different cavities with a pore diameter of 14 Å, 11 Å and 5 Å.[156] Although the smallest cavity in **4** is not big enough for the diffusion of **MP** because its size, there is enough space in **4** to have continuous **polyMP** after **MP** loading and polymerization step.

The common points of these three investigated systems in this study are the connection of the linker molecules via Cu-paddle wheel type SBUs.

By using of basis molecular dynamics simulations, the sizes of polymer coils formed from **PolyMP** were estimated, which is presented in Figure 4.17. For the simulation, 20 monomer units were used

to obtain one polymer molecule. After the simulation of initial structure of **PolyMP** (Figure 4.17a), the formation of coils with an average radius of gyration equals 0.66 nm was observed expectedly (Figure 4.17b). The dimensions of the coils structure were found as 1.5 x 1.9 x 1.8 nm. Regarding to these simulations, it can be concluded that n=20 coils should fit into the pores of all three MOFs, **2**, **3** and **4**.
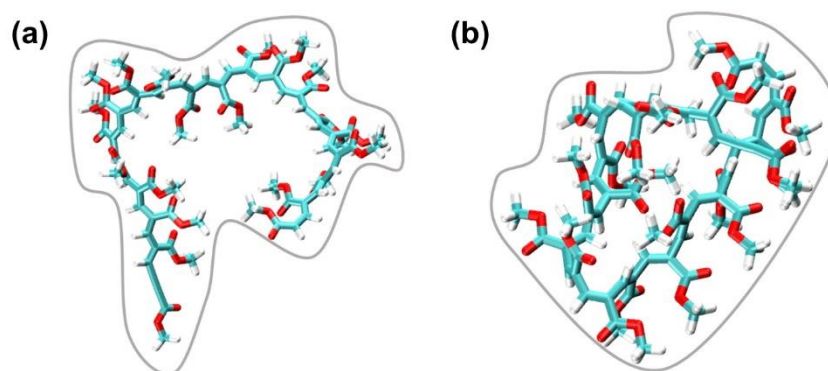
*Figure 4.17 : Molecular dynamics simulation of the (a) initial structure of **PolyMP** and (b) final coiled structure of **PolyMP**.*

First of all, out-of-plane XRD patterns were recorded by XRD in order to check the changes in the crystallinity of SURMOFs before and after **MP** loading and polymerization, as shown in Figure 4.18. It can be concluded from XRD patterns that **MP** loading into the SURMOFs has a weak effect on the intensity of reflexes. However, small changes in the intensity ratio due to changes in the form factors caused by the **MP** loading into the SURMOFs were observed especially in the system **3.** Modelling of the SURMOF structures were carried out to check the XRD patterns after the loading of one **MP** or Pd molecule in the pore of SURMOF, which was consistent with the experimental XRD patterns (see Appendix B, Figure 6.4). Especially, modelling of Pd loading in the pores of SURMOFs is in good agreement with the experimental XRD pattern after **MP** polymerization.

For the SURMOF system **2**, it was observed that (001) and (002) peaks disappeared after the polymerization, whereas a new peak (210) appeared (Figure 4.18a). Based on the modelling of the **MP** and Pd loading into **2**, the occurrence of the new peak (210) was also observable after loading of of Pd. Since Pd is used as a catalyst in the polymerization reaction, the simulated data is consistent with the experimental data.
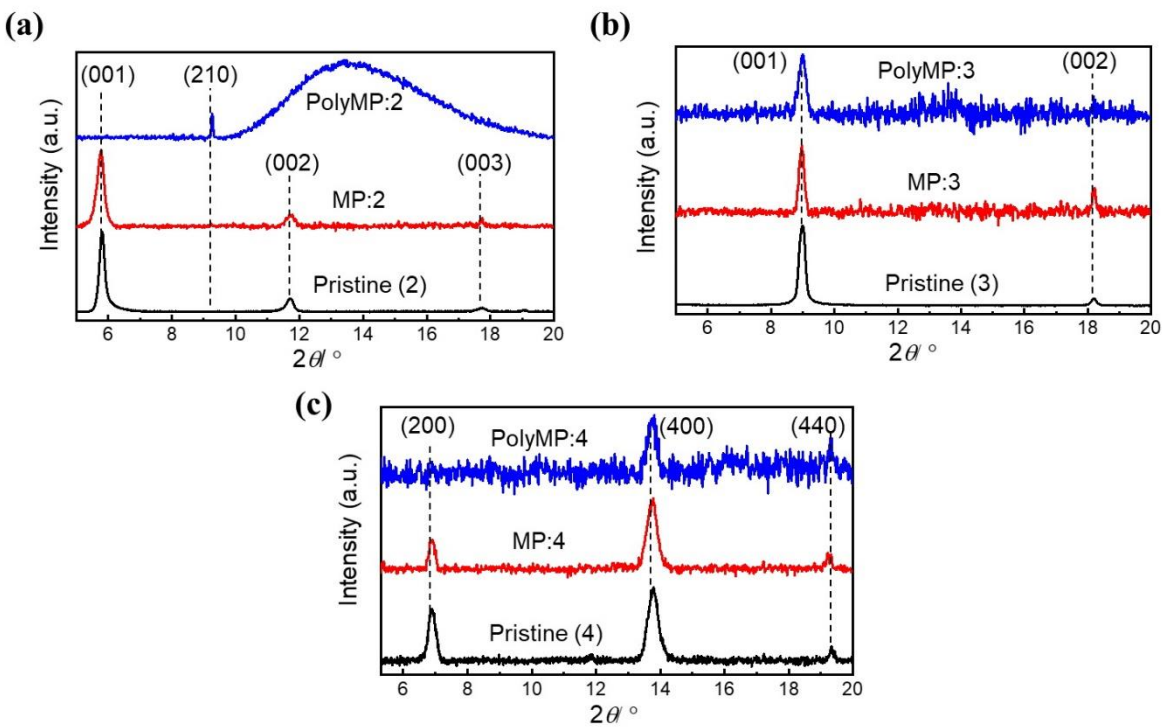
*Figure 4.18 : Out-of-plane XRD patterns of (a) **1**, (b) **2** and (c) **3** in pristine state (black), after MP loading (red) and after polymerization (blue) with normalized intensities.*

For the SURMOF system **3**, form factor changes were observed after **MP** loading and polymerization especially for the reflex of (002), which can be explained by strongly interaction with the lattice and introducing crystal strain after **MP** loading and polymerization (Figure 4.18b).

For the SURMOF system **4**, XRD patterns indicated that the (200) peak disappeared, whereas the (400) peak was still visible after **MP** polymerization. Moreover, a decrease in the intensity of the (200) peak and the changes in form factors were observed after **MP** loading (Figure 4.18c). When the modelling and the experimental data are compared, it was observed that the experimental XRD patterns were affected stronger by the loading and polymerization compared to the modelling data, but the change was still comparable.

All XRD patterns revealed that **MP** loading and polymerization affected the intensities of reflexes and form factors. But it is important to note that SURMOF structure remains still crystalline after **MP** loading and polymerization.

Besides the XRD analysis; SEM and EDX analysis played a crucial role in order to observe the morphologically and elemental changes in SURMOFs after the **MP** polymerization. Figure 4.19 shows the characterization results of the cross-sections for SURMOFs before and after **MP** polymerization performing SEM and energy dispersive X-ray mapping (EDXM) analysis.
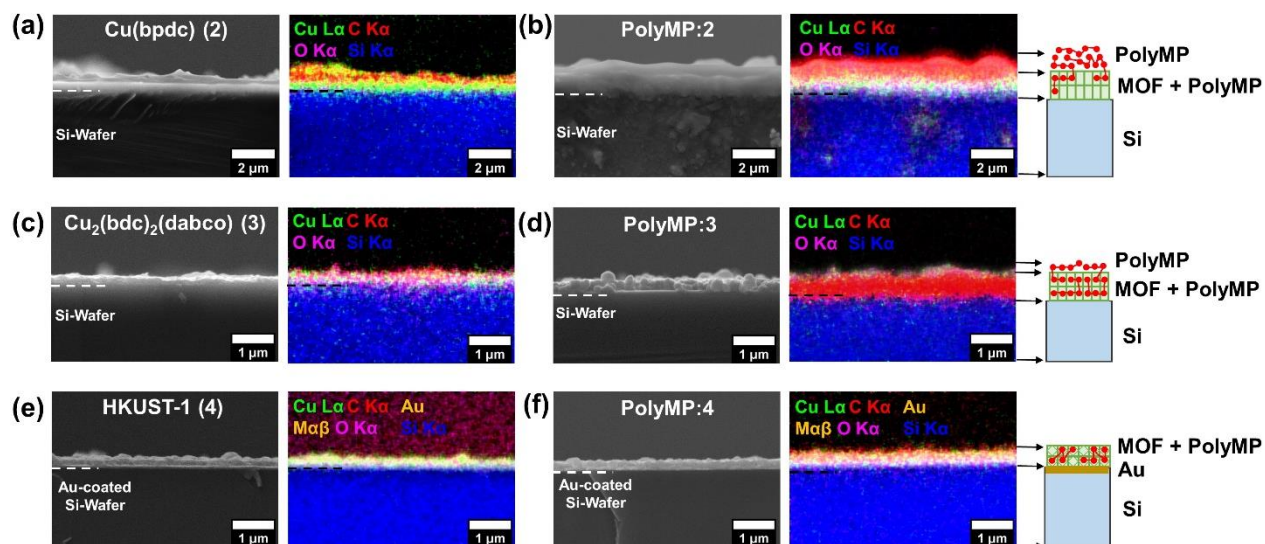

Figure 4.19 : SEM images and corresponding EDXM of (a) pristine **2**, *(b)* **PolyMP:2**, *(c) pristine* **3**, *(d)* **PolyMP:3**, *(e) pristine* **4** *and (f)* **PolyMP:4**. *The cartoons on the right side of (b), (d) and (f) visualize the observations of* **PolyMP** *formation.*

The SEM analysis indicated that the thickness of all pristine SURMOF layers are about 200-300 nm. Interestingly, various changes were visible after polymerization of **MP** in SURMOFs, particularly in the thickness of the samples and elemental analysis.

For the SURMOF system **2**, it can be clearly observed from SEM analysis together with EDXM that a thick layer of polymer covered the whole surface after **MP** polymerization (Figure 4.19a, b). Moreover, energy dispersive X-ray spectroscopy (EDXS) analysis of SURMOF thin films were performed for the elemental analysis before and after the polymerization (Appendix B, Figure 6.5). The increase in C-signal to Cu-signal ratio was observed after polymerization for **PolyMP:2**, which can be explained by a successful polymerization inside the pores of SURMOF and the formation of a thick polymer top layer (Appendix B, Figure 6.5a, b). Based on EDXM analysis, the distribution of carbon signals shows where the polymer was formed, which is as a thick top layer, as well as inside the **2** (Figure 4.19a, b).

For the SURMOF system **3**, a thinner polymer layer covering the surface was observed (Figure 4.19c, d). From SEM analysis, this system seems like less limited and works better than **2**. Based on the EDXM analysis, **PolyMP** and MOF were indistinguishable, which can be explained by the equally distribution of polymer inside the pore of **3**. Moreover, a slightly increase in the overall carbon signal and decrease in the copper signal was found for **PolyMP:3** compared to the pristine **3** in EDXS analysis, which can be attributed to a successful polymerization mainly inside the pores of **3** (Appendix B, Figure 6.6a, b).

For the SURMOF system **4**, SEM and EDXM analysis showed that not even a thin top layer was observable on the surface of **4**, which provide an evidence that polymerization occurred only inside the pores of **4** (Figure 4.19e, f). In Figure 4.19f, EDXM analysis revealed that the carbon signal has the same intensity as the copper signal, which also an indicator of successfully polymerization inside the pores of **4**. Furthermore, EDXS analysis also confirmed the polymerization inside the pores, because the carbon signal of **PolyMP:4** is more than two times higher than the pristine **4**, whereas the copper signal was almost the same (Appendix B, Figure 6.7a, b).

Since a thick polymer top layer was observed in the case of **2** after polymerization, polymerization of **MP** was tried in different thicknesses of **2** (30 & 40cycles) in order to see the effect of the SURMOF thickness over the thickness of formed polymer on the surface. It has been found by SEM together with EDXM analysis that the thickness of the polymer top layer on **2** has linear dependence with the thickness of the **2**. As shown in Figure 4.20, the polymer thickness for **PolyMP:2** grown with 40 cycles is bigger than in the case of **PolyMP:2** grown with 30 cycles, as expected. The difference in thickness between the pristine **2** and **polyMP:2** was 100 nm for 30 growth cycles, whereas it was 150 nm for 40 growth cycles.
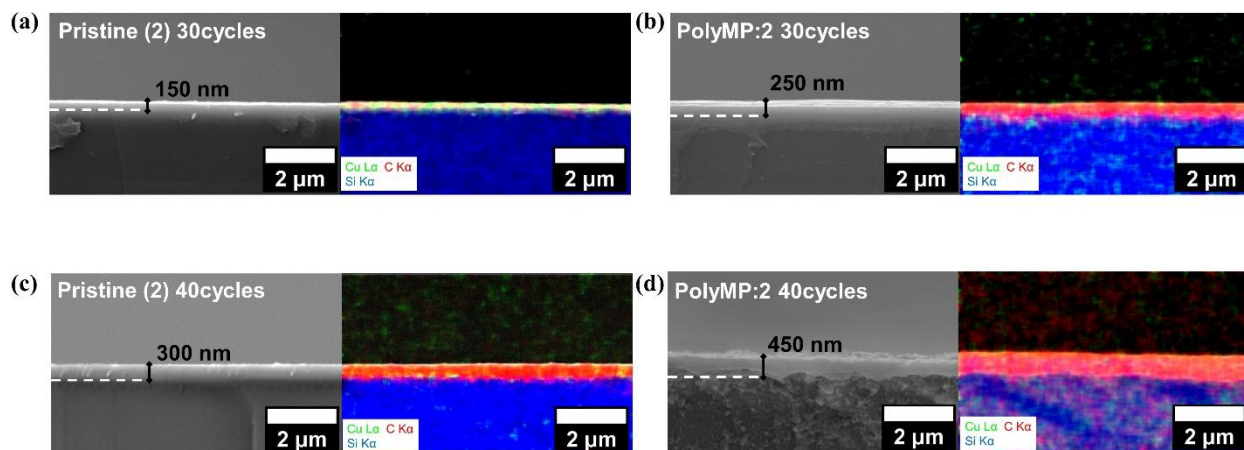
*Figure 4.20 : SEM and EDXM images of 30 growth cycles of (a) pristine **2** (b) **PolyMP:2**; 40 growth cycles of (c) pristine **2** and (d) **PolyMP:2**.*

The formation of thick polymer layer on **2** gave rise to thought the diffusion out of the monomer after loading, which resulted in polymer film formation on the SURMOF thin film. Since the pore channels of **2** are aligned parallel to the substrate, the diffusion of **MP** could be difficult and a polymer top layer can be formed on the surface. However, **4** has 3D pore system, which could make easier for the diffusion of **MP** into the pores, so no top layer formation was observed. Therefore, QCM experiments were performed for **MP** loading inside the **2** and **4** to find the answer of the formation of polymer top layer. The adsorption/desorption kinetics were checked of the thin films **2** and **4**.

Figure 4.21 presents the graph of the normalized mass change from adsorption and desorption of **MP** on **2** and **4** over time by using QCM. From these results, it is clear that **MP** showed a slow and steady release from the framework of **2** starting at t=20 min. It can be clearly seen that the desorption kinetics of **MP** from **4** much faster than from **2**. Hence, the desorption kinetics of MP from **2** is an indicator for a slow release of the monomers from the depot, which is consistent with SEM analysis, where a polymer top layer formation was observed. Regarding to the desorption kinetics of **4**, a quick release of monomer was found. But it doesn't mean that all monomers diffused out from **4**. From Figure 4.21, it can be concluded that most monomers were bound within open metal sites of HKUST-1 and only excess monomers which are loosely bound or unbound, were diffused out quickly. If the final normalized mass change per cm^2 was taken into consideration, it can be concluded that **4** contains more **MP** compared to **2** at the end of desorption

process. Further analyses like MALDI-ToF and ToF-SIMS were carried out in order to prove the polymerization of monomers, which took place inside of the SURMOFs.
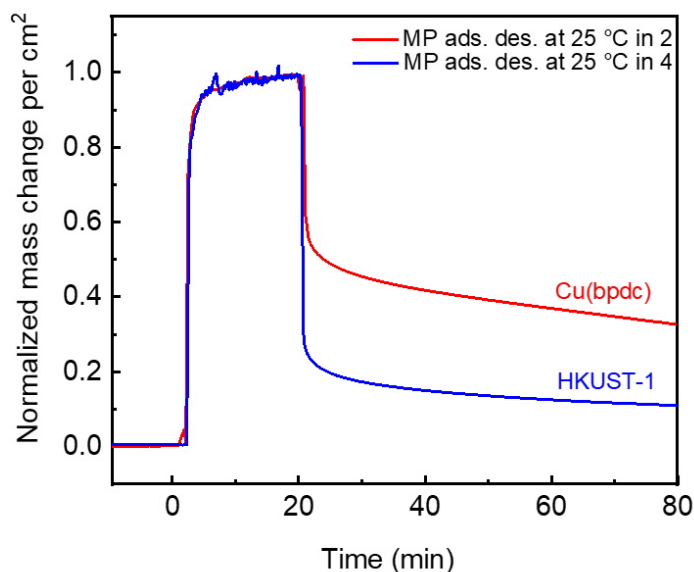

*Figure 4.21 : The normalized mass change from adsorption and desorption of **MP** on Cu(bpdc) (**2**) and HKUST-1 (**4**) measured by QCM at 25 ℃.*

The time constants of the desorption process of MP from **2** and **4** is shown in Table 4.3. The time constants showed that ~ 144 min was required to remove 80% of the monomer from **2**, whereas only ~ 2.6 min is needed in case of **4**. Because of this slow and long release of **MP** from the framework **2**, top layer can be formed on the surface. Since the release of **MP** was faster from the framework **4** like burst release, it is good agreement why no top layer was formed on the surface of **4**. Adsorption/desorption kinetics of the thin films of **2** and **4** are shown in detailed graphs in Appendix B (Figure 6.8). The desorption experiment was performed firstly at 25 ℃ following at 40 ℃ in order to remove all absorbents.

*Table 4.3 : Time constants of the desorption process of **MP** from the framework of **2** and **4** on QCM sensors.*

Time constant (min)	Cu(bpdc) (2)	HKUST-1 (4)
$T_{0.5}$	1.9	0.3
$T_{0.8}$	144.3	2.6

Figure 4.22 represents a schematic diagram, based on the QCM analysis, which shows the depot effect of MP diffusion from **2** and **4**. The results confirm, that **MP** diffused depot-like slowly from **2**, which causes a polymer top layer formation, whereas the diffusion from **4** was faster leading to no polymer top layer formation.
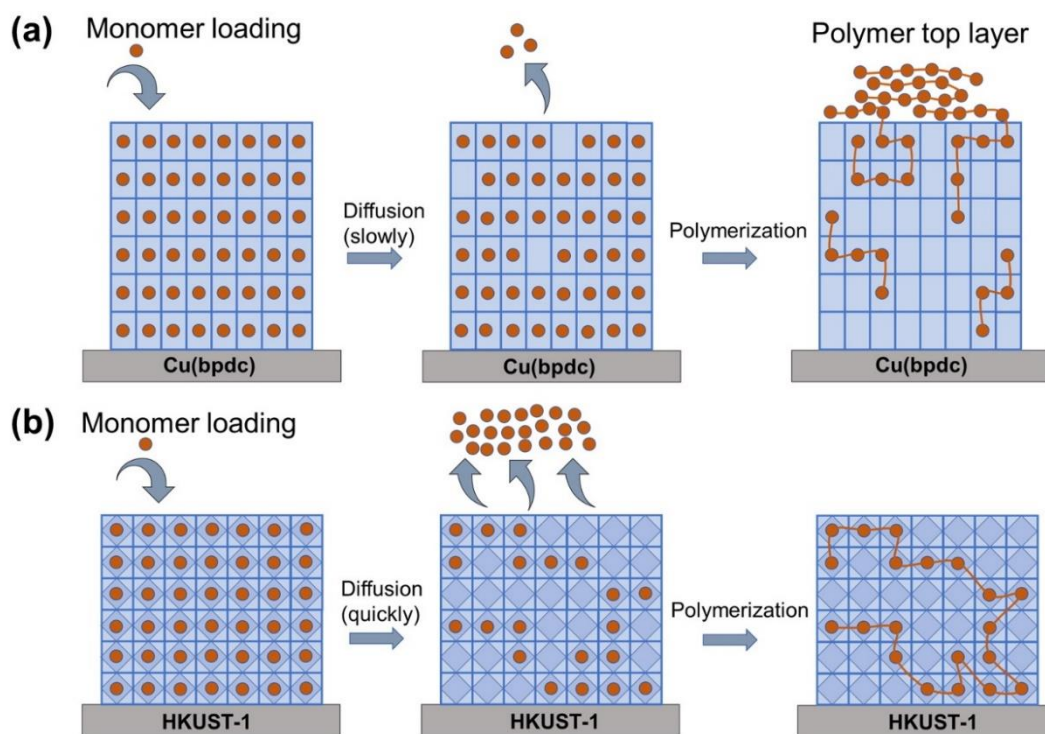

*Figure 4.22 : Schematic diagram showing the depot effect of (a) **MP** diffusion from **2** and (b) quick release from the framework of **4**, followed by polymerization.*

In addition to the above-mentioned analyzes, the polymer morphology was checked by AFM, which is shown in Figure 4.23 with two different magnifications. Bulk synthesized **PolyMP** dissolved in acetic acid/ethanol mixture was deposited on a flat silicon substrate, whereas **PolyMP** obtained from SURMOF system **4** was deposited on a flat silicon substrate, after the digestion of **PolyMP:4** in acetic acid/ethanol mixture. The images of AFM analysis indicated that the bulk polymer formed large, spherical and agglomerated particles (Figure 4.23a, b). However, the polymer formed in SURMOF exhibits a significantly different morphology than the bulk polymer (Figure 4.23c, d). The polymer particles became much smaller compared to the bulk polymer and they formed like a polymer film including very tiny and agglomerated particles. The reason to get tiny particles can be attributed to the concentration difference between bulk polymer and polymer from SURMOF.
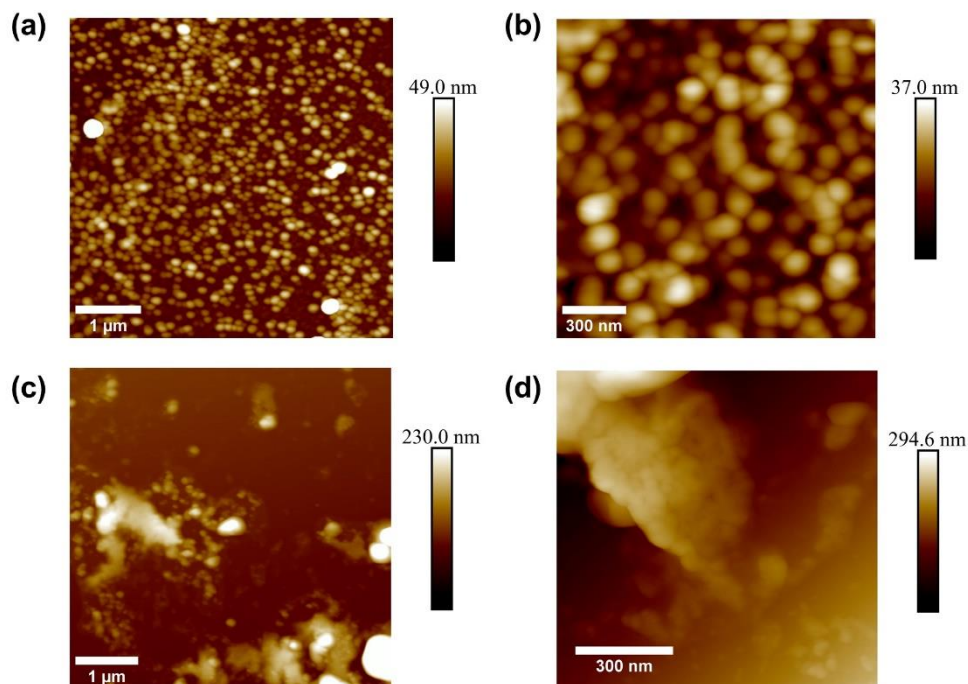
Figure 4.23 : AFM images of (a, b) bulk polymer (c, d) polymer from SURMOF deposited on the smooth surface.

MALDI-ToF/MS was used in order to determine the chain length and molecular weight distribution of the **PolyMP** formed in **2**, **3** and **4**. For this reason, dissolution of **PolyMP:2**, **PolyMP:3**, **PolyMP:4** was carried out by immersing the samples into the mixture of ethanol and acetic acid solution before the MALDI-ToF/MS analysis. Figure 4.24 represents the spectra of **PolyMP** formed in **2,3** and **4**. The size distribution of the polymer can be clearly observed in mass spectra with a difference of ~ 84, because the molecular mass of a monomeric unit **MP** is 84.07 g/mol. The masses shown in the spectra are sodium adduct masses, which was coming from the ionization of substrate. MALDI-ToF spectra can show sodium adducts for low molecular weight samples, because mostly sodium salts are added and dissolved in MALDI-ToF/MS in order to initiate the ionization process.[157, 158]

The chain length of **PolyMP** formed in **2** were observed with a maximum length up to n=22 (Figure 4.24a), in **3** with a length up to n=19 (Figure 4.24b), whereas in **4** with a length up to n=23 (Figure 4.24c). If each peak in the spectrum is examined in detail, the isotopic patterns of the peaks can also be seen (see Appendix B for n=8, Figure 6.9). Besides this analysis, the chain length determination was also done for the bulk polymer as a comparison of the chain lengths., which is formed by reaction in solution with a maximum chain length up to n=23 (Appendix B, Figure 6.10).
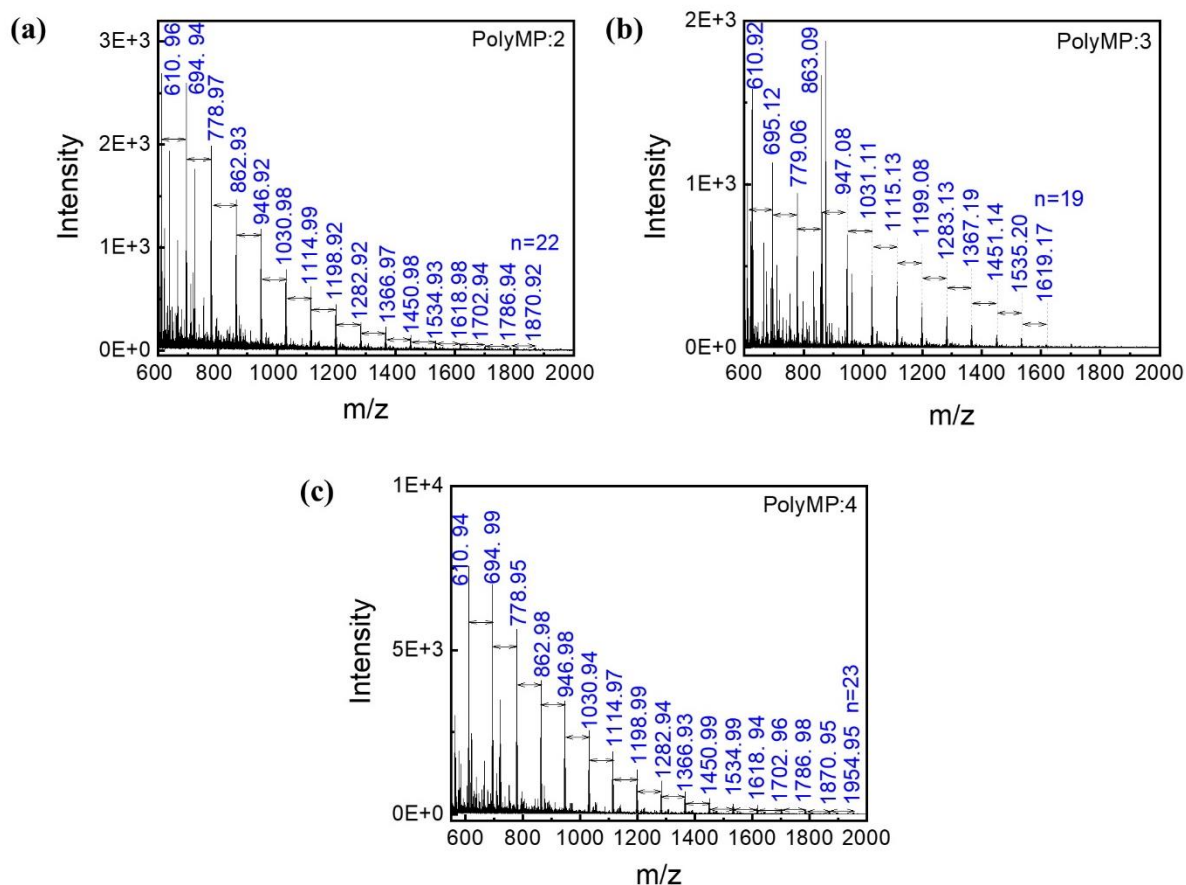
*Figure 4.24 : MALDI-ToF spectrum of (a) **PolyMP:2** (b) **PolyMP:3** and (c) **PolyMP:4** after dissolution in acetic acid/ethanol.*

For the SURMOF system **2**, it was shown in SEM together with QCM analysis that a polymer top layer was formed on the surface. Hence, it can be expected that the same molecular weight distribution for **PolyMP:2** can be achieved as in the bulk polymer. Interestingly, maximum chain length for **PolyMP:2** was observed with a length up to $n=22$, which points out the idea of confined polymerization in SURMOF.

For the SURMOF system **3**, the acquired maximum chain length was shorter compared to the other systems, which can be attributed a successful polymerization in the 1D channels of **3**.

For the SURMOF system **4**, getting the maximum chain length with a length up to $n=23$ as same as in bulk polymer was not expected, because no top layer formation was seen in **4** after polymerization.

If the all MALDI-ToF/MS spectra are taken into account, it can be concluded that SURMOFs with 1D channels restricts the diffusion of the monomers inside the SURMOFs, which is resulted in

formation of polymer with lower chain lengths. Using of SURMOFs with 3D pore system for the polymerization reaction achieve getting the similar molecular weight distribution as the bulk polymer.

For further characterization of polymerization inside the SURMOF, ToF-SIMS analysis was performed on all samples in order to see changes before and after polymerization. Figure 4.25 shows the depth integrated spectra of the all samples (**2**, **3** and **4**) with three different analyzed spots indicating the monomeric unit $C_4H_3O_2^-$ of **MP** after monomer loading and polymerization. Since the chemical formula of MP is $C_4H_4O_2$, $C_4H_3O_2^-$ is the deprotonated form of **MP** upon polymerization. The depth integrated spectra indicate that only rather small amounts of $C_4H_3O_2^-$ were found in **MP:2, MP:3** and **MP:4**. This is because of easily desorbing of the monomers from the lattice under UHV conditions in ToF-SIMS. Nevertheless, detection of some residual monomers in monomer loaded samples can be explained by not easily desorption of the sticky monomers from the SURMOF lattice. After the **MP** polymerization in all cases proves a successful polymerization of **MP** inside the SURMOFs.
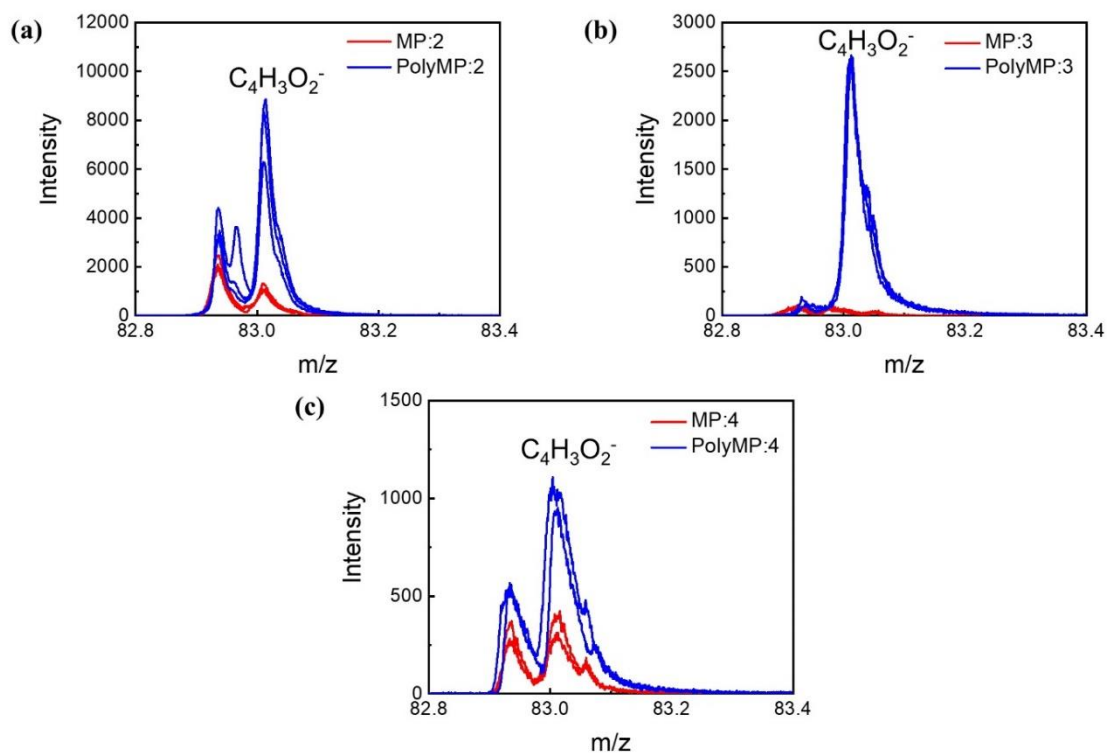

*Figure 4.25 : Depth integrated ToF-SIMS spectrum showing the main fragment of the **PolyMP** repeating unit of (a) **MP:2** (red) and **PolyMP:2** (blue) (b) **MP:3** (red) and **PolyMP:3** (blue) (c) **MP:4** (red) and **PolyMP:4** (blue).*

Furthermore, depth integrated images and depth profiles were recorded by ToF-SIMS. Depth integrated images for all cases reveals that there is a correlation between $^{63}Cu^-$ & $^{65}Cu^-$ and $C_4H_3O_2^-$ for the polymerized samples of **2**, **3** and **4** (see Appendix B, Figure 6.11-6.13). Also, depth profile analysis normalized on the Cu-signal, coming from the SURMOF indicates that there is a gradient starting at the top of each SURMOF surface with the highest monomer content which disappears gradually in the direction of the substrate (Si or Au) (see Appendix B, Figure 6.14). All ToF-SIMS analysis proves the **MP** polymerization takes place inside the pores in all SURMOFs, even if a polymer top layer is formed.

Since the goal of this study was to achieve the formation of the polymers completely inside the pores of SURMOFs, SURMOF system **4** was chosen for the conductivity measurements, because no polymer top layer formation was observed in **4**. Formation of a thick layer on the surface of SURMOF **2** and **3** was not convenient for the reliable electroconductive measurements. The lateral conductivity was measured for **4** and **PolyMP:4** by using interdigitated Au-electrodes. The investigation as shown in Figure 4.26 revealed a significant increase in conductivity of 6 orders of magnitude after **MP** polymerization compared to that of pristine **4**. The current is proportional to the voltage showing ohmic conduction behavior. The **PolyMP:4** exhibits a current of 3.6 µA at 3 V, whereas the pristine sample **4** shows a current of 3.3 pA. Referring to the sample thickness of ~ 200 nm, the data corresponds to a conductivity of 9 µS/m, which is about 6 orders of magnitude higher than the conductivity of the pristine **4**, where the conductivity was 8 pS/m. The conductivity of the pristine **4** is consistent with the other published values.[159, 160]
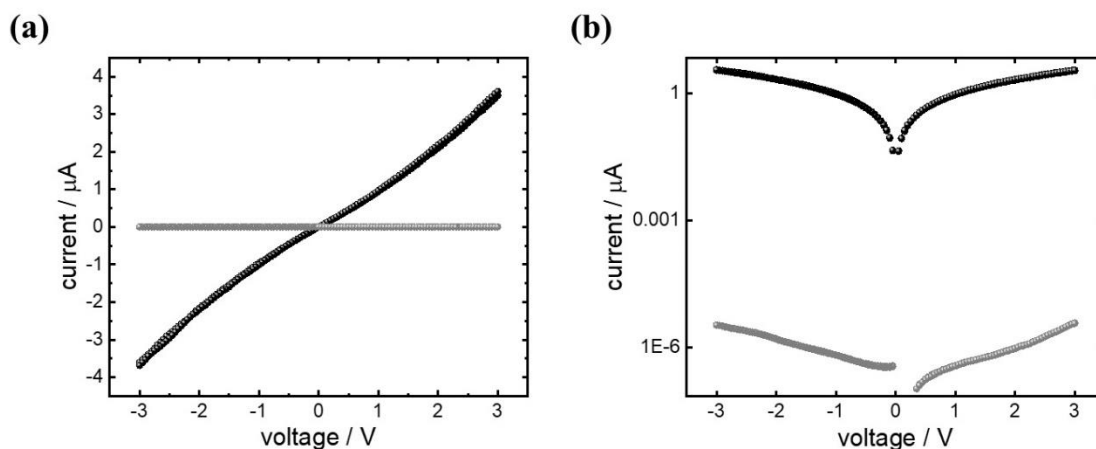

*Figure 4.26 : Conductivity of **PolyMP:4**. (a) The current-voltage curve of the **PolyMP:4** sample is shown in black, the current-voltage curve of **4** is shown as reference in grey. (b) The data on a log-scale.*

61

4.2.7 Summary

To sum up the results, Pd-catalyzed polymerization of methyl propiolate has been successfully carried out in the pores of Cu(bpdc), $Cu_2(bdc)_2(dabco)$ and HKUST-1. It has been shown that pore-volume and pore-channels affects the polymerization. Based on XRD analyses, it has been shown that monomer loading and polymerization have an effect on the intensities of the reflexes and form factors, but the SURMOF structures remained still crystalline. SEM analysis together with EDX analysis revealed a polymer top layer formation in Cu(bpdc) and $Cu_2(bdc)_2(dabco)$. However, no polymer top layer formation was observed in HKUST-1, which indicates a successfully polymerization inside the pores of HKUST-1. The maximum chain length determined by MALDI-ToF was n=22 for Cu(bpdc), n=19 for $Cu_2(bdc)_2(dabco)$, whereas n=23 for HKUST-1. The maximum chain length of the bulk polymer formed in solution was also n=23 as same as in HKUST-1 with the 3D pore systems. For the investigation of the polymer top layer formation, QCM experiments were performed, in which it has been found a quick desorption of methyl propiolate from HKUST-1, whereas a depot-like slow and steady desorption was observed from Cu(bpdc). These findings can prove the polymer top layer formation in Cu(bpdc) and $Cu_2(bdc)_2(dabco)$. AFM analysis was carried out in order to compare bulk polymer and polymer formed in HKUST-1. It indicates that large spherical particles were formed in bulk polymer synthesis, whereas fibers and tiny agglomerates were observed as polymer from the MOF pores. ToF-SIMS analyses showed that the polymerization was performed inside the pores of the all three SURMOFs in spite of the polymer top layer formation. Since HKUST-1 revealed as a best SURMOF system for polymerization reaction with its 3D pore systems, electrical conductivity was measured for HKUST-1 after polymerization. It has been found that, the electrical conductivity after polymerization was increased to 6 orders of magnitude compared to the pristine HKUST-1. An increase in electroconductivity plays an important role on the various electrical applications of SURMOFs, e.g. in sensors or microelectronics.

5. CONCLUSION AND OUTLOOK

This thesis demonstrates templated polymerization reactions in SURMOFs synthesized by LBL procedure on functionalized substrates for different kind applications. It has been shown that templated polymerization in SURMOFs is useful to (i) control the chain lengths of the polymers and (ii) for potential electrical applications.

The first part shows oxidative reaction of Tth and EDOT, polymerized in the pores of different SURMOF-2 structures, consisting of 1D channels. The resulting reaction yields oligomers instead of polymers as described in Chapter 4.1. Tth was loaded inside the pores of Zn(bdc) or Cu(bdc) and polymerized in the presence of I_2 as oxidizing agent, whereas EDOT was loaded in Cu(bpdc) and left to polymerize in the presence of Fe^{3+} as oxidizing agent. Based on the MALDI-ToF/MS analysis, the chain lengths for PTth oligomers were observed with a length up to n=4 and for PEDOT oligomers with a length up to n=9. The polymer chain length in SURMOFs is rather shorter compared the chain lengths of the bulk polymer formed in solution. Checking the SURMOF structures by XRD revealed no changes or effect on the crystallinity of the SURMOFs after oligomerization. In order to see how the oligomerization altered the chemical structure of SURMOFs and to prove the occurrence of oligomerization inside the pores of SURMOFs, analyses with UV-Vis, FTIR and Raman spectroscopy were performed before and after the oligomerization for the samples, showing successful oligomerization on the inside of the pores of the SURMOF structures. The poor solubility of PEDOT hinders electrical conductivity, because covering a surface only with PEDOT is not easy. PEDOT can be mixed with PSS to increase the stability and to use as a conductive thin polymer film. However, we could show in this study that PEDOT:SURMOF thin film composites are showing a good alternating current conductivity, making the system suitable candidates for optoelectronic applications.

In the second part of the thesis, a Pd-catalyzed polymerization of methyl propiolate was used in a case study of three different SURMOF structures, as described in Chapter 4.2: Cu(bpdc), $Cu_2(bdc)_2(dabco)$ and HKUST-1. The polymerization in these three different SURMOFs with the same Cu-paddle wheel unit, but different pore windows, channel dimensions and volumes revealed interesting results. Analyzing the polymer composites with MALDI-ToF/MS showed that the maximum chain length of PolyMP was n=22 for Cu(bpdc), n=19 for $Cu_2(bdc)_2(dabco)$ and n=23 for HKUST-1. Polymerization in case of HKUST-1 yielded a quite similar result to the bulk

polymer synthesized in solution. SEM and EDXM analyses were performed for the characterization of the structures before and after the MP polymerization. We find from EDXM and EDXS that polymer top layer formation on Cu(bpdc) and $Cu_2(bdc)_2(dabco)$ occurs, whereas it was not observed in case of HKUST-1. To find an explanation for the polymer top layer formation, QCM analysis was performed to see the desorption kinetics of MP from Cu(bpdc) and HKUST-1. While a depot-like slow release was observed from Cu(bpdc), a faster release from HKUST-1 is found. A slower desorption kinetic can be assumed to favor polymer top layer formation. Furthermore, ToF-SIMS analyses were carried out in order to prove that the polymerization occurred inside the pores. It was found that polymerization occurred inside the pores of three different SURMOFs despite of the polymer top layer formation in Cu(bpdc) and $Cu_2(bdc)_2(dabco)$. Since HKUST-1 did not show any polymer top layer formation, it was chosen for the electrical conductivity measurements. Comparing the pristine HKUST-1 with the MP polymerized HKUST-1, six orders of magnitude higher electrical conductivity have been achieved for the polymer composite. This again plays an important role for the potential usage of polymerized SURMOF thin films in different electrical applications, such as pseudocapacitors, sensors and actuators.

In both parts of the thesis, polymerization reactions were successfully carried out in different type of SURMOF structures. These studies showed that the pore channels can be a limiting factor the for the diffusion of the monomers. However, the monomer formation to conjugated oligomers or polymers in the pores of SURMOFs yields new thin film MOF-polymer composites with potential electrical applications. By reviewing the literature, it could be shown that bulk MOF powders are mainly used for the polymerization reaction instead of SURMOFs. SURMOFs, due to their nature as nanometer scaled film, deliver different advantages, such as being a homogeneous coating with high crystallinity, making them highly interesting, especially for electronic applications or for controlled polymerization.

It is expected that in the near future, new techniques and technologies will be developed on the basis of SURMOF and SURMOF-polymer composites. Performing the polymerization reactions inside the SURMOFs in confined space could lead to highly homogeneous molecular weight distribution in polymer synthesis. Additionally, the effect of the SURMOF structures on the formation of the polymers can be further investigated. The loading of the monomers inside the pores of SURMOFs can be studied and optimized by gas-phase loading instead of drop-casting. By optimizing these conditions, improved electrical conductivity can be achieved in

Polymer:SURMOF thin films, which might become useful for biological films, in capacitors/supercapacitors or capacitive sensing of target molecules.
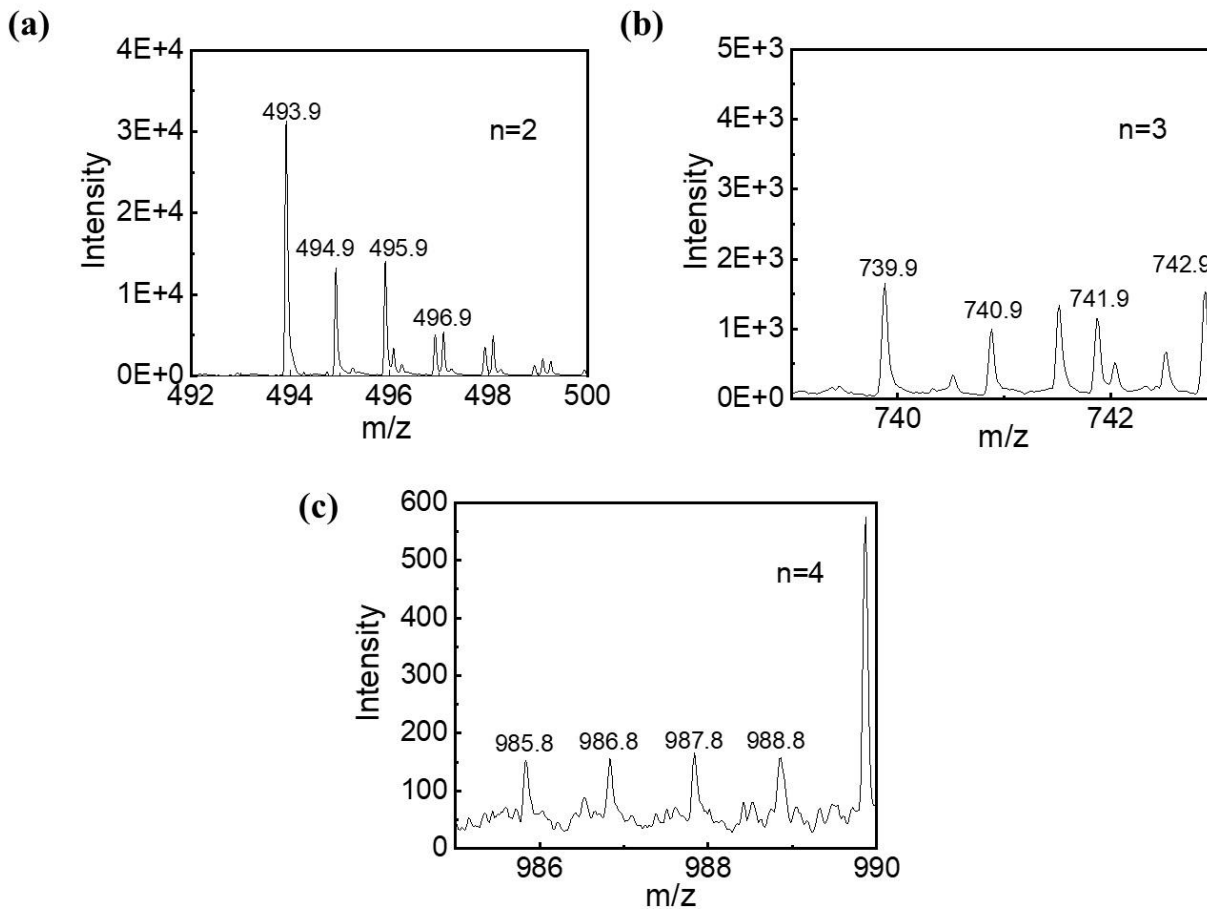
6. APPENDIX

6.1 Appendix A

(a)

(b)

(c)

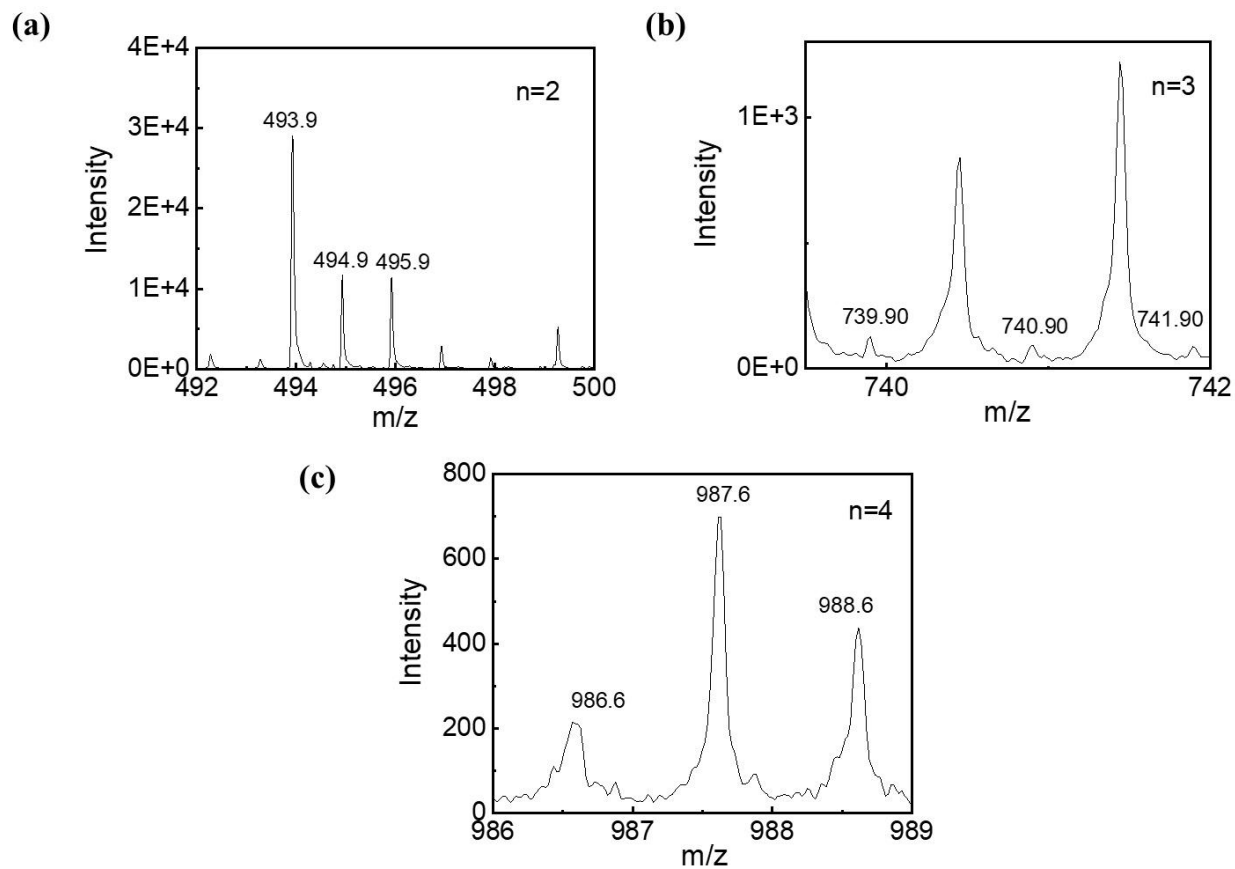*Figure 6.1 : Isotopic mass distribution of PTth for (a) n=2, (b) n=3 and (c) n=4 formed in **PTTh:1**.*

Figure 6.2 : Isotopic mass distribution of PTth for (a) n=1, (b) n=2, and (c) n=4 formed in **PTth:1a***.*
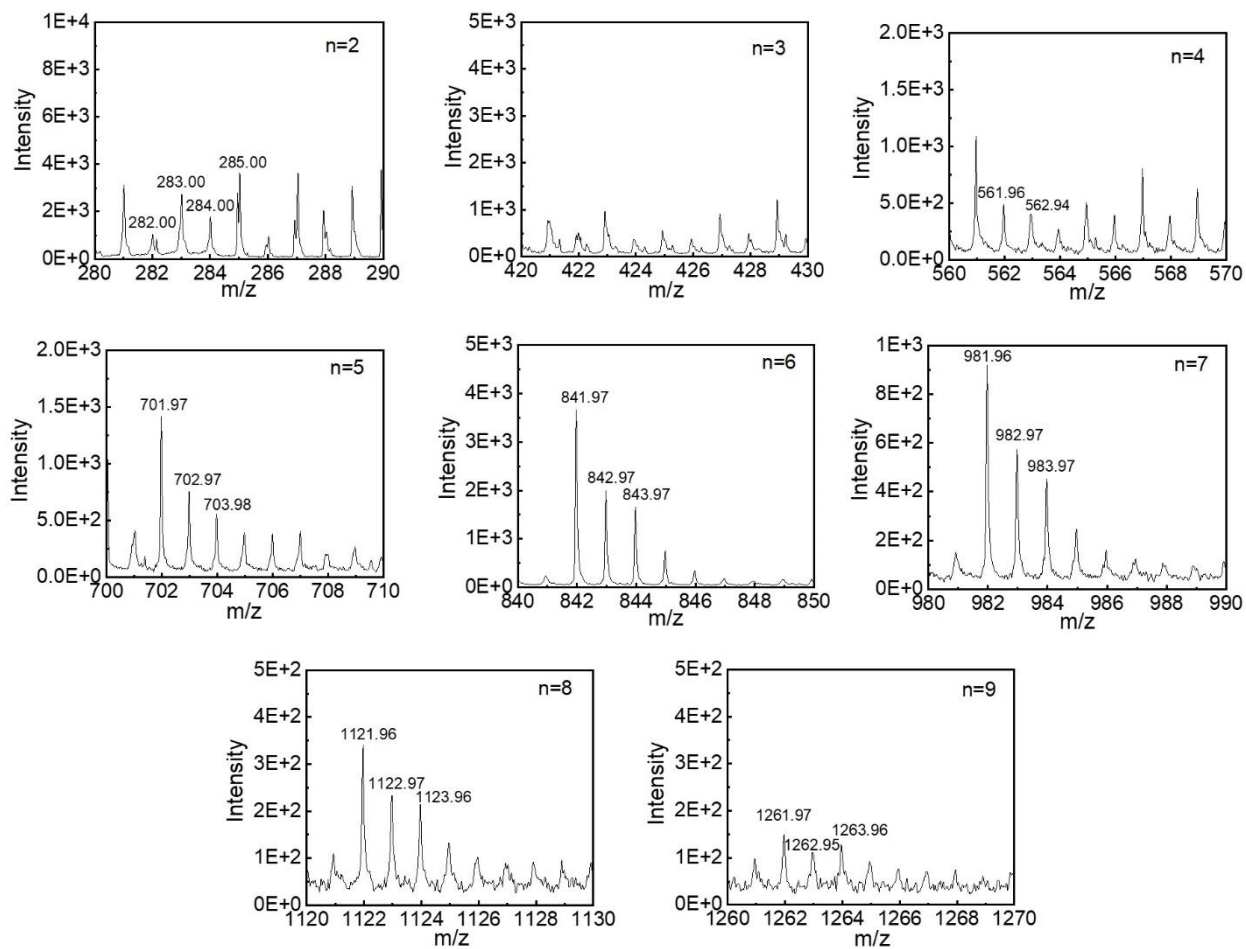
*Figure 6.3 : Isotopic mass distribution of PEDOT formed in **PEDOT:2** with a length of up to n=9.*

6.2 Appendix B

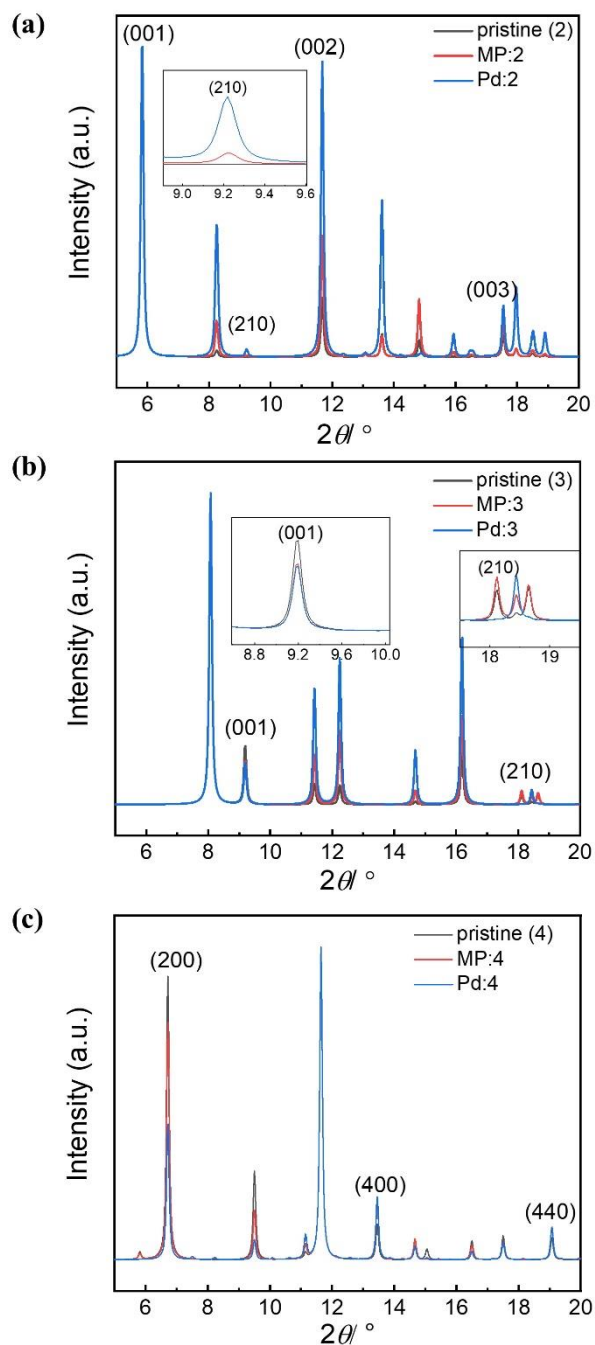*Figure 6.4 : XRD patterns of (a) **1** (b) **2** and (c) **3** after the modelling the non-oriented structures (black: pristine sample, red: MP loaded sample, blue: Pd loaded sample).*
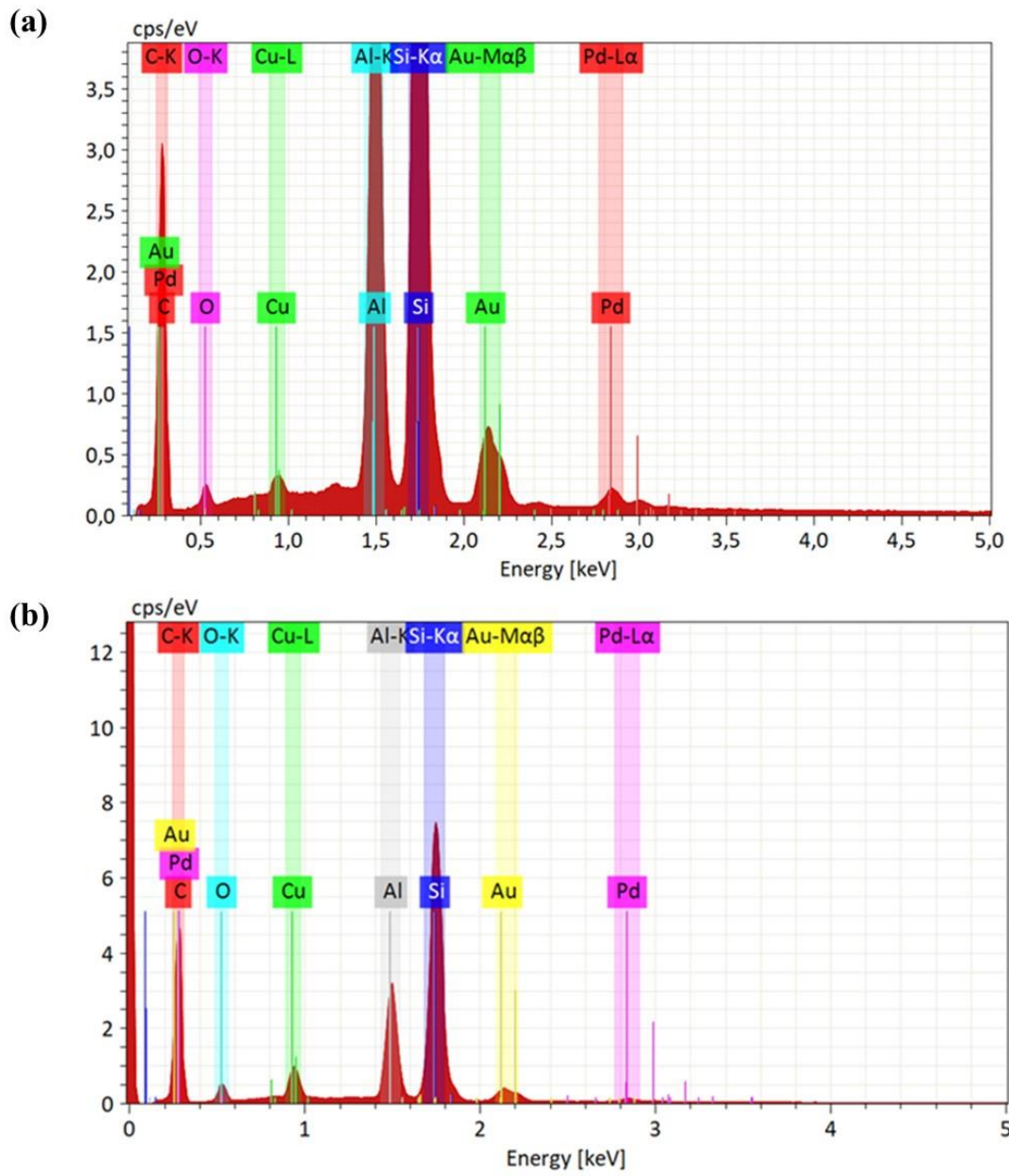
*Figure 6.5 : EDXS of the (a) pristine **2** (b) **PolyMP:2**.*
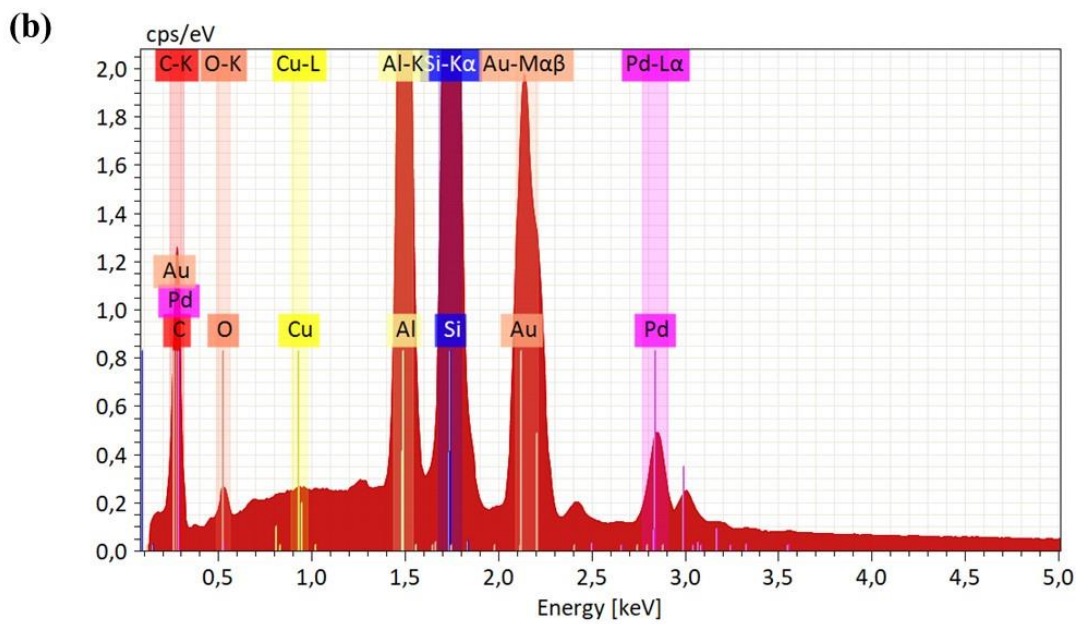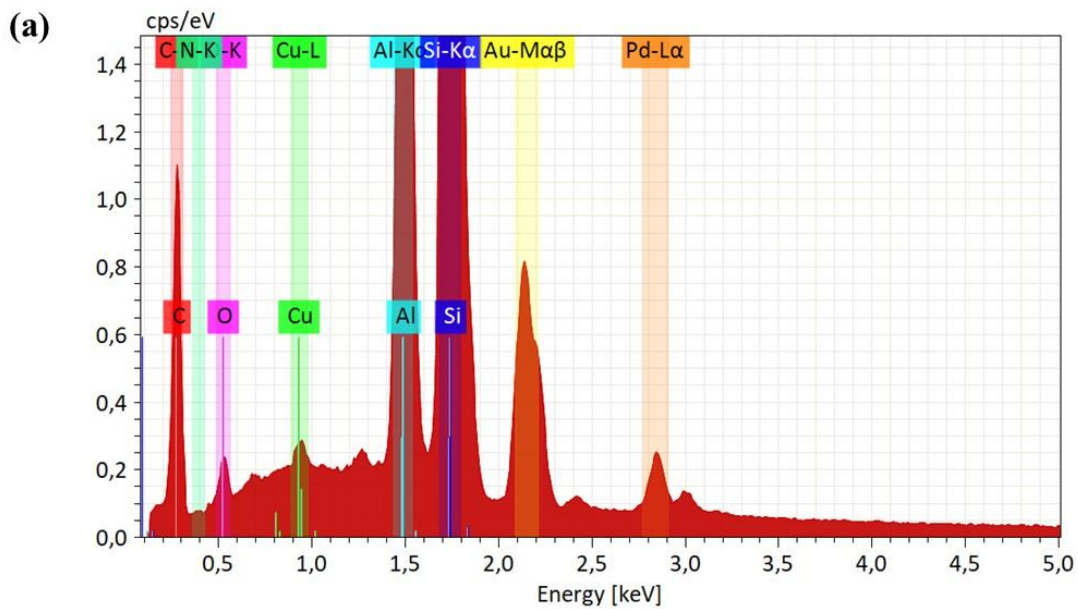
*Figure 6.6 : EDXS of the (a) pristine **3** (b) **PolyMP:3**.*

(a)

(b)
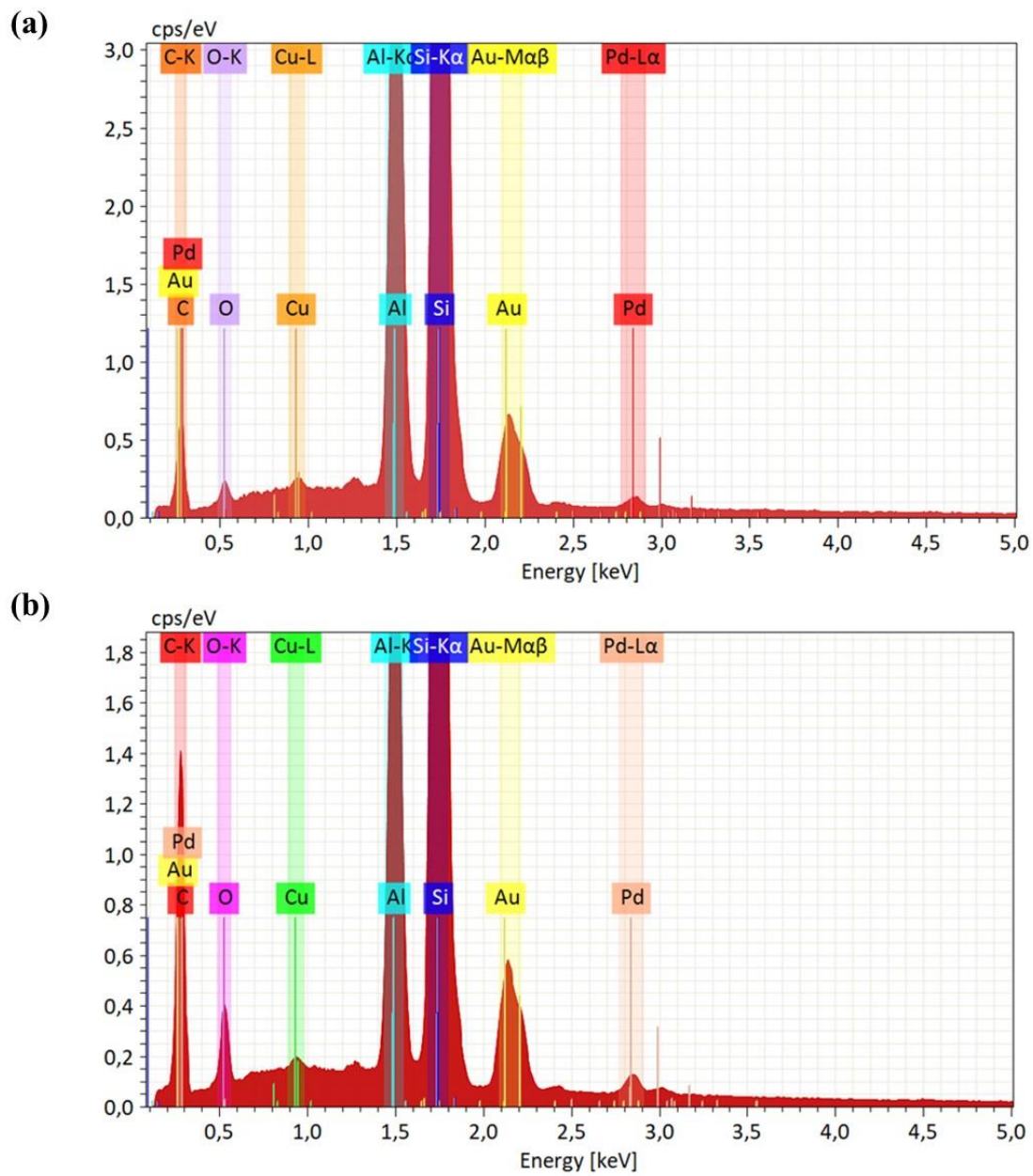
*Figure 6.7 : EDXS of the (a) pristine **4** (b) **PolyMP:4**.*
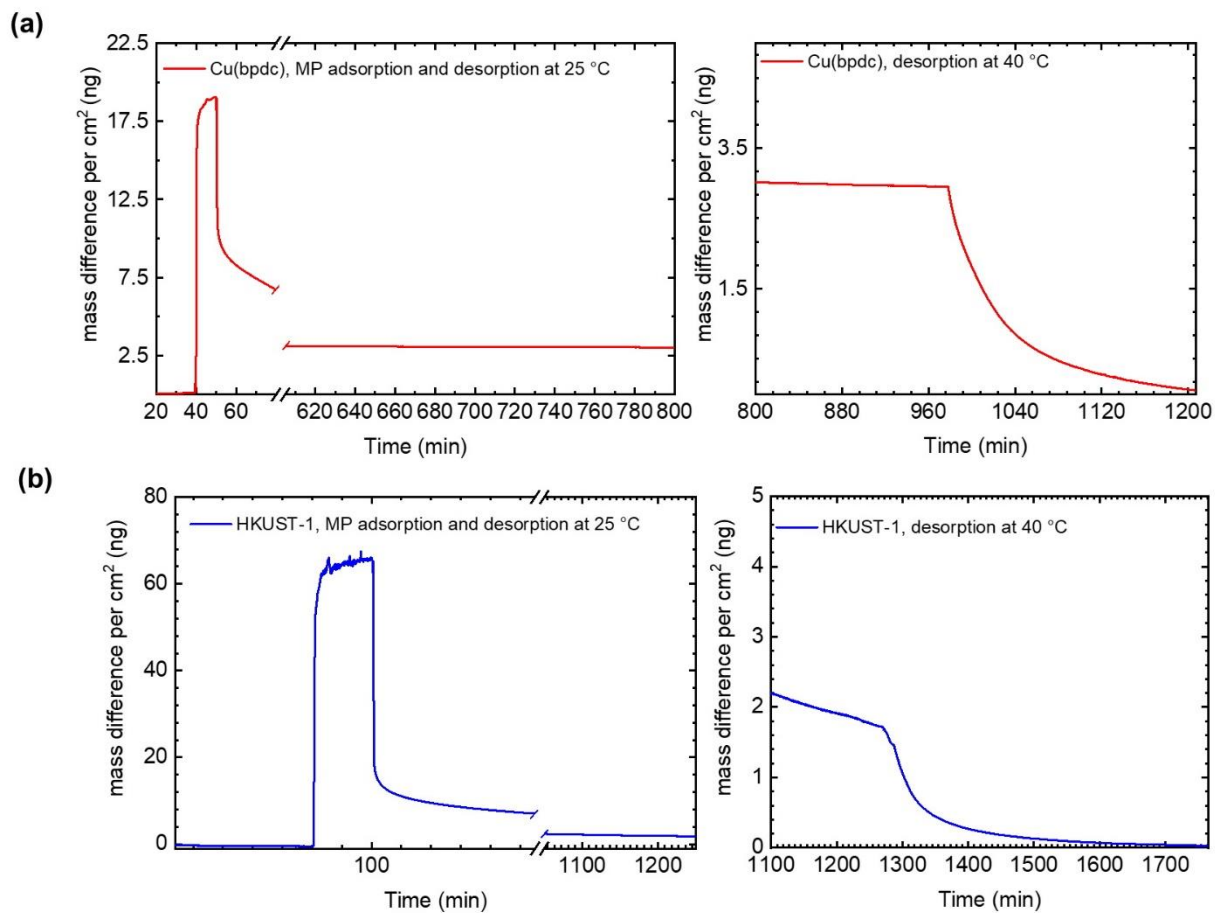
Figure 6.8 : Adsorption/desorption kinetics of the thin films of (a) **2** *and (b)* **4**.
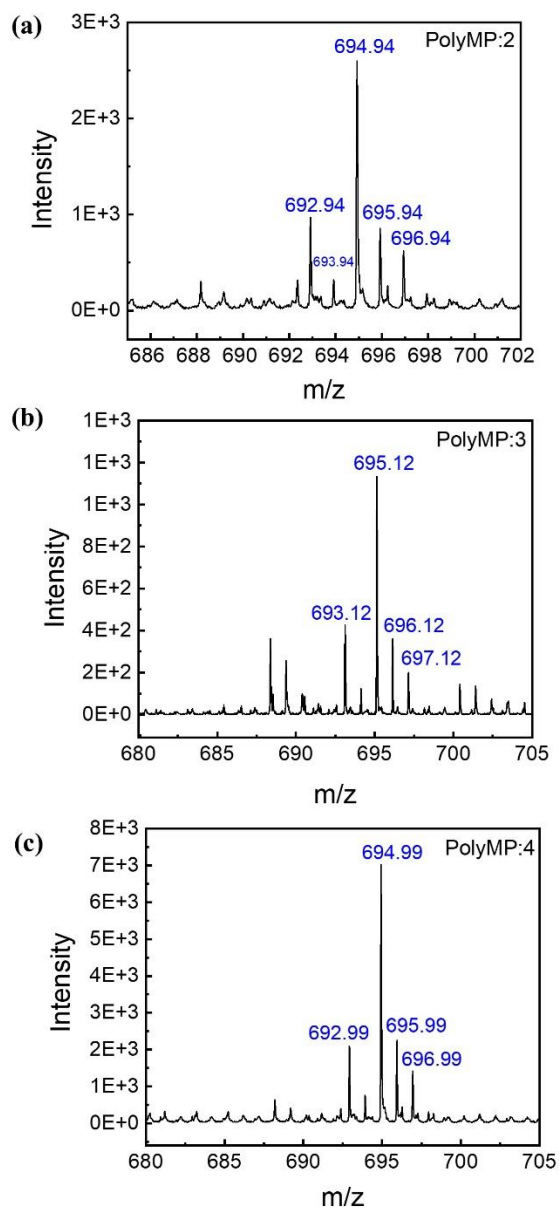
*Figure 6.9 : Isotopic patterns of **PolyMP** with a length of n=8 for (a) **PolyMP:2** (b)**PolyMP:3** and (c) **PolyMP:4**.*
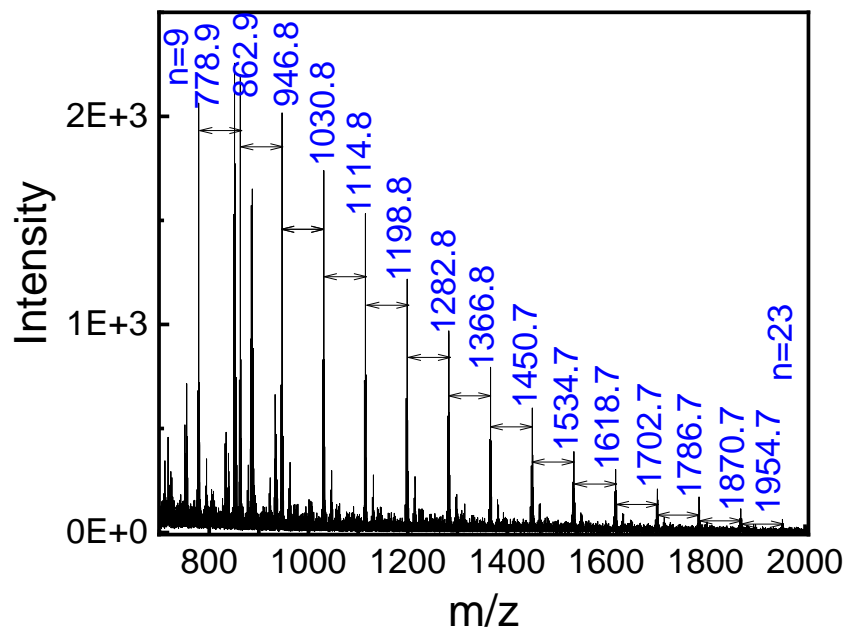
*Figure 6.10 : MALDI-ToF spectrum of bulk **PolyMP** formed in solution.*

Total ion distribution   **Cu-**   **^{65}Cu-**   **$C_4H_3O_2$-**
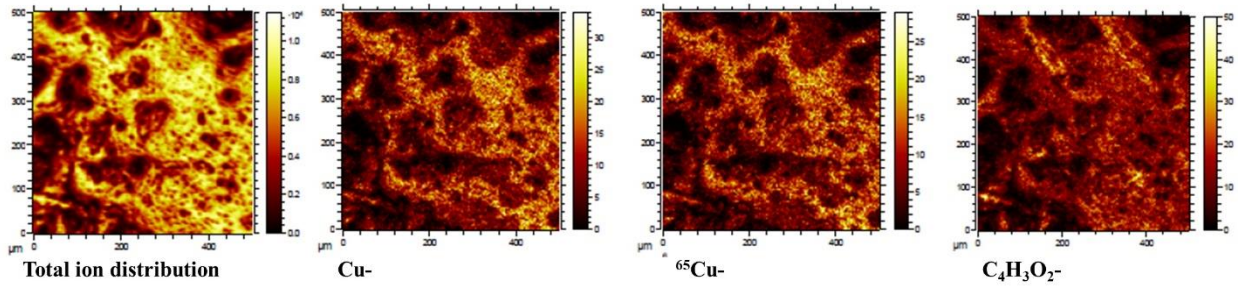
*Figure 6.11 : Depth integrated images of **PolyMP:2** from ToF-SIMS analysis.*

Total ion distribution   **Combined (Cu-, ^{65}Cu-)**   **$C_4H_3O_2$-**
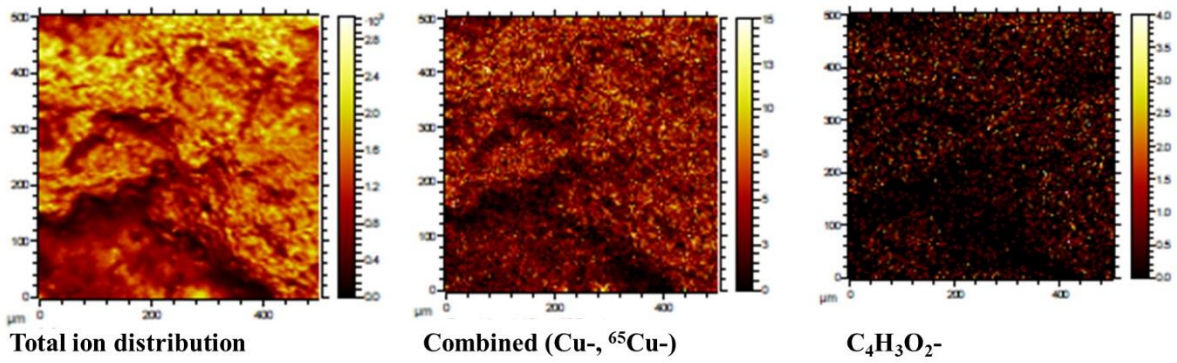
*Figure 6.12 : Depth integrated images of **PolyMP:3** from ToF-SIMS analysis.*

Total ion distribution   **Combined (Cu-, ^{65}Cu-)**   **$C_4H_3O_2$-**
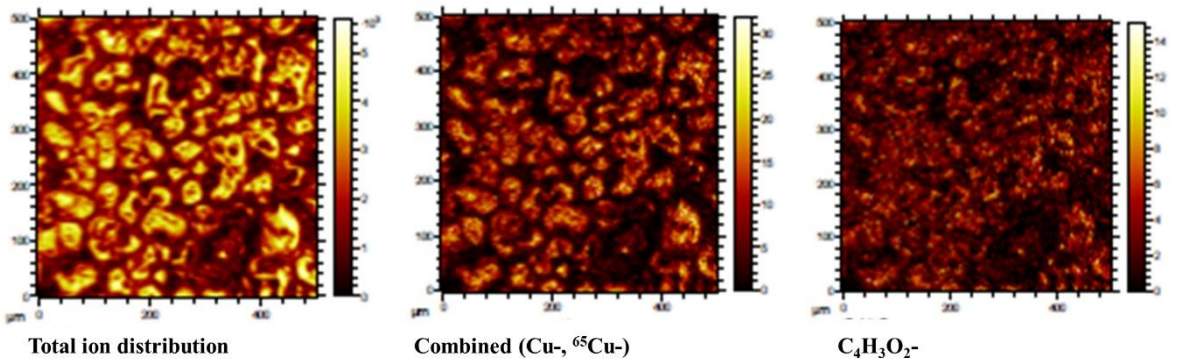
*Figure 6.13 : Depth integrated images of **PolyMP:4** from ToF-SIMS analysis.*

77
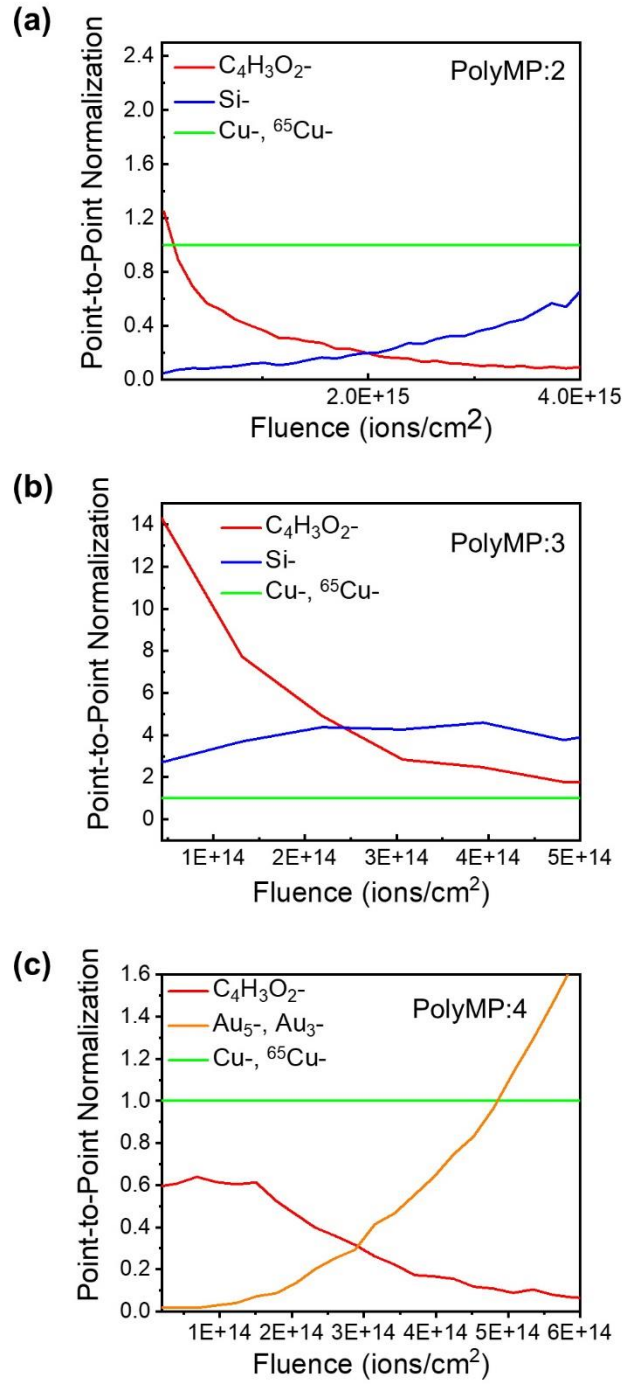
*Figure 6.14 : Depth profiles of (a) **PolyMP:2** (b) **PolyMP:3** and (c) **PolyMP:4** with normalization on the Cu-signal.*

6.3 APPENDIX C

List of Abbreviations

°	degree
µA	microamper
µm	micrometer
µm/m	microsiemens per meter
1D	one-dimensional
2D	two-dimensional
3D	three-dimensional
Å	Angstrom
a.u.	arbitrary unit
AFM	atomic force microscopy
bdc	1,4-benzenedicarboxylic acid
bpdc	4,4- biphyenyldicarboxylic acid
btc	1,3,5-benzenetricarboxylic acid
℃	degree Celsius
dabco	1,4-diazabicyclo(2.2.2)octane
DCTB	trans-2-[3-(4-tert-Butylphenyl)-2-methyl-2-propenylidene]malononitrile
EDOT	3,4-ethylenedioxythiophene
EDX	energy-dispersive X-ray
EDXM	energy-dispersive X-ray mapping
EDXS	energy-dispersive X-ray spectroscopy
FTIR	fourier transform infrared
h	hour(s)

HKUST-1	Hong Kong University of Science and Technology-1
IR	infrared spectroscopy
IRRAS	infrared reflection absorption spectroscopy
K	Kelvin
LB	Langmuir Blodgett
LBL	layer-by-layer
LPE	liquid phase epitaxy
MALDI-ToF/MS	matrix-assisted laser desorption ionization time of flight mass spectrometry
MHDA	16-mercaptohexadecanoic acid
min	minute
mL	milliliter
mM	millimolar
MOF	metal-organic framework
MP	methyl propiolate
MUD	11-mercapto-1-undecanol
nm	nanometer
pA	picoamper
PEDOT	poly(3,4-ethylenedioxythiophene)
Poly(MP)	poly(methyl propiolate)
pS/m	picosiemens per meter
PTth	poly/(terthiophene)
QCM	quartz crystal microbalance
S	Siemens
SAM	self-assembled monolayer
SBU	secondary building unit

SEM	scanning electron microscopy
SURMOF	surface-mounted metal-organic framework
THF	tetrahydrofuran
ToF-SIMS	time-of-flight secondary ion mass spectrometry
Tth	2,2′:5′,2″-Terthiophene
UHV	ultra-high vacuum
UV	ultraviolet
UV-Vis	ultraviolet-visible spectroscopy
V	voltage
XRD	X-ray diffraction

7. REFERENCES

1.	Zhou, H. C.; Kitagawa, S., Metal-Organic Frameworks (MOFs). *Chem. Soc. Rev.* **2014,** *43* (16), 5415-5418.

2.	Gliemann, H.; Wöll, C., Epitaxially grown metalorganic frameworks. *Mater. Today* **2012,** *15* (3), 110-116.

3.	Yaghi, O. M.; Li, H., Hydrothermal Synthesis of a Metal-Organic Framework Containing Large Rectangular Channels. *J. Am. Chem. Soc.* **1995,** *117* (41), 10401-10402.

4.	Tibbetts, I.; Kostakis, G. E., Recent bio-advances in metal-organic frameworks. *Molecules* **2020,** *25* (6), 1291.

5.	Tao, C.-a.; Wang, J.; Chen, R., Metal Organic Frameworks-Based Optical Thin Films. In *Multilayer Thin Films-Versatile Applications for Materials Engineering*, IntechOpen: 2020.

6.	Howarth, A. J.; Liu, Y.; Li, P.; Li, Z.; Wang, T. C.; Hupp, J. T.; Farha, O. K., Chemical, thermal and mechanical stabilities of metal organic frameworks. *Nat. Rev. Mater.* **2016,** *1*, 15018.

7.	Tranchemontagne, D. J.; Mendoza-Cortes, J. L.; O'Keeffe, M.; Yaghi, O. M., Secondary building units, nets and bonding in the chemistry of metal-organic frameworks. *Chem. Soc. Rev.* **2009,** *38* (5), 1257-1283.

8.	Zhao, L.-M.; Zhang, Z.-J.; Zhang, S.-Y.; Cui, P.; Shi, W.; Zhao, B.; Cheng, P.; Liao, D.-Z.; Yan, S.-P., Metal–organic frameworks based on transition-metal carboxylate clusters as secondary building units: synthesis, structures and properties. *CrystEngComm* **2011,** *13* (3), 907-913.

9.	Köberl, M.; Cokoja, M.; Herrmann, W. A.; Kuehn, F. E., From molecules to materials: Molecular paddle-wheel synthons of macromolecules, cage compounds and metal–organic frameworks. *Dalton Trans.* **2011,** *40* (26), 6834-6859.

10.	Chen, Y.; Wang, B.; Wang, X.; Xie, L.-H.; Li, J.; Xie, Y.; Li, J.-R., A Copper(II)-Paddlewheel Metal–Organic Framework with Exceptional Hydrolytic Stability and Selective Adsorption and Detection Ability of Aniline in Water. *ACS Appl. Mater. Interfaces* **2017,** *9* (32), 27027-27035.

11.	Ryzhikov, M. R.; Kozlova, S. G., Understanding structural flexibility of the paddle-wheel Zn-SBU motif in MOFs: influence of pillar ligands. *Phys. Chem. Chem. Physics* **2019,** *21* (22), 11977-11982.

12.   Dey, C.; Kundu, T.; Biswal, B. P.; Mallick, A.; Banerjee, R., Crystalline metal-organic frameworks (MOFs): synthesis, structure and function. *Acta Crystallog. Section B: Structural Science, Crystal Engineering and Materials* **2014,** *70* (1), 3-10.

13.   Farha, O. K.; Hupp, J. T., Rational Design, Synthesis, Purification, and Activation of Metal−Organic Framework Materials. *Acc. Chem. Res.* **2010,** *43* (8), 1166-1175.

14.   Zhou, H. C.; Long, J. R.; Yaghi, O. M., Introduction to Metal-Organic Frameworks. *Chem. Rev.* **2012,** *112* (2), 673-674.

15.   Chui, S. S.-Y.; Lo, S. M.-F.; Charmant, J. P.; Orpen, A. G.; Williams, I. D., A chemically functionalizable nanoporous material [Cu3 (TMA) 2 (H2O) 3] n. *Science* **1999,** *283* (5405), 1148-1150.

16.   Li, H.; Eddaoudi, M.; O'Keeffe, M.; Yaghi, O. M., Design and synthesis of an exceptionally stable and highly porous metal-organic framework. *Nature* **1999,** *402* (6759), 276-279.

17.   Goldman, M.; Huang, Y., Conformational analysis of 1, 2-dichloroethane adsorbed in metal-organic frameworks. *Vib. Spectrosc.* **2018,** *95*, 68-74.

18.   Wagner, A., Preparation, functionalization and analysis of UiO-66 metal-organic framework thin films on silicon photocathodes. 2015.

19.   Lee, Y.-R.; Kim, J.; Ahn, W.-S., Synthesis of metal-organic frameworks: A mini review. *Korean J. Chem. Eng.* **2013,** *30* (9), 1667-1680.

20.   Stock, N.; Biswas, S., Synthesis of Metal-Organic Frameworks (MOFs): Routes to Various MOF Topologies, Morphologies, and Composites. *Chem. Rev.* **2012,** *112* (2), 933-969.

21.   Sun, Y.; Zhou, H. C., Recent progress in the synthesis of metal-organic frameworks. *Sci. Technol. Adv. Mater.* **2015,** *16* (5), 054202.

22.   García, H.; Navalón, S., *Metal-Organic Frameworks: Applications in Separations and Catalysis*. John Wiley & Sons: 2018.

23.   James, S. L., Metal-organic frameworks. *Chem. Soc. Rev.* **2003,** *32* (5), 276-288.

24.   Li, J.-R.; Kuppler, R. J.; Zhou, H.-C., Selective gas adsorption and separation in metal–organic frameworks. *Chem. Soc. Rev.* **2009,** *38* (5), 1477-1504.

25.   Maldonado, R. R.; Zhang, X.; Hanna, S.; Gong, X.; Gianneschi, N. C.; Hupp, J. T.; Farha, O. K., Squeezing the box: isoreticular contraction of pyrene-based linker in a Zr-based metal–organic framework for Xe/Kr separation. *Dalton Trans.* **2020,** *49* (20), 6553-6556.

26.   Bonneau, M.; Lavenn, C.; Ginet, P.; Otake, K.-i.; Kitagawa, S., Upscale synthesis of a binary pillared layered MOF for hydrocarbon gas storage and separation. *Green Chem.* **2020,** *22* (3), 718-724.

27.   Murray, L. J.; Dincă, M.; Long, J. R., Hydrogen storage in metal–organic frameworks. *Chem. Soc. Rev.* **2009,** *38* (5), 1294-1314.

28.   Tshuma, P.; Makhubela, B. C.; Öhrström, L.; Bourne, S. A.; Chatterjee, N.; Beas, I. N.; Darkwa, J.; Mehlana, G., Cyclometalation of lanthanum (iii) based MOF for catalytic hydrogenation of carbon dioxide to formate. *RSC Adv.* **2020,** *10* (6), 3593-3605.

29.   Lee, J.; Farha, O. K.; Roberts, J.; Scheidt, K. A.; Nguyen, S. T.; Hupp, J. T., Metal-organic framework materials as catalysts. *Chem. Soc. Rev.* **2009,** *38* (5), 1450-1459.

30.   Horcajada, P.; Serre, C.; Vallet-Regí, M.; Sebban, M.; Taulelle, F.; Férey, G., Metal–organic frameworks as efficient materials for drug delivery. *Angew. Chem.* **2006,** *118* (36), 6120-6124.

31.   Suresh, K.; Matzger, A. J., Enhanced Drug Delivery by Dissolution of Amorphous Drug Encapsulated in a Water Unstable Metal–Organic Framework (MOF). *Angew. Chem.* **2019,** *131* (47), 16946-16950.

32.   Liu, Y.; Xie, X.-Y.; Cheng, C.; Shao, Z.-S.; Wang, H.-S., Strategies to fabricate metal–organic framework (MOF)-based luminescent sensing platforms. *J. Mater. Chem. C* **2019,** *7* (35), 10743-10763.

33.   Tchalala, M.; Bhatt, P.; Chappanda, K.; Tavares, S.; Adil, K.; Belmabkhout, Y.; Shkurenko, A.; Cadiau, A.; Heymans, N.; De Weireld, G., Fluorinated MOF platform for selective removal and sensing of SO 2 from flue gas and air. *Nat. Commun.* **2019,** *10* (1), 1-10.

34.   Mochizuki, S.; Kitao, T.; Uemura, T., Controlled polymerizations using metal–organic frameworks. *Chem. Commun.* **2018,** *54* (84), 11843-11856.

35.   Schmidt, B. V. K. J., Metal-Organic Frameworks in Polymer Science: Polymerization Catalysis, Polymerization Environment, and Hybrid Materials. *Macromol. Rapid Commun.* **2020,** *41* (1), 1900333.

36.   Shekhah, O.; Liu, J.; Fischer, R. A.; Wöll, C., MOF thin films: existing and future applications. *Chem. Soc. Rev.* **2011,** *40* (2), 1081-1106.

37.   Zacher, D.; Shekhah, O.; Wöll, C.; Fischer, R. A., Thin films of metal-organic frameworks. *Chem. Soc. Rev.* **2009,** *38* (5), 1418-1429.

38.   Hermes, S.; Schröder, F.; Chelmowski, R.; Wöll, C.; Fischer, R. A., Selective Nucleation and Growth of Metal−Organic Open Framework Thin Films on Patterned COOH/CF3-Terminated Self-Assembled Monolayers on Au(111). *J. Am. Chem. Soc.* **2005,** *127* (40), 13744-13745.

39.   Horcajada, P.; Serre, C.; Grosso, D.; Boissière, C.; Perruchas, S.; Sanchez, C.; Férey, G., Colloidal Route for Preparing Optical Thin Films of Nanoporous Metal–Organic Frameworks. *Adv. Mater.* **2009,** *21* (19), 1931-1935.

40.   Makiura, R.; Motoyama, S.; Umemura, Y.; Yamanaka, H.; Sakata, O.; Kitagawa, H., Surface nano-architecture of a metal-organic framework. *Nat. Mater.* **2010,** *9* (7), 565-71.

41.   Gascon, J.; Aguado, S.; Kapteijn, F., Manufacture of dense coatings of Cu3(BTC)2 (HKUST-1) on α-alumina. *Micropor. Mesopor. Mater.* **2008,** *113* (1), 132-138.

42.   Li, M.; Dincă, M., Selective formation of biphasic thin films of metal–organic frameworks by potential-controlled cathodic electrodeposition. *Chem. Sci.* **2014,** *5* (1), 107-111.

43.   Li, Z.-Q.; Zhang, M.; Liu, B.; Guo, C.-Y.; Zhou, M., Rapid fabrication of metal–organic framework thin films using in situ microwave irradiation and its photocatalytic property. *Inorg. Chem. Commun.* **2013,** *36*, 241-244.

44.   Schoedel, A.; Scherb, C.; Bein, T., Oriented Nanoscale Films of Metal–Organic Frameworks By Room-Temperature Gel-Layer Synthesis. *Angew. Chem. Int. Ed.* **2010,** *49* (40), 7225-7228.

45.   Falcaro, P.; Ricco, R.; Doherty, C. M.; Liang, K.; Hill, A. J.; Styles, M. J., MOF positioning technology and device fabrication. *Chem. Soc. Rev.* **2014,** *43* (16), 5513-5560.

46.   Heinke, L.; Tu, M.; Wannapaiboon, S.; Fischer, R. A.; Wöll, C., Surface-mounted metal-organic frameworks for applications in sensing and separation. *Micropor. Mesopor. Mater.* **2015,** *216*, 200-215.

47.   Shekhah, O.; Wang, H.; Kowarik, S.; Schreiber, F.; Paulus, M.; Tolan, M.; Sternemann, C.; Evers, F.; Zacher, D.; Fischer, R. A.; Wöll, C., Step-by-Step Route for the Synthesis of Metal−Organic Frameworks. *J. Am. Chem. Soc.* **2007,** *129* (49), 15118-15119.

48.   Shekhah, O.; Wang, H.; Strunskus, T.; Cyganik, P.; Zacher, D.; Fischer, R.; Wöll, C., Layer-by-Layer Growth of Oriented Metal Organic Polymers on a Functionalized Organic Surface. *Langmuir* **2007,** *23* (14), 7440-7442.

49.   Liu, J. X.; Wöll, C., Surface-supported metal-organic framework thin films: fabrication methods, applications, and challenges. *Chem. Soc. Rev.* **2017,** *46* (19), 5730-5770.

50.   Liu, Y.-F.; Lee, Y.-L., Adsorption characteristics of OH-terminated alkanethiol and arenethiol on Au(111) surfaces. *Nanoscale* **2012,** *4* (6), 2093-2100.

51.   Arnold, R.; Azzam, W.; Terfort, A.; Wöll, C., Preparation, Modification, and Crystallinity of Aliphatic and Aromatic Carboxylic Acid Terminated Self-Assembled Monolayers. *Langmuir* **2002,** *18* (10), 3980-3992.

52.   Wang, H.; Chen, S.; Li, L.; Jiang, S., Improved method for the preparation of carboxylic acid and amine terminated self-assembled monolayers of alkanethiolates. *Langmuir* **2005,** *21* (7), 2633-6.

53.   Shekhah, O., Layer-by-Layer Method for the Synthesis and Growth of Surface Mounted Metal-Organic Frameworks (SURMOFs). *Materials* **2010,** *3* (2), 1302-1315.

54.   Gu, Z.-G.; Zhang, J., Epitaxial growth and applications of oriented metal–organic framework thin films. *Coord. Chem. Rev.* **2019,** *378*, 513-532.

55.   Liu, J.; Schüpbach, B.; Bashir, A.; Shekhah, O.; Nefedov, A.; Kind, M.; Terfort, A.; Wöll, C., Structural characterization of self-assembled monolayers of pyridine-terminated thiolates on gold. *Phys. Chem. Chem. Phys.* **2010,** *12* (17), 4459-4472.

56.   Kind, M.; Wöll, C., Organic surfaces exposed by self-assembled organothiol monolayers: Preparation, characterization, and application. *Prog. Surf. Sci.* **2009,** *84* (7), 230-278.

57.   Liu, J. X.; Shekhah, O.; Stammer, X.; Arslan, H. K.; Liu, B.; Schupbach, B.; Terfort, A.; Wöll, C., Deposition of Metal-Organic Frameworks by Liquid-Phase Epitaxy: The Influence of Substrate Functional Group Density on Film Orientation. *Materials* **2012,** *5* (9), 1581-1592.

58.   Betard, A.; Fischer, R. A., Metal-Organic Framework Thin Films: From Fundamentals to Applications. *Chem. Rev.* **2012,** *112* (2), 1055-1083.

59.   Liu, B.; Fischer, R. A., Liquid-phase epitaxy of metal organic framework thin films. *Sci. China-Chem.* **2011,** *54* (12), 1851-1866.

60.   Heinke, L.; Gliemann, H.; Tremouilhac, P.; Wöll, C., SURMOFs: Liquid-Phase Epitaxy of Metal–Organic Frameworks on Surfaces. *The Chemistry of Metal–Organic Frameworks: Synthesis, Characterization, and Applications* **2016,** *2*, 523-550.

61.   Shekhah, O.; Wang, H.; Zacher, D.; Fischer, R. A.; Wöll, C., Growth Mechanism of Metal-Organic Frameworks: Insights into the Nucleation by Employing a Step-by-Step Route. *Angew. Chem. Int. Ed.* **2009,** *48* (27), 5038-5041.

62.   Munuera, C.; Shekhah, O.; Wang, H.; Wöll, C.; Ocal, C., The controlled growth of oriented metal–organic frameworks on functionalized surfaces as followed by scanning force microscopy. *Phys. Chem. Chem. Phys.* **2008,** *10* (48), 7257-7261.

63.   St. Petkov, P.; Vayssilov, G. N.; Liu, J.; Shekhah, O.; Wang, Y.; Wöll, C.; Heine, T., Defects in MOFs: A Thorough Characterization. *Chemphyschem* **2012,** *13* (8), 2025-2029.

64.   Arslan, H. K.; Shekhah, O.; Wieland, D. C. F.; Paulus, M.; Sternemann, C.; Schroer, M. A.; Tiemeyer, S.; Tolan, M.; Fischer, R. A.; Wöll, C., Intercalation in Layered Metal–Organic Frameworks: Reversible Inclusion of an Extended π-System. *J. Am. Chem. Soc.* **2011,** *133* (21), 8158-8161.

65.   Gu, Z.-G.; Pfriem, A.; Hamsch, S.; Breitwieser, H.; Wohlgemuth, J.; Heinke, L.; Gliemann, H.; Wöll, C., Transparent films of metal-organic frameworks for optical applications. *Micropor. Mesopor. Mater* **2015,** *211*, 82-87.

66.   Heinke, L.; Gu, Z.; Wöll, C., The surface barrier phenomenon at the loading of metal-organic frameworks. *Nat. Commun.* **2014,** *5* (1), 1-6.

67.   Kitao, T.; Uemura, T., Polymers in Metal–Organic Frameworks: From Nanostructured Chain Assemblies to New Functional Materials. *Chem. Lett.* **2020,** *49* (6), 624-632.

68.   Uemura, T.; Kitagawa, K.; Horike, S.; Kawamura, T.; Kitagawa, S.; Mizuno, M.; Endo, K., Radical polymerisation of styrene in porous coordination polymers. *Chem. Commun.* **2005,** (48), 5968-5970.

69.   Uemura, T.; Yanai, N.; Kitagawa, S., Polymerization reactions in porous coordination polymers. *Chem. Soc. Rev.* **2009,** *38* (5), 1228-1236.

70.   Uemura, T.; Ono, Y.; Kitagawa, S., Radical copolymerizations of vinyl monomers in a porous coordination polymer. *Chem. Lett.* **2008,** *37* (6), 616-617.

71.   Uemura, T.; Ono, Y.; Kitagawa, K.; Kitagawa, S., Radical polymerization of vinyl monomers in porous coordination polymers: Nanochannel size effects on reactivity, molecular weight, and stereostructure. *Macromolecules* **2008,** *41* (1), 87-94.

72.   Uemura, T.; Hiramatsu, D.; Kubota, Y.; Takata, M.; Kitagawa, S., Topotactic Linear Radical Polymerization of Divinylbenzenes in Porous Coordination Polymers. *Angew. Chem. Int. Ed.* **2007,** *46* (26), 4987-4990.

73.   Hwang, J.; Lee, H.-C.; Antonietti, M.; Schmidt, B. V. K. J., Free radical and RAFT polymerization of vinyl esters in metal–organic-frameworks. *Polym. Chem.* **2017,** *8* (40), 6204-6208.

74.   Uemura, T.; Kaseda, T.; Sasaki, Y.; Inukai, M.; Toriyama, T.; Takahara, A.; Jinnai, H.; Kitagawa, S., Mixing of immiscible polymers using nanoporous coordination templates. *Nat. Commun.* **2015,** *6* (1), 7473.

75.   Yanai, N.; Uemura, T.; Ohba, M.; Kadowaki, Y.; Maesato, M.; Takenaka, M.; Nishitsuji, S.; Hasegawa, H.; Kitagawa, S., Fabrication of Two-Dimensional Polymer Arrays: Template Synthesis of Polypyrrole between Redox-Active Coordination Nanoslits. *Angew. Chem. Int. Ed.* **2008,** *47* (51), 9883-9886.

76.   Uemura, T.; Kadowaki, Y.; Yanai, N.; Kitagawa, S., Template Synthesis of Porous Polypyrrole in 3D Coordination Nanochannels. *Chem. Mater.* **2009,** *21* (18), 4096-4098.

77.   MacLean, M. W. A.; Kitao, T.; Suga, T.; Mizuno, M.; Seki, S.; Uemura, T.; Kitagawa, S., Unraveling Inter- and Intrachain Electronics in Polythiophene Assemblies Mediated by Coordination Nanospaces. *Angew. Chem. Int. Ed.* **2016,** *55* (2), 708-713.

78.   Lu, C.; Ben, T.; Xu, S.; Qiu, S., Electrochemical Synthesis of a Microporous Conductive Polymer Based on a Metal–Organic Framework Thin Film. *Angew. Chem. Int. Ed.* **2014,** *53* (25), 6454-6458.

79.   Haldar, R.; Sen, B.; Hurrle, S.; Kitao, T.; Sankhla, R.; Kühl, B.; Welle, A.; Heissler, S.; Brenner-Weiß, G.; Thissen, P.; Uemura, T.; Gliemann, H.; Barner-Kowollik, C.; Wöll, C., Oxidative polymerization of terthiophene and a substituted thiophene monomer in metal-organic framework thin films. *Eur. Polym. J.* **2018,** *109*, 162-168.

80.   Kobayashi, Y.; Horie, Y.; Honjo, K.; Uemura, T.; Kitagawa, S., The controlled synthesis of polyglucose in one-dimensional coordination nanochannels. *Chem. Commun.* **2016,** *52* (29), 5156-5159.

81.   Uemura, T.; Kitaura, R.; Ohta, Y.; Nagaoka, M.; Kitagawa, S., Nanochannel-Promoted Polymerization of Substituted Acetylenes in Porous Coordination Polymers. *Angew. Chem. Int. Ed.* **2006,** *45* (25), 4112-4116.

82.   Park, I.-H.; Chanthapally, A.; Lee, H.-H.; Quah, H. S.; Lee, S. S.; Vittal, J. J., Solid-state conversion of a MOF to a metal-organo polymeric framework (MOPF) via [2+2] cycloaddition reaction. *Chem. Commun.* **2014,** *50* (28), 3665-3667.

83.   Uemura, T.; Mochizuki, S.; Kitagawa, S., Radical Copolymerization Mediated by Unsaturated Metal Sites in Coordination Nanochannels. *ACS Macro Lett.* **2015,** *4* (7), 788-791.

84.   Marshall, N.; James, W.; Fulmer, J.; Crittenden, S.; Thompson, A. B.; Ward, P. A.; Rowe, G. T., Polythiophene Doping of the Cu-Based Metal–Organic Framework (MOF) HKUST-1 Using Innate MOF-Initiated Oxidative Polymerization. *Inorg. Chem.* **2019,** *58* (9), 5561-5575.

85.   Gu, Z.-G.; Fu, W.-Q.; Liu, M.; Zhang, J., Surface-mounted MOF templated fabrication of homochiral polymer thin film for enantioselective adsorption of drugs. *Chem. Commun.* **2017,** *53* (9), 1470-1473.

86.   Lu, C.; Ben, T.; Xu, S.; Qiu, S., Electrochemical synthesis of a microporous conductive polymer based on a metal–organic framework thin film. *Angew. Chem.* **2014,** *126* (25), 6572-6576.

87.   Klyatskaya, S.; Kanj, A. B.; Molina-Jirón, C.; Heidrich, S.; Velasco, L.; Natzeck, C.; Gliemann, H.; Heissler, S.; Weidler, P.; Wenzel, W.; Bufon, C. C. B.; Heinke, L.; Wöll, C.; Ruben, M., Conductive Metal–Organic Framework Thin Film Hybrids by Electropolymerization of Monosubstituted Acetylenes. *ACS Appl. Mater. Interfaces* **2020,** *12* (27), 30972-30979.

88.   Widjonarko, N. E., Introduction to advanced x-ray diffraction techniques for polymeric thin films. *Coatings* **2016,** *6* (4), 54.

89.   Dinnebier, R. E.; Friese, K., Modern XRD methods in mineralogy. *Introduction to the Mineralogical Sciences: Encyclopedia of Life Support Systems (EOLSS)* **2003**.

90.   Bunaciu, A. A.; UdriŞTioiu, E. G.; Aboul-Enein, H. Y., X-ray diffraction: instrumentation and applications. *Crit. Rev. Anal. Chem.* **2015,** *45* (4), 289-299.

91.   Unruh, D. K.; Forbes, T. Z., X-ray Diffraction Techniques. In *Analytical Geomicrobiology: A Handbook of Instrumental Techniques*, Alessi, D. S.; Veeramani, H.; Kenney, J. P. L., Eds. Cambridge University Press: Cambridge, 2019; pp 215-237.

92.   Inaba, K., X-ray thin-film measurement techniques. *The Rigaku Journal* **2008,** *24* (1), 10-12.

93.   Kato, K.; Omoto, H.; Takamatsu, A., Influence of cathode voltage on electrical property and crystal structure of sputter-deposited Ag thin films. *Vacuum* **2009,** *84* (5), 587-591.

94.   Larkin, P., *Infrared and Raman spectroscopy: principles and spectral interpretation*. Elsevier: 2017.

95.   Smith, B. C., *Fundamentals of Fourier transform infrared spectroscopy*. CRC press: 2011.

96.   Vinh, N. G.; Ngu, M. V.; Lan, N. T.; Thanh, L. T. K.; Dung, N. T.; Viet, N. A., Some applications using the connection betweenq-deformed harmonic oscillator and symmetric and asymmetric potentials. *Journal of Physics: Conference Series* **2017,** *865*, 012006.

97.   Sharma, S. K.; Verma, D. S.; Khan, L. U.; Kumar, S.; Khan, S. B., *Handbook of Materials Characterization*. Springer: 2018.

98.   Kulkarni, S. K., *Nanotechnology: principles and practices*. Springer: 2014.

99.   Tolstoy, V. P.; Chernyshova, I.; Skryshevsky, V. A., *Handbook of infrared spectroscopy of ultrathin films*. John Wiley & Sons: 2003.

100.   Yoshinobu, J., Infrared Reflection–Absorption Spectroscopy. In *Compendium of Surface and Interface Analysis*, The Surface Science Society of, J., Ed. Springer Singapore: Singapore, 2018; pp 295-299.

101.   Valadez Sánchez, E. P.; Knebel, A.; Izquierdo Sánchez, L.; Klumpp, M.; Wöll, C.; Dittmeyer, R., Studying ZIF-8 SURMOF Thin Films with a Langatate Crystal Microbalance: Single-Component Gas Adsorption Isotherms Measured at Elevated Temperatures and Pressures. *Langmuir* **2020,** *36* (29), 8444-8450.

102.   Shekhah, O.; Arslan, H. K.; Chen, K.; Schmittel, M.; Maul, R.; Wenzel, W.; Wöll, C., Post-synthetic modification of epitaxially grown, highly oriented functionalized MOF thin films. *Chem. Commun.* **2011,** *47* (40), 11210-11212.

103.   Popp, J.; Mayerhöfer, T., *Micro-Raman Spectroscopy*. De Gruyter: 2020.

104.   Smith, E.; Dent, G., Modern Raman spectroscopy: a practical approach. **2005**.

105.   Wang, Z.; Błaszczyk, A.; Fuhr, O.; Heissler, S.; Wöll, C.; Mayor, M., Molecular weaving via surface-templated epitaxy of crystalline coordination networks. *Nat. Commun.* **2017,** *8* (1), 14442.

106.   Sokolov, M. R.; Enakieva, Y. Y.; Yapryntsev, A. D.; Shiryaev, A. A.; Zvyagina, A. I.; Kalinina, M. A., Intercalation of Porphyrin-Based SURMOF in Layered Eu(III) Hydroxide: An Approach Toward Symbimetic Hybrid Materials. *Adv. Funct. Mater.* **2020,** *30* (27), 2000681.

107.   Sagadevan, S.; Murugasen, P., Studies on optical, mechanical and electrical properties of organic nonlinear optical p-Toluidine p-Toluenesulfonate single crystal. *J. Crystn. Process Technol.* **2014,** *2014*.

108.   Khan, S. A.; Khan, S. B.; Khan, L. U.; Farooq, A.; Akhtar, K.; Asiri, A. M., Fourier transform infrared spectroscopy: fundamentals and application in functional groups and nanomaterials characterization. In *Handbook of Materials Characterization*, Springer: 2018; pp 317-344.

109.   Fleming, I.; Williams, D. H., *Spectroscopic methods in organic chemistry*. Springer: 1966.

110. Müller, K.; Wadhwa, J.; Singh Malhi, J.; Schöttner, L.; Welle, A.; Schwartz, H.; Hermann, D.; Ruschewitz, U.; Heinke, L., Photoswitchable nanoporous films by loading azobenzene in metal–organic frameworks of type HKUST-1. *Chem. Commun.* **2017,** *53* (57), 8070-8073.

111. Müller, K.; Knebel, A.; Zhao, F.; Bléger, D.; Caro, J.; Heinke, L., Switching Thin Films of Azobenzene-Containing Metal–Organic Frameworks with Visible Light. *Chem. Eur. J.* **2017,** *23* (23), 5434-5438.

112. Hosseini, S.; Martinez-Chapa, S. O., *Fundamentals of MALDI-ToF-MS Analysis: Applications in Bio-diagnosis, Tissue Engineering and Drug Delivery*. Springer: 2016.

113. Barner-Kowollik, C.; Gruendling, T.; Falkenhagen, J.; Weidner, S., *Mass spectrometry in polymer chemistry*. John Wiley & Sons: 2012.

114. Karas, M.; Bachmann, D.; Hillenkamp, F., Influence of the wavelength in high-irradiance ultraviolet laser desorption mass spectrometry of organic molecules. *Anal. Chem.* **1985,** *57* (14), 2935-2939.

115. Vogel, N.; Schiebel, K.; Humeny, A., Technologies in the whole-genome age: MALDI-TOF-based genotyping. *Transfus. Med. Hemother.* **2009,** *36* (4), 253-262.

116. Singhal, N.; Kumar, M.; Kanaujia, P. K.; Virdi, J. S., MALDI-TOF mass spectrometry: an emerging technology for microbial identification and diagnosis. *Front. Microbiol.* **2015,** *6* (791).

117. Jurinke, C.; Oeth, P.; van den Boom, D., MALDI-TOF mass spectrometry. *Mol. Biotechnol.* **2004,** *26* (2), 147-163.

118. Stephan, T., TOF-SIMS in cosmochemistry. *Planet. Space Sci.* **2001,** *49* (9), 859-906.

119. Vickerman, J. C., ToF-SIMS—an overview. *ToF-SIMS: surface analysis by mass spectrometry* **2001**, 1-40.

120. Fearn, S., *An introduction to time-of-flight secondary ion mass spectrometry (ToF-SIMS) and its application to materials science*. Morgan & Claypool Publishers San Rafael, CA, USA: 2015.

121. Saha, B.; Chakraborty, P., MCsn+-SIMS: An Innovative Approach for Direct Compositional Analysis of Materials without Standards. *Energy Procedia* **2013,** *41*, 80-109.

122. Ladnorg, T.; Welle, A.; Heißler, S.; Wöll, C.; Gliemann, H., Site-selective growth of surface-anchored metal-organic frameworks on self-assembled monolayer patterns prepared by AFM nanografting. *Beilstein J. Nanotechnol.* **2013,** *4*, 638-48.

123.   Baroni, N.; Turshatov, A.; Oldenburg, M.; Busko, D.; Adams, M.; Haldar, R.; Welle, A.; Redel, E.; Wöll, C.; Richards, B. S.; Howard, I. A., Facile loading of thin-film surface-anchored metal-organic frameworks with Lewis-base guest molecules. *Mater. Chem. Front.* **2017,** *1* (9), 1888-1894.

124.   Singh, A. K., Chapter 4 - Experimental Methodologies for the Characterization of Nanoparticles. In *Engineered Nanoparticles*, Singh, A. K., Ed. Academic Press: Boston, 2016; pp 125-170.

125.   Inkson, B., Scanning electron microscopy (SEM) and transmission electron microscopy (TEM) for materials characterization. In *Materials characterization using nondestructive evaluation (NDE) methods*, Elsevier: 2016; pp 17-43.

126.   Scimeca, M.; Bischetti, S.; Lamsira, H. K.; Bonfiglio, R.; Bonanno, E., Energy Dispersive X-ray (EDX) microanalysis: A powerful tool in biomedical research and diagnosis. *European journal of histochemistry : EJH* **2018,** *62* (1), 2841-2841.

127.   Thomas, S.; Thomas, R.; Zachariah, A. K.; Kumar, R., *Microscopy methods in nanomaterials characterization*. Elsevier: 2017; Vol. 1.

128.   Uemura, T.; Kaseda, T.; Kitagawa, S., Controlled Synthesis of Anisotropic Polymer Particles Templated by Porous Coordination Polymers. *Chem. Mater.* **2013,** *25* (18), 3772-3776.

129.   Uemura, T.; Kaseda, T.; Sasaki, Y.; Inukai, M.; Toriyama, T.; Takahara, A.; Jinnai, H.; Kitagawa, S., Mixing of immiscible polymers using nanoporous coordination templates. *Nat. Commun.* **2015,** *6*.

130.   Gamage, N. D. H.; McDonald, K. A.; Matzger, A. J., MOF-5-Polystyrene: Direct Production from Monomer, Improved Hydrolytic Stability, and Unique Guest Adsorption. *Angew. Chem. Int. Ed.* **2016,** *55* (39), 12099-12103.

131.   Wang, T. S.; Farajollahi, M.; Henke, S.; Zhu, T. T.; Bajpe, S. R.; Sun, S. J.; Barnard, J. S.; Lee, J. S.; Madden, J. D. W.; Cheetham, A. K.; Smoukov, S. K., Functional conductive nanomaterials via polymerisation in nano-channels: PEDOT in a MOF. *Mater. Horiz.* **2017,** *4* (1), 64-71.

132.   Ding, N.; Li, H.; Feng, X.; Wang, Q.; Wang, S.; Ma, L.; Zhou, J.; Wang, B., Partitioning MOF-5 into Confined and Hydrophobic Compartments for Carbon Capture under Humid Conditions. *J. Am. Chem. Soc.* **2016,** *138* (32), 10100-10103.

133.   Lee, H.-C.; Hwang, J.; Schilde, U.; Antonietti, M.; Matyjaszewski, K.; Schmidt, B. V. K. J., Toward Ultimate Control of Radical Polymerization: Functionalized Metal–Organic

Frameworks as a Robust Environment for Metal-Catalyzed Polymerizations. *Chem. Mater.* **2018,** *30* (9), 2983-2994.

134.   Liu, J. X.; Lukose, B.; Shekhah, O.; Arslan, H. K.; Weidler, P.; Gliemann, H.; Brase, S.; Grosjean, S.; Godt, A.; Feng, X. L.; Mullen, K.; Magdau, I. B.; Heine, T.; Wöll, C., A novel series of isoreticular metal organic frameworks: realizing metastable structures by liquid phase epitaxy. *Sci. Rep.* **2012,** *2*, 5.

135.   Tamanai, A.; Beck, S.; Pucci, A., Mid-infrared characterization of thiophene-based thin polymer films. *Displays* **2013,** *34* (5), 399-405.

136.   Kitao, T.; MacLean, M. W. A.; Le Ouay, B.; Sasaki, Y.; Tsujimoto, M.; Kitagawa, S.; Uemura, T., Preparation of polythiophene microrods with ordered chain alignment using nanoporous coordination template. *Polym. Chem.* **2017,** *8* (34), 3077-5081.

137.   Heinke, L.; Gu, Z.; Wöll, C., The surface barrier phenomenon at the loading of metal-organic frameworks. *Nat. Commun.* **2014,** *5* (1), 4562.

138.   Zainal, M. F.; Mohd, Y., Characterization of PEDOT Films for Electrochromic Applications. *Polym. Plast. Technol. Eng.* **2015,** *54* (3), 276-281.

139.   Gangopadhyay, R.; Das, B.; Molla, M. R., How does PEDOT combine with PSS? Insights from structural studies. *RSC Adv.* **2014,** *4* (83), 43912-43920.

140.   Girtan, M.; Mallet, R.; Socol, M.; Stanculescu, A., On the Physical Properties PEDOT:PSS Thin Films. *Mater. Today Commun.* **2020,** *22*, 100735.

141.   Lang, U.; Naujoks, N.; Dual, J., Mechanical characterization of PEDOT:PSS thin films. *Synth. Met.* **2009,** *159* (5), 473-479.

142.   Le Ouay, B.; Boudot, M.; Kitao, T.; Yanagida, T.; Kitagawa, S.; Uemura, T., Nanostructuration of PEDOT in Porous Coordination Polymers for Tunable Porosity and Conductivity. *J. Am. Chem. Soc.* **2016,** *138* (32), 10088-10091.

143.   Arrozi, U. S. F.; Bon, V.; Kutzscher, C.; Senkovska, I.; Kaskel, S., Towards highly active and stable nickel-based metal–organic frameworks as ethylene oligomerization catalysts. *Dalton Trans.* **2019,** *48* (10), 3415-3421.

144.   Rivera-Torrente, M.; Pletcher, P. D.; Jongkind, M. K.; Nikolopoulos, N.; Weckhuysen, B. M., Ethylene Polymerization over Metal–Organic Framework Crystallites and the Influence of Linkers on Their Fracturing Process. *ACS Catal.* **2019,** *9* (4), 3059-3069.

145.   Zhang, X.; Kitao, T.; Piga, D.; Hongu, R.; Bracco, S.; Comotti, A.; Sozzani, P.; Uemura, T., Carbonization of single polyacrylonitrile chains in coordination nanospaces. *Chem. Sci.* **2020**.

146.   Kitao, T.; MacLean, M. W. A.; Nakata, K.; Takayanagi, M.; Nagaoka, M.; Uemura, T., Scalable and Precise Synthesis of Armchair-Edge Graphene Nanoribbon in Metal–Organic Framework. *J. Am. Chem. Soc.* **2020,** *142* (12), 5509-5514.

147.   Simionescu, C. I.; Bulacovschi, V.; Grovu-ivanoiu, M.; Stanciu, A., Polymerization of Methyl Propiolate with Palladium Chloride, Triphenylphosphine, and Palladium Chloride Triphenylphosphine Complex. *J. Macromol. Sci. A.* **1987,** *24* (6), 611-622.

148.   Soteras Gutiérrez, I.; Lin, F. Y.; Vanommeslaeghe, K.; Lemkul, J. A.; Armacost, K. A.; Brooks, C. L., 3rd; MacKerell, A. D., Jr., Parametrization of halogen bonds in the CHARMM general force field: Improved treatment of ligand-protein interactions. *Bioorg. Med. Chem.* **2016,** *24* (20), 4812-4825.

149.   Vanommeslaeghe, K.; MacKerell, A. D., Jr., Automation of the CHARMM General Force Field (CGenFF) I: bond perception and atom typing. *J. Chem. Inf. Model.* **2012,** *52* (12), 3144-54.

150.   Vanommeslaeghe, K.; Raman, E. P.; MacKerell, A. D., Jr., Automation of the CHARMM General Force Field (CGenFF) II: assignment of bonded parameters and partial atomic charges. *J. Chem. Inf. Model.* **2012,** *52* (12), 3155-68.

151.   Yu, W.; He, X.; Vanommeslaeghe, K.; MacKerell, A. D., Jr., Extension of the CHARMM General Force Field to sulfonyl-containing compounds and its utility in biomolecular simulations. *J. Comput. Chem.* **2012,** *33* (31), 2451-2468.

152.   Hirst, G.C., *Methyl Propiolate*. In *Encyclopedia of Reagents for Organic Synthesis*. John Wiley & Sons:2001.

153.   Dybtsev, D. N.; Chun, H.; Kim, K., Rigid and Flexible: A Highly Porous Metal–Organic Framework with Unusual Guest-Dependent Dynamic Behavior. *Angew. Chem. Int. Ed.* **2004,** *43* (38), 5033-5036.

154.   Liang, Z.; Marshall, M.; Chaffee, A. L., CO2 adsorption, selectivity and water tolerance of pillared-layer metal organic frameworks. *Micropor. Mesopor. Mater.* **2010,** *132* (3), 305-310.

155.   Guerrero, V. V.; Yoo, Y.; McCarthy, M. C.; Jeong, H.-K., HKUST-1 membranes on porous supports using secondary growth. *J. Mater. Chem.* **2010,** *20* (19), 3938-3943.

156.   Worrall, S. D.; Bissett, M. A.; Hill, P. I.; Rooney, A. P.; Haigh, S. J.; Attfield, M. P.; Dryfe, R. A. W., Metal-organic framework templated electrodeposition of functional gold nanostructures. *Electrochim. Acta* **2016,** *222*, 361-369.

157.   Cai, Z.; Liu, S., *Applications of MALDI-TOF spectroscopy*. Springer: 2014; Vol. 331.

158.   Lee, C.; Lu, I. C.; Hsu, H. C.; Lin, H.-Y.; Liang, S.-P.; Lee, Y.-T.; Ni, C.-K., Formation of Metal-Related Ions in Matrix-Assisted Laser Desorption Ionization. *J. Am. Soc. Mass. Spectrom.* **2016,** *27* (9), 1491-1498.

159.   Kanj, A. B.; Verma, R.; Liu, M.; Helfferich, J.; Wenzel, W.; Heinke, L., Bunching and Immobilization of Ionic Liquids in Nanoporous Metal–Organic Framework. *Nano Lett.* **2019,** *19* (3), 2114-2120.

160.   Liu, J.; Wächter, T.; Irmler, A.; Weidler, P. G.; Gliemann, H.; Pauly, F.; Mugnaini, V.; Zharnikov, M.; Wöll, C., Electric Transport Properties of Surface-Anchored Metal–Organic Frameworks and the Effect of Ferrocene Loading. *ACS Appl. Mater. Interfaces* **2015,** *7* (18), 9824-9830.

PUBLICATIONS

1. Haldar, R.[#], **Sen, B.**[#], Hurrle, S., Kitao, T., Sankhla, R., Kühl, B., Welle, A., Heissler, S., Brenner-Weiß, G., Thissen, P., Uemura, T., Gliemann, H., Barner-Kowollik, C., Wöll, C. Oxidative polymerization of terthiophene and a substituted thiophene monomer in metal-organic framework thin films. *European Polymer Journal*, **2018**, 109, 162-168.

2. **Sen, B.**, Santos, J. C. C., Haldar, R., Zhang, Q., Hashem, T., Qin, P., Li, Y., Kirschhöfer, F., Brenner-Weiß, G., Gliemann, H., Heinke, L., Knebel, A., Wöll, C. Introducing electrical conductivity to metal-organic framework thin films by templated polymerization of methyl propiolate. *Nanoscale*, **2020**, Accepted Manuscript.

# The authors contributed equally.

CURRICULUM VITAE

Personal data

Name: Beren Sen

Title: M.Sc.

Education

2017-2020   **Ph.D. Candidate**, Chemistry
Institute of Functional Interfaces
Faculty of Chemistry and Biosciences
Karlsruhe Institute of Technology (KIT), Karlsruhe, Germany
PhD Thesis: "Polymerization Control in Surface-Mounted Metal-Organic Frameworks" under the supervision of Prof. Dr. C. Wöll

2013-2016   **M. Sc.**, Molecular Biology-Genetics and Biotechnology
Department of Molecular Biology-Genetics and Biotechnology
Istanbul Technical University (ITU), Istanbul, Turkey
Master Thesis: "Design and Characterization of a Wound Dressing System for Effective Pain Relief" under the supervision of Assoc. Prof. Dr. F. N. Kök

2008-2013   **B. Sc.**, Molecular Biology and Genetics
Department of Molecular Biology and Genetics
Istanbul Technical University (ITU), Istanbul, Turkey
Bachelor Thesis: "Characterization of Polymeric Protein Microencapsulation Systems" under the supervision of Assoc. Prof. Dr. F. N. Kök

2003-2008   **Sankt Georg Austrian High School**, Istanbul, Turkey
1 year of German preparation class

Conferences

- Poster presentation: EuroMOF 19; Paris, France; October 27-30, 2019.
- Poster presentation: Biennial Meeting of the GDCh-Division of Macromolecular Chemistry; Karlsruhe, Germany; September 24-27, 2018.
- Oral presentation: DocMOF 2018; Raitenhaslach, Germany; April 29- Mai 02, 2018.

ACKNOWLEDGEMENTS

I would like to express my special gratitude to my family starting with my dear mother Müfide Sen, my father and my idol Prof. Dr. Mete Sen, my brother Berke Sen and my brother's wife Laure Lopato for their endless love, patience and support throughout my life and my stressful times. Nothing would be possible without you.

I would like to give my special thanks to my beloved boyfriend Faruk Karakilic for being my motivation during these three years. He helped me always to find my way when I was lost and encourage me to continue.